FLOW BEHAVIOR, MIXING AND MASS TRANSFER IN A PEIRCE-SMITH CONVERTER USING PHYSICAL MODEL AND COMPUTATIONAL FLUID DYNAMICS

by

Deside Kudzai Chibwe

Thesis presented in partial fulfillment

of the requirements for the Degree

of

MASTER OF SCIENCE IN ENGINEERING

(Extractive Metallurgical Engineering)

in the Faculty of Engineering

at Stellenbosch University

Supervised by

Prof. G. Akdogan

Prof. C. Aldrich

STELLENBOSCH

March 2011

DECLARATION

By submitting this thesis electronically, I declare that the entirety of the work contained therein is my own, original work, that I am the sole author thereof (save to the extent explicitly otherwise stated), that reproduction and publication thereof by Stellenbosch University will not infringe any third party rights and that I have not previously in its entirety or in part submitted it for obtaining any qualification.

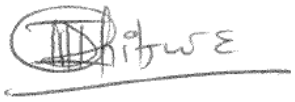

17 February 2011

Signature (Deside K. Chibwe) **Date**

ABSTRACT

The flow pattern, mixing and mass transfer characteristics in an industrial Peirce-Smith converter (PSC) have been experimentally and numerically studied in this work using cold model simulations. The development of a cold model to simulate an industrial Peirce-Smith converter was achieved through a realistic small-scale representation of the system that meets specified geometric, kinematic and dynamic similarity between the model and industrial equipment.

The effects of air flow rate and presence of overlaying slag phase on matte on the flow structure, mixing and mass transfer efficiency were investigated. The 2-D and 3-D simulations of the three phase system were carried out using volume of fluid (VOF) and realizable $k-\varepsilon$ turbulence models to account for the multiphase and turbulent nature of the flow respectively. These models were implemented using a commercial Computational Fluid Dynamics (CFD) numerical code, FLUENT.

The cold model for physical simulations was a 1:5 horizontal cylindrical container made of Perspex with seven tuyeres on one side of the cylinder typifying a Peirce-Smith converter. Compressed air was blown into the cylinder through the tuyeres, simulating air or oxygen enriched air injection into the PSC.

Industrially treated feed, product and by-product, referred to as matte-white metal and slag were simulated with water and kerosene respectively in this study. The influence of varying air flow rate and simulated slag quantities on the bulk mixing and mass transfer was studied with five different compressed air flow rates and five levels of simulated slag thicknesses at constant simulated matte volume.

Mixing time results were evaluated in terms of total specific mixing power, ε_m and the following correlation: $T_{mix} = 30722 Q^{1.35} SS_t^{-0.08}$ where Q is in (Nm^3s^{-1}) and SS_t in (m), was proposed for estimating mixing times in the model of PSC. Solid-liquid mass transfer was characterized by calculated mass transfer coefficients and turbulence parameter values of benzoic acid sintered compacts spatially positioned in the model. The mass transfer coefficients and turbulence parameter values were highest at the bath surface and near plume region and decreased in identified dead zones in the regions close to the circular side walls of

the model. Stratification of fluid flow was concluded due to different mass transfer coefficients and turbulence parameters of compacts placed on the same distance from the tuyere line region but differed in submergence.

Mathematical simulations were also conducted to see the effect on mixing on only simulated matte systems with equivalent bath height of simulated matte and slag. It was concluded from these simulations that presence of simulated slag contributes to the prolonged mixing times observed in the PSC scale model as mixing times were observed to decrease in only simulated matte system relative to the system with equivalent total bath height of simulated matte and slag.

Both numerical and experimental simulations were able to predict the variation characteristics of the system in relation to flow field. This was achieved through mathematical calculation of relevant integrated quantities of turbulence, volume fraction (VF) and velocity magnitudes. Both air flow rate and presence of the overlaying slag layer has been found to have profound effects on the mixing efficiency of the converter.

OPSOMMING

In hierdie studie is die vloeipatrone, vermenging en massa oordrag eienskappe in ‘n industriële Pierce-Smith reaktor (PSR) eksperimenteel en numeries deur middel van koue model simulasies ge-evalueer. Die ontwikkeling van ‘n koue model om ‘n industriële Pierce-Smith reaktor te simuleer, is uitgevoer deur gebruik te maak van ‘n realistiese laboratorium-skaal voorstelling van ‘n industriële sisteem met gespesifiseerde geometriese, kinematiese en dinamiese ooreenstemmings tussen die model en industriële toerusting.

Die invloed van lug vloeitempo en die teenwoordigheid van ‘n oorlaag slak oor mat op die vloei struktuur, vermenging en massa oordrag is ge-evalueer. Die 2-D en 3-D simulasies van die driefase sisteem is uitgevoer deur volume vloeier en haalbare $k-\varepsilon$ turbulensie modelle te gebruik om vir die multifase en turbulente natuur van die vloei ondeskeidelik te vergoed. Hierdie modelle is geimplementeer deur ‘n kommersiële Rekenkundige-Vloei-Dinamika numeriese kode, FLUENT.

Die koue model vir fisiese simulasies was ‘n 1:5 horisontale silindriese Perspex houer met sewe blaaspypies aan een kant van die silinder en was tipies dit van ‘n industriële Pierce-Smith reaktor. Druklug was deur die blaaspypies in die silinder ingeblaas om lug- of suurstof verrykte lug inspuitings te simuleer.

In hierdie studie is industrieel behandelde voer, produk en by-produk (verwys na mat-wit metaal en slak) deur water en keroseen onderskeidelik gesimuleer. Die invloed van veranderlike lug vloeitempo en gesimuleerde slak hoeveelhede op die vermenging en massa oordrag was ge-evlaueer deur gebruik te maak van vyf versillende lug vloeitempos en vyf vlakke van gesimuleerde slakdikte teen konstante mat volume.

Vermengingstyd resultate is ge-evalueer in terme van totale spesifieke krag, ε_m, en die volgende korrelasie: $T_{mix} = 30722 Q^{1.35} SS_t^{-0.08}$ met die eenhede vir Q in (Nm^3s^{-1}) en vir SS_t in (m). Hierdie metode vir die evaluering van vermengingstyd was voorgestel in die PSR model. Vastestof-vloeistof massa oordrag was gekarakteriseer deur berekende massa oordrag koeffisiënte en turbulensie parameter waardes van benzoësuur behandelde kompakte wat ruimtelik in die model geplaas was. Die hoogste massa oordrag koeffisiënte en turbulensie parameter waardes is verkry by die bad oppervlak en naby die pluim area en het afgeneem in

geidentifiseerde dooie sones na aan die sirkelvormige sy-mure van die model. Die gevolg van verskillende massa oordrag koeffisiënte en turbulensie parameters van die kompakte het gevolg tot stratifikasie van vloeier vloei in lyn met die blaaspypies en het verskil in vertikale diepte vanaf die blaaspypies.

Wiskundige simulasies is ook uitgevoer om te sien wat die effek van vermenging op slegs mat sisteme met soortgelyke bad hoogtes van reeds gesimuleerde mat en slak sisteme was. Die gevolgetrekking van die simulering van slegs mat sisteme het aangedui dat die teenwoordigheid van ‘n slak-fase die vermengingstyd verleng in die PSR model, aangesien die vermengingstyd verkort het in simulasies van slegs mat sisteme met soortgelyke bad hoogtes as mat en slak sisteme.

Beide numeriese en eksperimentele simulasies het die vermoë gehad om die verandering in karakteristieke van die sisteem in ooreenstemming met die vloeiveld vooruit te skat. Dit was bereik deur die wiskundige berekening van relevante geintegreerde hoeveelhede van turbulensie, volume fraksie (VF) en snelheid groottes. Dit was bevind dat beide die lug vloeitempo en die teenwoordigheid van ‘n oorlaag slak oor mat ‘n beduidende invloed op die vermengingseffektiwiteit van die PSR gehad het.

ACKNOWLEDGEMENTS

There is no research work that could be produced by an individual, but rather successful research output is a reflection of influences and experiences received from a broad range of sources. It is my pleasure to acknowledge the help, advice, insights, support and encouragement I received from different people and/ or organizations in setting up, carrying out and the final production of this piece of work.

Firstly I would want to say thank you to my supervisors Prof. G Akdogan and Prof. C Aldrich for their unabated and invaluable support, experience, patience and excellent supervision of the project that has made this writing a success. Through your guidance, I have realized that it is not worth to rush to a destination for there is high chance of missing half the fun of being there. You provided an opportunity for me to understand computational fluid dynamics modelling which seemed to be a nightmare in the infants of this research.

I would also like to express my gratitude to Qfinsoft South Africa, distributors and product support of Fluent. Many thanks go to fellow students and staff at all functional levels in the Department of Process Engineering for various contributions. I really appreciate the help from technical personal in the mechanical workshop for swift response to my needs in setting up the physical model for this work. Janie Barnard and team, I say thank you.

Lastly, I am also grateful to my family for their support during this period of study and above all the almighty who made everything possible.

TABLE OF CONTENTS

LIST OF FIGURES

LIST OF TABLES

LIST OF APPENDICES

NOMENCLATURE

SYMBOL	DESCRIPTION	UNITS
A	Total cross sectional/ interfacial area	m^2
C	Dissolved concentration of solute in bulk liquid	$molm^{-3}$
C_D	Drag coefficient	
C_{sat}	Concentration of solute in the boundary layer	$molm^{-3}$
d	Sample diameter	mm
d_o	Tuyere diameter	mm
d_p	Particle diameter	mm
D	Diffusivity	m^2s^{-1}
D_H	Hydraulic diameter	mm
D_t	Turbulent diffusivity	m^2s^{-1}
$D_{i,m}$	Mass diffusion coefficient for i th species in the mixture	
$D_{T,i}$	Thermal diffusion coefficient for i th species in the mixture	
E	Total energy	J
$\vec{F}$	Gravitational body force	ms^{-2}
F_D	Drag force	N
F_x	Additional acceleration term	Nkg^{-1}
g	Gravitational constant	ms^{-2}
G_k	Turbulent kinetic energy generation due to mean velocity gradients	m^2s^{-2}
G_b	Turbulent kinetic energy generation due to buoyancy	m^2s^{-2}

h	Sensible enthalpy	
h_i	Sensible enthalpy of i th species	
H_s	Submergence of injection	mm
H_b	Liquid (bath) depth	mm
i , j	Species	
I	Turbulent intensity	
$\vec{J}$	Diffusion flux	$molm^{-2}s^{-1}$
$\vec{J}_i$	Diffusion flux of i th species	$molm^{-2}s^{-1}$
k	Turbulent kinetic energy	m^2s^{-2}
K	Mass transfer coefficient	ms^{-1}
k_{eff}	Effective thermal conductivity	$WK^{-1}m^{-1}$
k_t	Turbulent thermal conductivity	$WK^{-1}m^{-1}$
k_T	Thermal conductivity	$WK^{-1}m^{-1}$
l_{model}	Model physical dimension	m
l_{ptype}	Prototype (real) converter physical dimension	m
L	Sample length	mm
$\dot{m}$	Mass flow rate	kgs^{-1}
$\dot{m}_{pq}$	Mass transfer from phase p to phase q	
$\dot{m}_{qp}$	Mass transfer from phase q to phase p	
m	Sample mass	g
M_{eqs}	Equisize skewness	
N^*_{Fr}	Modified Froude number	
N_{Mo}	Morton number	
N_{faces}	Number of faces enclosing computational cell	

P	Static pressure	Pa
P_w	Wetted perimeter	mm
Q	Air volumetric flow rate	Nm^3s^{-1}
r_i	Sample initial radius	mm
r_f	Equivalent final sample radius	mm
R_i	Net rate production of i th species by chemical reaction	
Re	Reynolds number	
Re_t	Turbulent/ tuyere Reynolds number	
$Re_{loc,r}$	Local nominal Reynolds number	
S	Area (2-D) or volume (3-D) of the computational mesh element	
S_{eq}	Maximum area (2-D) or volume (3-D) of an equilateral element	
S_i	Net rate creation of i th species by addition from the dispersed phase	
S_m , S_ε	Mass and turbulent dissipation source terms	
S_E , S_k	Energy and turbulent kinetic energy source terms	
Sc	Schmidt number	
Sc_t	Turbulent Schmidt number	
Sh	Sherwood number	
SS_t	Simulated slag thickness	mm
τ	Measure of mixing time	s
$\bar{\bar{\tau}}_{eff}$	Effective stress tensor	Pa
T	Temperature	K
T_{mix}	Mixing time	s
T_i	Turbulence characteristic	
v_x , v_y , v_z	x, y, z- velocity components	ms^{-1}

v_p	Particle velocity	ms^{-1}
$\vec{v}$	Overall velocity vector	ms^{-1}
v_t	Tuyere gas velocity	ms^{-1}
V	Computational cell volume	
Y_i	Local mass fraction of i th species	
Y_M	Ccontribution of the fluctuating dilatation in turbulence	
α	Fluid phase fraction	
ψ	Under-relaxation factor	
λ	Scale factor	
Γ	Diffusion coefficient	
∇	Gradient operator	
μ	Dynamic viscosity	Pas
μ_t	Turbulent dynamic viscosity	Pas
σ	Surface tension	Nm^{-1}
θ_{cal}	Calculated scalar quantity variable magnitude	
θ_{new}	New scalar quantity variable magnitude	
θ_{old}	Old scalar quantity variable magnitude	
ρ_g , ρ_l	Density of gas and liquid respectively	kgm^{-3}
ρ_p , ρ_s	Density of particle and sample respectively	kgm^{-3}
p , q	Fluid phases	
$\bar{\bar{\tau}}$	Stress tensor	Pa
ε	Turbulent dissipation rate	m^2s^{-3}

ε_b	Buoyancy specific power	$kWton^{-1}$
ε_k	Kinetic energy specific power	$kWton^{-1}$
ε_m	Specific mixing power	$kWton^{-1}$
ϕ	Scalar quantity (Temperature, Turbulence, e.t.c)	

ABBREVIATIONS

CFD - Computational Fluid Dynamics

DPM - Discrete Phase Model

Gambit - Geometry and Mesh Building Intelligent Toolkit

PSC - Peirce-Smith converter

RKE - Realizable $k-\varepsilon$ model

SKE - Standard $k-\varepsilon$ model

VOF - Volume of Fluid

VF - Volume Fraction

CHAPTER 1

INTRODUCTION

Copper is widely used substantially for both industrial and domestic applications. Due to its physical characteristics of high thermal conductivity, ductility, resistance to corrosion and malleability, it has great application in industrial sectors of construction and healthcare facilities (Frankel & Frankel 2009). Over 65% of produced copper is used in the electrical industry for power generation and transmission (Baxamusa, 2010). It is mostly produced from copper ores by a concentration-smelting-refining route (Davenport et al. 2002). Presently, the most widespread method of smelting comprises of two stages to produce molten sulphide matte from Cu-Fe sulphide concentrates, in a process referred to as converting (Davenport et al. 2002).

During converting, the first stage consists of slag forming, processes aimed at separating copper and other metals from non-metallic impurities within the molten matte. This operation removes about one-third of sulphur and the greater part of the iron. In the second stage, which is called copper making, iron is completely eliminated from the matte and the remaining copper sulphide is oxidized to almost pure copper (blister copper >99.5 wt% Cu). The most common industrial equipment to carry out such chemical oxidation is the Peirce-Smith converter (PSC), which was first conceived at Baltimore Copper Company in 1905, and currently accounts for over 90% of the world production of copper (Liow & Gray 1990b, Real et al. 2007, Gonzalez et al. 2008).

A Peirce-Smith converter is a cylindrical horizontal steel reactor (circular canal geometry) lined inside with refractory material. Air or oxygenated air at subsonic velocity is injected into the converter through submerged tuyeres which come along the axis of the converter (Gonzalez et al. 2008). The injected air or oxygenated air has a two-fold function which is to supply oxidant (reactant) for the chemical oxidation of iron and sulphur associated with the copper and energy to stir the bath. Energy is supplied in three forms namely kinetic, buoyancy and expansion. The mentioned functions affect the chemical and physical processes

occurring in the converter such as converting rate, oxygen efficiency, dispersion, mixing, heat and mass transfer, slopping, splashing and accretion growth (Haida & Brimacombe 1985, Valencia et al. 2004).

Since there are chemical reactions taking place with products being formed, quality and quantity of mixing is important. Mixing will promote chemical reactions, removing the products from reaction sites; minimize temperature and composition inhomogeneties (Singh & McNallan 1983, Sinha & McNallan 1985). Due to generation of turbulence in the converter, mixing may aid inclusion agglomeration, coalescence and floatation of impurities, thus improving converter efficiencies (Gray et al. 1984).

During the converting process, a substantial amount of cold solid additions are added in the form of fluxing material for slag liquefaction and process scrap and/or reverts for purposes of temperature control and scrap utilization. The mechanism of dissolution (mass transfer) of the cold additions and active sites within the cylinder is not well understood. Rates of dissolution can be logically assumed to affect the thermal state of the converter and turns out to be a factor that affects the turnaround time of the converter processing. As such, establishing a stable functional state of the converter and fully developed categorization of flow fields is necessary for effective process control.

Though the PSC has been the major blister copper production route for over a century, there has been insufficient research on process engineering which lower considerably the productivity of the process. Mixing and mass transfer in the converter are such key tenets process parameters that have been little studied. Most research on mixing and injection phenomena in gas/ liquid multiphase systems has been conducted in the steel making and ladle metallurgy (Sinha & McNallan 1985, Sahai & Guthrie 1982, Mazumdar & Guthrie 1986, Castillejos & Brimacombe 1987, Stapurewicz & Themelis 1987, Kim & Fruehan 1987). Due to similarity of the basic concept in ladle injection and PSC, the principles of their works has been adopted in the past decades on process characterization research of PSC in an attempt to address the challenges in productivity (Gray et al. 1984, Hoefele & Brimacombe 1979, Vaarno et al. 1998). Review of such studies will be covered in the subsequent chapter.

Macroscopic physical and numerical models of PSC have been developed to study multiphase fluid flow phenomena (Real et al. 2007, Gonzalez et al. 2008, Valencia et al. 2004, Vaarno et al. 1998, Liow & Gray 1990a, Koohi et al. 2008, Ramirez-Argaez 2008,

Rosales et al. 2009). However, despite the bulk of numerical and investigational work on the subject of fundamental phenomenon of multiphase flow, gas injection and mixing, there are no comprehensive statements on scaling up of model trial results. This is due to the difficulties of extrapolation of correlations deduced because of similarity shortfall between models and industrial (real) systems (Szekely et al. 1988).

Against such background, the purpose of this research is to investigate the dependence of mass transfer and the mixing parameter on the operating system variables such as volumetric gas flow rate and the presence of second phase (slag). A water bath physical model of equivalent properties as the generic industrial PSC to carry out the experiments was designed using similarity principles. Geometric and dynamic similarity were used in the design for equivalency between prototype and model since hydrodynamic studies on fluid flow are not concerned with thermal and chemical similarity effects (Mazumdar 1990).

With the help of literature and knowledge of the fluid flow physics phenomena under current study, the dynamic similarity (blowing parameters) and the reliability of the physical model were determined using Modified Froude number, N_{Fr}^{*} which resembles fluid flow dominated by inertial and gravitational forces which are more pronounced than molecular viscous forces (Mazumdar & Evans 2004). The molten liquid phases in the real PSC namely matte and slag were simulated in the model with water and kerosene respectively. The kinematic similarity was maintained by using the dimensionless Morton number, N_{Mo}. In the literature, in physical simulation studies, mixing time were measured using different techniques. Most of these techniques included acid injection into the bath and monitoring pH changes with respect to time. Stable values of +/-0.01pH units were taken as 99% mixing. This method was employed in the current studies. Mixing times were determined experimentally by tracer dispersion technique using 98% sulphuric acid (H_2SO_4). The decay in pH against time to a steady state value of +/-0.01pH units in the bath was measured.

In simulation of solid additions in the converter, sintered benzoic acid cylinder compacts were used. These cylinders were placed at predetermined sites within the model converter. Mass transfer rates from these cylinders were measured at various gas flow rates and simulated slag thicknesses.

In order to have good level understanding of the experimental results, isothermal transient multiphase 2-D and 3-D CFD numerical simulations were carried out. The Computational Fluid Dynamics (CFD) software Fluent was used to solve the transient Navier-Stokes equations. The Realizable $k-\varepsilon$ turbulent model and infinitesimal fluid element also known as volume of fluid (VOF) was used to model the turbulent nature and multiphase flow respectively. Attention was paid to the average velocity profiles and turbulence kinetic energy generation to explain mixing and mass transfer in the converter.

In the subsequent chapter, a review of basic copper converting principles will the done to add understanding to the current scope of work followed by mixing and mass transfer studies in gas injected systems of relevance. Chapter 3 will unearth model developments and experimental methods employed in the study. Results and discussions will be presented in Chapter 4. Chapter 5 and Chapter 6 will comprise of conclusions and recommendations respectively.

.

CHAPTER 2

LITERATURE REVIEW

2. INTRODUCTION

It can be logically postulated that mixing and mass transfer rates in a Peirce-Smith converter affect the overall process efficiency in relation to chemical and thermal homogeneity and the distribution of phases. The conversion process used in removing iron and sulphur from the furnace matte is a complex phenomenon involving various chemical reactions. It is also associated with heat generation and phase interactions at temperatures around 1250^{o}C (Kyllo & Richards 1998a, Kyllo & Richards 1998b).

Through mapping the fluid flow in the converter, we can have some knowledge on mixing and the dissolution of additives. This provides information on required processing turnaround time and appropriate mechanisms for addition of additives. Because of the high temperatures involved, methods for mixing and mass transfer measurements are difficult, if not impossible.

This work focuses on the development of a cold model to simulate an industrial Peirce-Smith converter (PSC) which is used in the copper making industry. This can be achieved through a realistic small-scale representation of the system that meets specified geometrical, kinematic and dynamic similarity between the model and industrial equipment (Szekely et al. 1988, Mazumdar & Evans 2004). Hence, the desired measurements can be made more conveniently in a cost effective manner. The effects of phase interactions and blowing conditions on mixing and mass transfer are investigated in this work using such a model.

Due to limited quantitative research work to date on PSC, an overall strategy has been devised to explain and evaluate experimental results using numerical simulations of the converter through Computational Fluid Dynamics (CFD) code software. The subsequent sections discuss basic PSC operations, mixing and mass transfer literature as well as numerical analysis development to be used in this research work.

2.1 Peirce-Smith converter

A Peirce-Smith converter (PSC) is a commercial reactor used for the conversion smelting of furnace copper matte into blister copper. It is a horizontal refractory-lined steel shell cylindrical furnace mounted on trunnion at either end. It is rotated about the major axis for charging and pouring. An opening at the converter centre functions as the mouth through which furnace molten matte, siliceous flux and copper scrap are charged. The mouth also serves as the process off-gas outlet.

It has a number of injection nozzles referred to as tuyeres situated along one side length of the converter where air or oxygen enriched air is blown through the matte to remove iron and sulphur chemically and physically associated with the copper (Liow & Gray 1990b). The converting process, which is accomplished by the reaction of oxygen and matte constituencies, will be discussed in the subsequent section. The position of a Peirce-Smith converter in an integrated copper making route is shown in schematic process flow diagram shown in **Figure 1**.

2.2 Converting Process

The matte, molten sulphide, is produced in the smelter furnaces and contains around 45 – 75 wt% copper primarily as copper sulfide with a substantial amount of iron sulfide as impurity. Table 1 below shows a typical composition of a copper matte in a copper making process.

Constituent	Cu	Fe	S	O	Others
wt%	45 - 75	3 - 30	20 – 23	1 - 3	> 3

Table 1: Typical industrial copper matte composition (Davenport et al. 2002).

The main aim of the converting process is the elimination of iron and sulphur through oxidation thereby producing blister copper (98 – 99.5 wt% Cu). This process proceeds in two distinct stages, namely slag forming and copper making.

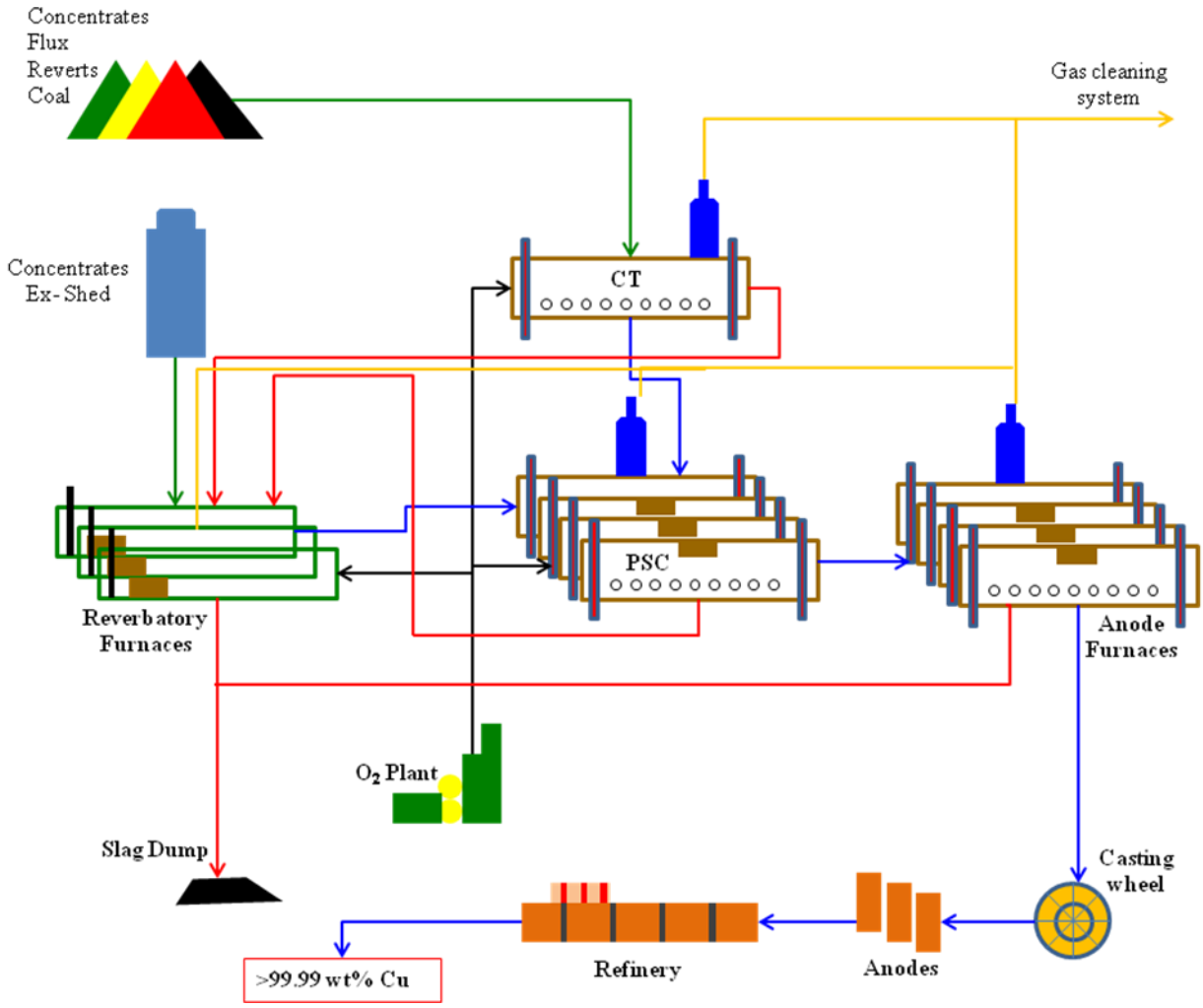

Figure 1: Typical process flow of an integrated copper making process - Adapted from Syamujulu (2005)

2.2.1 Slag Forming

During this stage, air or oxygen enriched air is blown through the matte. Iron sulphide is oxidized into iron oxides and, due to oxidation reactions, sulphur dioxide gas is produced. Iron oxide forms an intimate mixture with silica to form fayalite slag. Depending on the thermodynamic state of the converter as well as oxygen activity in the process, the iron oxides can be further oxidized to haematite (Fe_2O_3) which posses the problem of entrainment and eventual copper losses to slag (Imris et al. 2005). Two phases are formed after the reactions, namely siliceous slag and white metal (Cu_2S) which stratifies due to density differences, with slag floating on the underlying white metal (Kyllo & Richards 1998a, Živković et al. 2009). The chemical reactions proceeds as given below

$$2FeS + 3O_2 \rightarrow 2FeO + 2SO_2$$ **Equation 1**

$$FeO + SiO_2 \rightarrow FeO \cdot SiO_2$$ (Slag product) **Equation 2**

Slag produced is intermittently skimmed off and fresh charge is added. The charge comprises of copper matte and siliceous materials (fluxes) for slag chemistry as well as process scrap, ladle skulls and reverts for temperature control.

2.2.2 Copper Making

Blowing, intermittent slagging off and charging continue until an adequate amount of relatively pure copper sulphide (Cu_2S) accumulates in the bottom of the converter. This product is referred to as "white metal". A final air or oxygenated air blast is performed to oxidize the sulphur to sulphur dioxide, thereby producing blister copper. The oxidation chemical reactions proceeds as given by **eq. (3)** – **eq. (5)**.

$$2Cu_2S + 3O_2 \rightarrow 2Cu_2O + 2SO_2$$ **Equation 3**

$$Cu_2S + 2Cu_2O \rightarrow 6Cu + SO_2$$ **Equation 4**

The overall reaction is:

$$Cu_2S + O_2 \rightarrow 2Cu + SO_2$$ **Equation 5**

The blister copper produced is tapped out of the converter for subsequent refining operations to remove residual oxygen. The sulphur dioxide gas produced throughout the operation is vented to pollution control systems or used as a raw material in sulphuric acid making plants.

2.3 Project Perspective

The preceding section highlighted the key process outline of the converting operation. It is evident that the flow field, in the PSC, is a multiphase system. Influence of interaction of the phases and injection variables on the process efficiency will add to better process control strategies. Rates of dissolution of solids added in the PSC in the form of fluxes and scrap is of major concern as it affects process turn-around time as well as chemical, compositional and thermal homogeneity of the system. Dissolution, mixing and mass transfer rates are function of kinetic energy of the system induced recirculatory flows coupled with the turbulence.

The current study focuses on the mixing and mass transfer in the PSC using scale water model. Geometric and dynamic similarity criterion was used to develop a water based one-fifth scale slice physical model to simulate a typical industrial PSC. The results give a quantitative measure of time and field flow state mapping at predetermined positions in space. The subsequent section review modelling techniques for industrial metallurgical vessels.

2.4 Modelling

Modelling is a practical tool for design optimization and problem solving of real systems at a cost-effective manner in the absence of elaborate experiments which might not be possible (Szekely et al. 1988, Mazumdar & Evans 2004). Fundamental understanding of the process to be modelled is required to exploit the capabilities of the modelling tools. Design work and/ or continual improvement is possible provided results of modelling are presented in a meaningful way. There are two broad sense of modelling, namely physical and numerical. Depending on the problem to be solved and availability of validation data, the models can be applied individually or in unison for comparative purposes. The models are presented in the subsequent section.

2.4.1 Physical Modelling

Physical modelling involves the presentation of features of a process which may be of interest to the researcher. Depending on the research interest, extent of physical model development differs and they are three main classifications:

a) Physical models developed to identify key features of a process or behaviour of a system without strictly following similarity.
b) Physical models developed by strictly following similarity criteria so as to facilitate direct extrapolation of results to the real system
c) Physical models developed to provide information for the development of a numerical model

Similarity using dimensionless numbers is the key feature in the development of physical models. Dimensionless numbers analysis using Buckingham π-Theorem can yield a number of the dimensionless numbers to be considered for a single problem. It is difficult to observe

all equivalency and some have to be ignored. Knowledge of the problem physics is necessary so that order of magnitude analysis can be implemented to consider relevant groups (Mazumdar & Evans 2004).

In pyrometallurgical submerged gas blown processes in ladle metallurgy, physical modelling investigations by researchers Kim & Fruehan (1987), Han et al. (2001), Fabritius et al. (2002) and Nyoka et al. (2003) to mention a few, have been performed using geometric and dynamic similarity. Geometric similarity was observed using scale factor, λ on all physical dimensions, and dynamic similarity achieved through Modified Froude number, N_{Fr}^{*} given by:

$$\lambda = \frac{l_{model}}{l_{ptype}} \qquad \textbf{Equation 6}$$

$$N_{Fr}^{*} = \frac{v_t^2 \rho_g}{g(\rho_l - \rho_g)d_o} \qquad \textbf{Equation 7}$$

Also in a recent study to investigate the factors affecting splashing in a PSC by Koohi et al. (2008), kinematic similarity was observed between prototype and water based model through Morton number, N_{Mo} equivalency given by:

$$N_{Mo} = \frac{g\mu^4}{\rho_l \sigma^3} \qquad \textbf{Equation 8}$$

In **eq. (6)** – **eq. (8)**, l_{model} (m) is model physical dimension, l_{ptype} (m) is prototype (real) converter physical dimension, v_t (ms^{-1}) is tuyere gas velocity, ρ_g (kgm^{-3}) is gas density, ρ_l (kgm^{-3}) is liquid (slag or matte) density, g (ms^{-2}) is gravitational constant, d_o (m) is tuyere diameter, μ (Pas) is liquid dynamic viscosity and σ (Nm^{-1}) is liquid surface tension.

2.4.2 Numerical Modelling

Numerical models may be used to represent a physical process or aspects of physical process in the form of differential equations. In pyrometallurgical operations, the models have been used extensively to establish functional relationships of process variables like reaction kinetics (Kyllo & Richards 1998b), injection dynamics (Schwarz 1996, Rosales et al. 1999, Valencia et al. 2002) and fluid flow behavior (Real et al. 2007, Valencia et al. 2004, Han et al. 2001). Three categories of numerical models exist namely:

a) ***Semi empirical models*** based on physical laws that incorporate some constraints adjustments due to complexity of the modelling equations.
b) ***Input-output models*** representing totally empirical relationships between the key process valuables.
c) ***Fundamental theoretical models*** developed from physical laws. Generically physical phenomena in a closed system are governed by three equations namely: conservation of mass, momentum and energy as basic building blocks of the models which are discussed in **section 2.4.2.2.1** and **section 2.4.2.2.2** respectively. Partial differential equations with appropriate boundary and initial conditions are solved.

2.4.2.1 Computational Fluid Dynamics (CFD)

In principle, CFD is the science of finding the exact numerical solutions in space and time by solving numerically a set of fluid dynamics governing mathematical equations coupled together with either steady state or transient analysis. A broad range of mathematical models for transport phenomena (like fluid flow, heat transfer, mass transfer, species dispersion and chemical reactions) can be combined with the ability to model complex industrial and non-industrial applications and processes.

2.4.2.2 The governing equations

Depending on the complexity of the model to be developed, the physical phenomena in a closed system can be governed by mathematical statements of the conservation laws of physics. These equations are referred to as governing equations of fluid flow and heat transfer (Versteeg & Malalasekera 2007).

The mathematical statements are presented by mass conservation or continuity, momentum and energy equations also known as the Navier-Stokes equations. In cases where heat transfer, compressibility, species mixing and reactions are involved, additional equations are solved. These equations are nonlinear partial deferential equations and have to be discretized to algebraic equations and iterative methods of solution implemented (ANSYS 2008). These equations are presented in the subsequent sections.

2.4.2.2.1 Mass conservation (Continuity) equation

The general equation for conservation of mass, or continuity equation, can be written as given in **eq (9)**:

$$\frac{\partial \rho}{\partial t} + \nabla \cdot (\rho \vec{v}) = S_m \qquad \textbf{Equation 9}$$

This equation is valid for incompressible as well as compressible flows. The operator (∇) presents the partial derivative of a quantity with respect to all directions in the chosen coordinate system (2D or 3D). In the equation, the first term on the left hand side is the transient term and the second term represents the convective term, while the right hand side of the equation contains any mass source term that must be either user defined or specified where, $\vec{v}$ (ms^{-1}) is the overall velocity vector.

2.4.2.2.2 Momentum conservation equation

The general equation for conservation of momentum can be written as follows:

$$\frac{\partial}{\partial t}(\rho \vec{v}) + \nabla \cdot (\rho \vec{v} \vec{v}) = -\frac{\partial P}{\partial x} + \nabla \cdot (\mu \nabla u) + S_m \qquad \textbf{Equation 10}$$

The left hand side of the equation contains terms as defined for the conservation of mass equation with the right side of the equation containing pressure source term and diffusion source term respectively. In FLUENT, this equation is implemented as:

$$\frac{\partial}{\partial t}(\rho \vec{v}) + \nabla \cdot (\rho \vec{v} \vec{v}) = \nabla P + \nabla \cdot \left(\bar{\bar{\tau}}\right) + \rho \vec{g} + \vec{F} \qquad \textbf{Equation 11}$$

Where P (Pa) is static pressure, $\bar{\bar{\tau}}$ is the stress tensor, $\rho \vec{g}$ is the gravitational body force and $\vec{F}$ is the external body forces.

2.4.2.2.3 Energy conservation equation

The energy conservation equation to be solved is as given below:

$$\frac{\partial}{\partial t}(\rho E) + \nabla \cdot (\vec{v}(\rho E + P)) = \nabla \cdot \left(k_{eff} \nabla T - \sum_i h_i \vec{J}_i + \left(\bar{\bar{\tau}}_{eff} \cdot \vec{v}\right)\right) + S_E \qquad \textbf{Equation 12}$$

In this equation, k_{eff} is the effective thermal conductivity given by: $k_{eff} = k_T + k_t$, where k_t ($WK^{-1}m^{-1}$) is the turbulent thermal conductivity, defined according to the turbulence model being used, k_T ($WK^{-1}m^{-1}$) is thermal conductivity and $\bar{\bar{\tau}}_{eff}$ (Pa) is the effective stress tensor. The first three terms on the right-hand side of **eq. (12)** represent energy transfer due to conduction, species diffusion, and viscous dissipation, respectively. S_E is the energy source

term which includes the heat of chemical reaction, and any other volumetric heat sources defined in the model. In the equation, E (J) is total energy described as in **eq. (13)** below:

$$E = h + \frac{P}{\rho} + \frac{\vec{v}^2}{2} \qquad \textbf{Equation 13}$$

Where h (J) is sensible enthalpy.

2.4.2.2.4 Species conservation equation

For monitoring the species mixing or reactions involved, conservation equations for chemical species equation is solved, predicting the local mass fraction of each species, Y_i, through the solution of a convection-diffusion equation for the ith species. The equation solved is as given below:

$$\frac{\partial}{\partial t}(\rho Y_i) + \nabla \cdot (\rho \vec{v} Y_i) = -\nabla \vec{J}_i + R_i + S_i \qquad \textbf{Equation 14}$$

In this equation, $\vec{J}_i$ is the diffusion flux of species i, which arises due to gradients of temperature and concentration, R_i is the net rate of production of species i by chemical reaction and S_i is the rate of creation by addition from the dispersed phase plus any user-defined sources. In turbulent flows, diffusion flux of species i is computed in the following form:

$$\vec{J}_i = -\left(\rho D_{i,m} + \frac{\mu_t}{Sc_t}\right)\nabla Y_i - D_{T,i}\frac{\nabla T}{T} \qquad \textbf{Equation 15}$$

In this equation, Sc_t is the turbulent Schmidt number $\left(\frac{\mu_t}{\rho D_t}\right)$ where μ_t is the turbulent viscosity and D_t is the turbulent diffusivity, $D_{i,m}$ is the mass diffusion coefficient for species i in the mixture $D_{T,i}$ is the thermal diffusion coefficient and T (K) is reaction temperature. In this work, there are no chemical reactions modeled and as such, the species equation shall be employed to track the spread and dispersion of a tracer through the domain for determining the mixing time hence mixing efficiency of the process.

2.4.2.3 Multiphase modelling

Peirce-Smith Converting process is a complex multiphase system involving four principle fluid phases namely the matte charged, blister copper produced, slag (oxides) formed and the oxygenated air used for oxidation removal of residual iron and sulphur as discussed in **section 2.2.1**. All the four phases are identifiable with distinct particular inertial response to and interaction with the flow and the potential field. Insight into the multiphase flows of such complex systems have been made possible with the availability of two broad approaches for the numerical calculation namely: Euler-Euler (Volume of Fluid model) and Euler-Lagrange (Discrete Phase Model) approaches.

The two approaches differ with respect to the frame of reference used in the handling of different phases. The Volume of fluid (VOF) model employs Eulerian approach that focuses on locations in space and time through which the fluid flows. In contrast, the Discrete phase model (DPM) model applies a Lagrangian approach where attention is focused on individual particles and how they traverse in space and time, each subject to a distinct force balance with overall momentum, mass and energy being transferred between the particles and the surrounding environment (Cloete et al. 2009).

2.4.2.3.1 Volume of Fluid Model (VOF)

The VOF model is a surface-tracking technique applied to a fixed Eulerian mesh. It is designed for two or more immiscible fluids where the position of the interface between the fluids is of interest. In the VOF model, a single set of momentum equations is shared by the fluids, and the volume fraction of each of the fluids in each computational cell is tracked throughout the domain. The different phases are treated mathematically as interpenetrating continua. The concept of phasic volume fraction is introduced since the volume of a phase cannot be occupied by the other phases. These volume fractions are assumed to be continuous functions of space and time and their sum is equal to one. Conservation equations for each phase are derived to obtain a set of equations, which have similar structure for all phases. Empirical information or application of kinetic theory is used to close the equations by providing constitutive relations.

The tracking of the interface(s) between the phases is accomplished by the solution of a continuity equation for the volume fraction of one (or more) of the phases, α. For the qth phase, this equation has the following form:

$$\frac{1}{\rho_q}\left(\frac{\partial}{\partial t}\left(\alpha_q\rho_q\right)+\nabla\cdot\alpha_q\rho_q\vec{v}_q=S_{\alpha_q}+\sum_{p=1}^{n}\left(\dot{m}_{pq}-\dot{m}_{qp}\right)\right)$$ **Equation 16**

In this equation, ρ_q (kgm^{-3}) is the density of qth phase, α_q is the qth phase, $\dot{m}_{qp}$ is the mass transfer from phase q to phase p and $\dot{m}_{pq}$ is the mass transfer from phase p to phase q. The source term on the right-hand side of **eq. (16)** S_{α_q}, is zero, but can be specified for mass source for each phase.

The volume fraction equation will not be solved for the primary phase; the primary-phase volume fraction will be computed based on the following constraint:

$$\sum_{q=1}^{n}\alpha_q=1$$ **Equation 17**

In order to capture the interfaces between fluids, geometric reconstruction scheme using a piece-wise linear approach has been widely used due to robustness, accuracy and general applicability in preference to other schemes such as QUICK, HRIC and CICSAM (ANSYS 2008). It is only applicable to transient (time-dependent) simulations and is the favorable in the current study since we are interested in the numerical solutions in space and time.

2.4.2.3.2 Discrete Phase Model (DPM)

The discrete phase model is a natural extension of particle mechanics which focuses on identifiable material particles as they traverse through and interact with fluid flow in space and time through tracking the motion and computing the rates of change of conserved properties by integrating the force balance on the particle (Versteeg & Malalasekera 2007, ANSYS 2008, Panton 1984). These particles could be bubbles, particles or droplets, capable of exchanging momentum, mass and energy with the fluid phase.

The force balance equates the particle inertia with the forces acting on the particle, and can be written (for the x-direction in Cartesian coordinates) as:

$$\frac{dv_p}{dt}=F_D\left(v_x-v_p\right)+\frac{g_x\left(\rho_p-\rho\right)}{\rho_p}+F_x$$ **Equation 18**

In this equation, ρ_p (kgm^{-3}) is the density of particle, F_x (Nkg^{-1}) is an additional acceleration term, whereas $F_D\left(v_x-u_p\right)$ is the drag force per unit particle mass with F_D being given by:

$$F_D = \frac{18\mu}{\rho_p d_p^2}\frac{C_D \,\mathrm{Re}}{24}$$ **Equation 19**

In this equation, v_x (ms^{-1}) is the fluid phase velocity, v_p (ms^{-1}) is the particle velocity and d_p (m) is the particle diameter. Re is the relative Reynolds number, which is defined as:

$$\mathrm{Re} = \frac{\rho d_p \left| v_p - v_x \right|}{\mu}$$ **Equation 20**

The drag coefficient is calculated by:

$$C_D = a_1 + \frac{a_2}{\mathrm{Re}} + \frac{a_3}{\mathrm{Re}^2}$$ **Equation 21**

In this equation, a_1 , a_2 and a_3 are constants that apply over several ranges of Re for smooth spherical particles.

DPM analysis application is challenging due to the formulation of position vectors as the solids responds to shear stresses whereas the VOF is more useful and computationally affordable. Physical laws written in VOF formulation does not contain the position vectors and the velocity appears as the major variable thereby revealing all fluid flow patterns necessary. This is due to the fact that fluids subjected to shear stress deform continuously as long as the stress is applied (Panton 1984). Usefulness of VOF is however achievable at high computational grid resolution (Cloete et al. 2009).

2.4.2.3.3 Turbulence model

The preceding sections discussed the physical models used to capture the multiphase flow. However, the flow dynamics in submerged gas injection system as the one under current study are turbulent in nature and precludes an economical description of the motion of all the fluid particles due to identifiable structures set up in the flow, referred to as eddies (Merle & David 1997). As such, an additional physical model referred to as turbulence model has to be used to account for the basic turbulent nature of the process.

The evolution to address the turbulence modelling resulted in the birth of the two-equation model (Wilcox 1994) also known as the $k-\varepsilon$ model solving the two transport equations: turbulence kinetic energy (k) and turbulence kinetic energy generation (ε), which capture the small scale and high frequency fluctuations in transport quantities which are computationally expensive to simulate directly. This is achieved by resolution of small scale

eddies through time-averaging, ensemble averaging or direct manipulation resulting in a modified set of equations that are computationally less expensive to solve. The model transport equation for k was mathematically derived whereas the equation for ε was empirically determined.

2.4.2.3.4 The Standard $k-\varepsilon$ (SKE) model

The SKE model is a semi-empirical model that has been widely used in industrial and non-industrial applications due to its robustness, easy on convergence, minimal computational requirements as well as reputable and reasonable accuracy for a wide range of turbulent flows. The turbulence kinetic energy, k (m^2s^{-2}) and its rate of dissipation ε (m^2s^{-3}) is obtained from the following transport equations respectively:

$$\frac{\partial}{\partial t}(\rho k)+\frac{\partial}{\partial x_x}(\rho k v_x)=\frac{\partial}{\partial x_y}\left(\left(\mu+\frac{\mu_t}{\sigma_k}\right)\frac{\partial k}{\partial x_y}\right)+G_k+G_b-\rho\varepsilon-Y_M+S_k \qquad \textbf{Equation 22}$$

$$\frac{\partial}{\partial t}(\rho \varepsilon)+\frac{\partial}{\partial x_x}(\rho \varepsilon v_x)=\frac{\partial}{\partial x_y}\left(\left(\mu+\frac{\mu_t}{\sigma_\varepsilon}\right)\frac{\partial k}{\partial x_y}\right)+\rho C_1\varepsilon-\rho C_2\frac{\varepsilon^2}{k+\sqrt{v_y\varepsilon}}+C_{1\varepsilon}\frac{\varepsilon}{k}C_{3\varepsilon}G_b+S_\varepsilon$$

Equation 23

In these equations, G_k represents the generation of turbulence kinetic energy due to the mean velocity gradients, G_b is the generation of turbulence kinetic energy due to buoyancy, Y_M is the contribution of the fluctuating dilatation in compressible turbulence to the overall dissipation rate, S_k and S_ε the kinetic energy and dissipation source terms respectively. The generation of turbulence kinetic energy due to mean velocity gradients and turbulent viscosity is given by **eq. (24)** and **eq. (25)** respectively where $v_x^{'}$ and $v_y^{'}$ (ms^{-1}) are averaged fluid axial and radial velocity components respectively.

$$G_k=-\rho\overline{v_x^{'}v_y^{'}}\frac{\partial y}{\partial x} \qquad \textbf{Equation 24}$$

$$\mu_t=\rho C_\mu\frac{k^2}{\varepsilon} \qquad \textbf{Equation 25}$$

In literature, the performance of the SKE model application have been reviewed for applications such as unconfined flows, flows with large extra strains, rotating flows as well as

flows driven by anisotropy of normal Reynolds stresses as observed in developed flows in non-circular ducts. The performance in terms of convergence and solution stability were found to be poor according to Versteeg & Malalasekera (2007). In this study, turbulence is important and as such RKE model has been reviewed.

2.4.2.3.5 The Realizable $k-\varepsilon$ (RKE) model

The RKE model is a relatively recent development by Shih et al. (1995) and differs from the SKE model as it contains a new formulation for the turbulent viscosity as well new transport equation for the kinetic energy dissipation rate, ε, that has been derived from an exact equation for the transport of the mean-square vorticity fluctuation thus providing superior performance for flows involving rotation, boundary layers under strong adverse pressure gradients, separation, and recirculation.

In this model, the kinetic energy dissipation rate ε is modeled as:

$$\frac{\partial}{\partial t}(\rho\varepsilon)+\frac{\partial}{\partial x_x}(\rho\varepsilon v_x)=\frac{\partial}{\partial x_y}\left(\left(\mu+\frac{\mu_t}{\sigma_\varepsilon}\right)\frac{\partial k}{\partial x_y}\right)+\rho C_1 S_\varepsilon-\rho C_2\frac{\varepsilon^2}{k+\sqrt{v_y\varepsilon}}+C_{1\varepsilon}\frac{\varepsilon}{k}C_{3\varepsilon}G_b+S_\varepsilon$$

Equation 26

The term "realizable" means that the model satisfies certain mathematical constraints on the Reynolds stresses, consistent with the physics of turbulent flows, a feature which is not available in the SKE model. Initial studies have shown that the realizable model provides the best performance against all the $k-\varepsilon$ model versions for several validations of separated flows and flows with complex secondary flow features (ANSYS 2008).

2.4.2.4 Computational solution

The numerical solution is achieved through three fundamental steps of pre-processing, solving and post-processing. Pre-processing is concerned with the development of the computational domain and mesh (grid) generation as well as defining physical and chemical phenomena to be modelled together with fluid properties definition and appropriate boundary condition specifications. The solver provides an algorithm for integration of the governing equations of fluid flow over the computational domain as discussed in **section 2.4.2.4.4** as well as discretization of the integral equations into a system of algebraic equations which will be solved by iteration methods due to non-linearity. The post-processing will provide the analysis of results interface through versatile data visualization tools.

2.4.2.4.1 Computational grid (mesh)

The subdivision of computational domain into a discrete number of smaller and non-overlapping finite control volumes or computational cells is critical as it affects the output of the simulation. Different approach algorithms are developed for the purposes of grid generation and each approach has to be chosen with a trade-off between computational cost, mesh size, quality and resolving physics as well as the time and effort required for the meshing. As such, selecting the right meshing strategy is a critical task in all numerical analysis.

A structured grid, consisting mainly of hexahedral mesh elements is preferred to an unstructured grid, which mainly contains tetrahedral mesh elements because of its superiority on producing more accurate solutions, greater possibility of flow alignment with the grid coupled with the ability to be anisotropically subdivided without elements quality deterioration. Tetrahedral mesh elements are susceptible to numerical diffusion and higher storage capacity than the hexahedral mesh elements with the same distribution of spacing due to increased number of edges. It could be concluded that the hexahedral mesh elements have reduced cell count with higher mesh quality which translates to faster turnaround time on simulations (ANSYS 2008, Snyders 2008, and Bezuidenhout 2008).

2.4.2.4.2 Numerical accuracy

The numerical accuracy of the solution is governed by the number of computational cells in the flow domain. In general the larger the number of computational cells the better the solution accuracy. Both the accuracy of the solution and its cost in terms of necessary computing power and calculation time are depended on the computational cell fineness. Due to large systems of equations arising from highly refined meshes, iterative techniques are preferred over the direct numerical methods which require higher storage solution overheads (Versteeg & Malalasekera 2007). In addition, the Semi Implicit Methods of Pressure Linked Equations (SIMPLE) algorithm for the continuity and momentum equations coupling is itself iterative in nature and therefore defeats the necessity of very accurate immediate solutions, as long as the iteration process eventually converges to a true and reliable solution.

2.4.2.4.3 Discretization of governing transport equations

Mathematical solutions of governing equations of flow which are nonlinear and coupling is achievable through discretization, which is a control volume based technique to convert the

general scalar transport equations into algebraic equations that can be solved numerically. This control volume technique consists of integrating the transport equation about each control volume, yielding a discrete equation that expresses the conservation law on a control-volume basis. Considering the unsteady conservation equation for transport of a scalar quantity ϕ (such as temperature and turbulence), the integral form for an arbitrary control volume V is as follows:

$$\int_v \frac{\partial \rho \phi}{\partial t} dV + \oint \rho \phi \vec{v} \cdot d\vec{A} = \oint \Gamma_\phi \nabla \phi \cdot d\vec{A} + \int_v S_\phi dV \qquad \textbf{Equation 27}$$

In this equation, $\Gamma_\phi, \nabla\phi, S_\phi$ is the diffusion coefficient, gradient and source of ϕ per unit volume. Discretization of **eq. (27)** on a given computational cell yields:

$$\frac{\partial \rho \phi}{\partial t} V + \sum_f^{N_{faces}} \rho_f \vec{v}_f \phi_f \cdot \vec{A}_f = \sum_f^{N_{faces}} \Gamma_\phi \nabla \phi_f \cdot \vec{A}_f + S_\phi V \qquad \textbf{Equation 28}$$

In this equation, N_{faces} is the number of faces enclosing cell, $\rho_f \vec{v}_f \phi_f \cdot \vec{A}_f$ is the face flux through the face and V is the computational cell volume. When the values from the neighboring cells are required for computation, interpolation of the cell centre values are required and this is achieved through upwind schemes which derives the quantities from the cells upstream. The first and second order upwind schemes have been found useful in all general numerical simulations (Snyders 2008).

2.4.2.4.4 Solvers

Solver algorithms have been developed to cater for different flow fields and fall into two broad categories namely density and pressure based solvers. Pressure based solver have been historically developed for low-speed subsonic incompressible flows (Mach number < 1) while the density based solver was developed for high speed transonic compressible flows (Mach number > 1) in a coupled or segregated (decoupled) manner. In the segregated algorithm, the individual governing equations for the solution variables are solved one after another. Each governing equation, while being solved, is "decoupled" or "segregated" from other equations, hence its name. The segregated algorithm is memory-efficient, since the discretized equations need only be stored in the memory one at a time. Solution convergence, however, is relatively slow, even though the equations are solved in a decoupled manner.

Unlike the segregated algorithm described above, the pressure-based coupled algorithm solves a coupled system of equations comprising the momentum equations and the pressure-based continuity equation. Since the momentum and continuity equations are solved in a closely coupled manner, the rate of solution convergence significantly improves when compared to the segregated algorithm. However, the memory requirement increases by 1.5 - 2 times that of the segregated algorithm since the discrete system of all momentum and pressure-based continuity equations needs to be stored in the memory when solving for the velocity and pressure fields rather than just a single equation, as is the case with the segregated algorithm (ANSYS 2008).

2.4.2.4.5 Under-relaxation

Due to nonlinearity of the equation set being solved in the numerical simulations, it is necessary to control the change of new variable magnitude, θ_{new}. This is typically achieved by under-relaxation of variables (also referred to as explicit relaxation), which reduces the change of θ_{new} produced during each iteration. In a simple form, the new value of the variable θ_{new} within a cell depends upon the old value; θ_{old}.The newly calculated variable value θ_{cal} and the under-relaxation factor, ψ are related as given in **eq. (29)**.

$$\theta_{new} = \theta_{old} + \psi\left(\theta_{cal} - \theta_{old}\right) \qquad \textbf{Equation 29}$$

The variable under-relaxation is used to increase numerical stability also referred to as smoothing.

2.4.2.4.6 Numerical convergence

A successful simulation result is judged by convergence and grid independence. The solution algorithm is iterative in nature and in a converged solution; the so-called residuals are used to measure the overall conservation of flow properties. The residuals should drop to three orders of magnitude when judging convergence. However residual definitions that are useful for one class of problem are sometimes misleading for other classes of problems. Therefore it is beneficial to judge convergence not only by examining residual levels, but also by monitoring relevant integrated flow quantities such as bulk kinetic energy generation, bulk fluid flow velocity or drag.

Progress towards a converged solution can be greatly assisted by careful selection of the settings of various relaxation factors and acceleration devices in the initial model development by generating good quality mesh which relies heavily on the insight into the expected properties of flow. Also convergence can be sped up by focusing the computational effort on the equations of primary importance in the simulation where less important equations can be turned off, focusing on equations of interest.

2.4.3 Physical and Numerical Modelling Combination

Physical and numerical modelling can be applied simultaneously. In most cases, this is done to have comparative evaluation of results where there is limit to validation data due to insufficient information. It can also be done to explain results of another model which cannot be done on it. Simultaneous application of physical and numerical models has been done in gas stirred systems by Vaarno et al. (1998), Han et al. (2001) and Valencia et al. (2006).

In a study focused on better prediction of consequences of modifications made to PSC operations, Vaarno et al. (1998) used numerical simulation in tandem with a scale water model. The numerical model was verified by way of comparison of calculated and measured velocity fields as well as the general dimensions of the plume. Experimental measurements and numerical simulations were found to be in sensible conformity.

Influence of second phase in a gas stirred ladle simulating Vacuum Oxygen Decarburization (VOD) was studied by Han et al. (2001) using a combination of numerical simulation and water model experiments. These authors found that mixing times increased with oil layer as compared to the bath with no oil layer. In the study, transient formation of plume eye was matched with results from water model experiments. Results of water model experiments and numerical simulations were in reasonable agreement.

Valencia et al. (2006) conducted numerical simulations and experimental observations to characterize the fluid flow behavior in a Teniente copper converter. They reproduced characteristics of three-dimensional unsteady flow with numerical simulation which agreed well with experimental observations in a water model. Process characteristics of air turbulent jets, splashing of free surface in the plume, suppression of splashing in the settling zone and displacement of slag to the settling zone, as observed in the PSC, were also visualized in the numerical simulations.

It will be sufficient to conclude that the choice of modelling technique to simulate a process depends on the deliverables being sought. Interpretation or unison functionality of physical and numerical simulation hinges on the problem being addressed and limitations of the models. In this work, physical and numerical simulation will be done harmoniously. Physical model is set up to quantitatively measure the mixing and mass transfer activities in the scale converter with additional visualization benefit of the bodily process. Numerical simulation will give explanation to the observed phenomena of physical experiments through calculation of flow field's variables such as liquid mean velocities, turbulence and phase distributions in space and time which cannot be achieved by the physical model.

2.5 Mixing in Pyrometallurgical Processes

In pyrometallurgical submerged gas injection operations, mixing is achieved by momentum transfer of energy from the blown gas to the liquid where three forms of energy exist namely kinetic, buoyancy and expansion energy. Mixing brings about corporal system homogeneity (Mazumdar & Guthrie 1986, Nakanishi et al. 1975). If proper mixing is not achieved in the reactors, three fundamental consequences results namely:

a) Chemical and thermal inhomogeneties
b) Particulate inhomogeneties
c) Undesirable variability in the final product composition

Mixing time, T_{mix}, which is defined as the time interval required to achieve uniform and homogeneous steady state concentration of the bath after introducing a tracer with an acceptable standard deviation from uniform concentration is normally used to ascertain the efficiency of mixing in metallurgical vessels. The subsequent section reviews studies conducted and approaches employed to study mixing in gas injection metallurgical systems.

2.5.1 Mixing Efficiency

Mixing efficiency by definition is the ease with which the system attains physical equilibrium of phases. Literature sources have revealed that mixing can be quantitatively evaluated for pyrometallurgical operations using a variety of techniques employing physical and numerical simulations. The approaches in the fore-mentioned techniques are aligned with macroscopic

evaluation of mixing efficiency of the systems. The subsequent sections will review the two different techniques.

2.5.1.1 Mixing efficiency-Physical modelling

Physical experiments have been conducted using water model experiments to study the mixing efficiency in submerged gas injection systems. Mixing time measurements were done using a variety of measurement techniques such as tracer dispersion technique (Sinha & McNallan 1985, Nyoka et al. 2003, Nakanishi et al. 1975, Akdogan & Eric 1999), photocell technique (Stapurewicz & Themelis 1987) and electrical conductivity technique (Mazumdar & Guthrie 1986), all employing the strategy of monitoring the concentration distribution of the tracer at one location to reach a defined steady state concentration after addition at a predetermined location. **Figure 2** shows the results of studies by Stapurewicz & Themelis (1987) using photocell technique. In this figure, τ shows the time taken for the transmittance to light of the water after introduction of dye (tracer) to a steady state value giving the mixing time, T_{mix} .

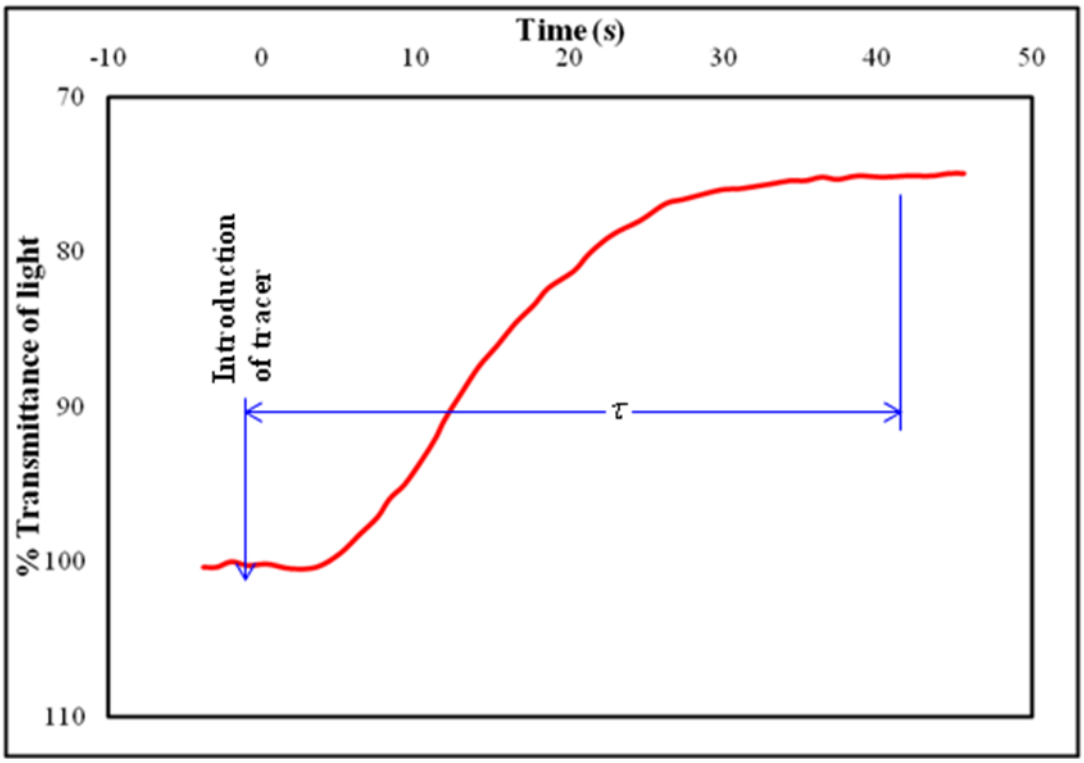

Figure 2: Change of transmittance after tracer injection - Redrawn from Stapurewicz & Themelis (1987)

Mixing time measurements studies have revealed that the value of mixing time is dependent on a variety of factors namely; number of injections, geometry, bulk liquid quantities, tracer monitoring point, tracer addition point, the presents of overlaying organic phase (simulated slag) and the mixing power of the system under consideration. Academic studies by Stapurewicz & Themelis (1987), Ramirez-Argaez (2008), Han et al. (2001), Nyoka et al. (2003), Mazumdar et al. (1988), Turkoglu & Farouk (1991), Zhu et al. (1996) and Wei (2002) outline the detailed information of the fore-mentioned factors that affect the mixing time in the systems which translates to the vessel contents turnaround time. However the subsequent section will discuss the mixing power input to submerged gas injection system as it shall be used in the interpretation of the experimental results in this work.

2.5.1.1.1 Specific mixing power

By definition, specific power is power to weight ratio. In gas bubble stirred driven systems; total power for mixing (specific mixing power) to the system is a summation of power due to buoyancy force, gas bubble volumetric work and gas kinetic energy (Gray et al. 1984, Stapurewicz & Themelis 1987, Nakanishi et al. 1975). Through integration of summation of work done by buoyancy and work done by rising bubble in gas systems assuming ideal gas behavior in limits of injection submergence, H_s (m), buoyancy specific power, ε_b (kWton^{-1}) is given by:

$$\varepsilon_b = \frac{2QP_a}{W}\ln\left(1+\frac{\rho g H_s}{P_a}\right) \qquad \textbf{Equation 30}$$

Kinetic energy specific power due to gas injection ε_k (kWton^{-1}) is given by:

$$\varepsilon_k = \frac{\rho_g Q^3}{2WA^2} \qquad \textbf{Equation 31}$$

Where W (kg) is effective bath weight, Q (Nm^{3}s^{-1}) is total gas flow rate, P_a (kPa) is atmospheric pressure and A (m^2) is total tuyere cross sectional area.

The total specific mixing power, ε_m to the system is an algebraic summation of buoyancy and kinetic energy specific power given by:

$$\varepsilon_m = \varepsilon_b + \varepsilon_k \qquad \textbf{Equation 32}$$

The relative contribution of buoyancy and kinetic energy specific power varies with the process under consideration but generally, buoyancy surpasses kinetic energy which is

instantaneously dissipated close to the tuyere at the exit into the bath. However it is instructive to mention that in non-ferrous converters, mixing time have been investigated in terms of the power input by the injected gas. It was found that the relative contribution of the kinetic energy can be as high as in ferrous processes though the liquid seal depth is shallow with very small bubble dispersion zone (Gray et al. 1984).

2.5.1.1.2 Mixing time correlations

Mixing time correlations for various metallurgical processes has been well documented in literature using water models (Sinha & McNallan 1985, Gray et al. 1984, Mazumdar & Guthrie 1986, Stapurewicz & Themelis 1987, Nyoka et al. 2003, Nakanishi et al. 1975). The results of mixing time of the systems have been expressed as a function of physical field flow variables in singular or in interactive manner. Main field flow variables that have been used to correlate mixing time are:

a) Total specific mixing power, ε_m

b) Air volumetric flow rate, Q

c) Submergence of injection, H_s

d) Liquid (bath) depth, H_b

The generalized correlation of mixing time is thus;

$$T_{mix} = f(\varepsilon_m, Q, H_s, H_b) \qquad \textbf{Equation 33}$$

There is a relationship between buoyancy specific power, ε_b and volumetric gas flow rate as given in **eq. (30)** which provides the major driving force for mixing and mass-transfer and thus a mention has to be made of total specific mixing power. The formulation of total specific mixing power have come in different forms and the inclusion and/or exclusion of specific mixing power due to gas kinetic energy, ε_k has resulted in no single blanket mixing time correlation for all systems studied.

The exclusion has been based on the basis that all the kinetic energy is expended at the tuyere exit. This is reasonable for deep submergence as ladle metallurgy studies. In shallow submergence, it is expected that the kinetic energy contributes to the bath stirring as there is minimal gas-liquid retention time. As such, in the current studies, kinetic energy, ε_k due to gas injection will be considered and formulated into the total specific mixing power, ε_m.

Table 2 gives a summary of mixing time studies conducted in ferrous pyrometallurgical simulations, techniques employed and mixing time formulations used. The current study is a first attempt to address physical simulation mixing time studies for the PSC and as such, there are no correlations developed and found in literature.

2.5.1.2 Mixing efficiency-Numerical modelling

Numerical modelling studies have been employed to study mixing efficiency in both steel making operations as well as PSC by tracer concentration dispersion in the gas stirred vessels, which is quantified by mixing time through numerical solution of conservation equations for chemical species by predicting the local mass and/or mole fraction of each species, through the solution of a convection-diffusion equation for the species as given by **eq. (14)** and the liquid circulation rate.

In this work, no chemical reactions are modelled and as such the species transport equation will be solved to track the concentration of the added species in space and time at a predetermined measuring point.

Turkoglu & Farouk (1991) pointed out that liquid bulk circulation rate is inversely proportional to mixing time which indicates that the bulk motion of the liquid plays an important role in mixing which also suggests that liquid recirculation rate can be used as a measure of mixing efficiency. As such a combination of species transport equation solution and numerical calculations of integral bulk flow quantities can effectively be utilized to quantify mixing in gas injected systems.

2.5.1.2.1 Mixing time-Tracer concentration dispersion

Three studies have been found in literature that employed numerical mixing time simulations solving species conservation transport equation. Mixing time was defined in these simulations as the total time taken for dispersion of tracer initial concentration to reach predetermined steady state equilibrium concentration on all nodes in the computational domain.

Reference	Specific mixing power expression (kWton^{-1})	Mixing time measurement technique used	Defined % mixing	Specific gas volumetric flow rate (m^{3}s^{-1}ton^{-1})	Simulated slag considered	Mixing time correlation derived
(Nakanishi et al. 1975)	$\frac{0.0285QT}{W}\log\left(1+\frac{L}{48}\right)$ L(cm), Q(Nlmin^{-1}), W(ton)	pH	-	0.00025 – 0.001	No	$T_{mix}=800\varepsilon_b^{-0.4}$
(Sinha & McNallan 1985)	$\frac{854QT}{W}\log\left(1+\frac{\rho g H_s}{P_a}\right)+\frac{\rho_g Q^3}{2WA^2}$ L(m), Q(m^{3}s^{-1}), W(ton)	pH	97.7	0.000335 – 0.00667	No	$T_{mix}=692\varepsilon_b^{-0.89}$ $T_{mix}=501\varepsilon_m^{-0.46}$
(Mazumdar & Guthrie 1986)	$\frac{gQ}{\pi R^2}$ Q(Nm^{3}s^{-1})	Electrical conductivity	95	0.0002 – 0.001	No	$T_{mix}=37\varepsilon_b^{-0.33}L^{-1}R^{1.66}$
(Stapurewicz & Themelis 1987)	$\frac{742QL}{W}\ln\left(1+\frac{H}{C}\right)$ H(m), Q(m^{3}s^{-1}), W(ton)	Photocell	95	0.00217 – 0.016	No	$T_{mix}=164\varepsilon_b^{-0.39}H^{-0.39}$
(Akdogan & Eric 1999)	$\frac{0.0145QT}{W}\log\left(1+\frac{H}{1033.9}\right)+\frac{\rho_g Q^3}{2WA^2}$ L(cm), Q(Nlmin^{-1}), W(ton)	pH	99.7	0.12 – 0.293	Yes	$T_{mix}=5528.7\varepsilon_m^{-0.33}$ (off-center) $T_{mix}=3502.3\varepsilon_m^{-0.27}$ (center)
(Nyoka et al. 2003)	$\frac{854QT}{W}\log\left(1+\frac{\rho g H_s}{P_a}\right)+\frac{\rho_g Q^3}{2WA^2}$ L(m), Q(m^{3}s^{-1}), W(ton)	pH	95	0.0667 – 0.12	No	$T_{mix}=1.08Q^{-1.05}W^{0.35}$

Table 2: Summary of mixing time studies conducted in steel making operation vessels

Turkoglu & Farouk (1991) studied the effects of bath aspect ratio and gas injection rates on mixing characteristics in a steel making ladle employing a tracer with the physical properties of steel using the species transport equation solution. The main conclusion in their study was that mixing power increases with increase in bath height (tuyere submergence). Later study by Zhu et al. (1996) employed the same principle and conditions to study the effects of gas flow rate, nozzle position and inclined wall on flow patterns and mixing in steel making ladle. The conclusion from the study was that nozzle position and tracer addition points affects mixing time. In a recent study, Ramirez-Argaez (2008) used species transport equation to model mixing in a industrial ladle furnace using one-sixth scaled water physical model and proposed mixing time as a function of the main process variables. Using multilineal regression, which is valid for one and two tuyeres, he developed the correlation as given below:

$$T_{mix} = 3.41 W^{0.3} (NT)^{0.4} Q^{-0.25} \left(\frac{r}{R}\right)^{-0.12} \left(\frac{H}{D}\right)^{-0.44} \qquad \textbf{Equation 34}$$

In this equation, NT is the number of tuyeres. This study presents the first attempt to model mixing in a PSC using species transport equation to gain fundamental and pertinent information about flow behavior in this metallurgical vessel.

2.5.1.2.2 Mixing time-Integral Fluid flow quantities

The calculation of fluid flow integral quantities have been applied in many numerical modelling of industrial systems to study mixing characteristics because bulk motion of the liquid plays an important role in mixing as revealed by Turkoglu, Farouk (1991).

In a study to gain understanding of flow patterns and characteristics in a gas stirred ladle with simulated slag thickness, Han et al. (2001) used numerical simulations coupled with water model experiments. Through calculation of water bulk recirculation speeds in space and time and matching with the behaviour of the plume eye, the work concluded that simulated slag presence resulted in extended mixing times over the entire gas flow rates employed in the study. First attempt to directly study mixing in a PSC was the work of Valencia et al. (2004) where they numerically calculated inlet air power and the output mean specific energy, turbulent kinetic energy and dissipation rate in water model experiments. **Table 3** gives the results of their work.

Inlet air power, E_i (W)	Mean specific energy, $\frac{1}{2}\rho_l v_t^2$ (Jm^{-3})	Mean turbulent kinetic energy, $\rho_l k$ (Jm^{-3})	Mean turbulent kinetic energy dissipation rate, $\rho_l \varepsilon$ (kWm^{-3})
14.0	24	25	119
25.5	26	35	1374
44.0	48	45	4430
70.0	38	50	300

Table 3: Mixing efficiency evaluation results - Adapted from Valencia et al. (2004).

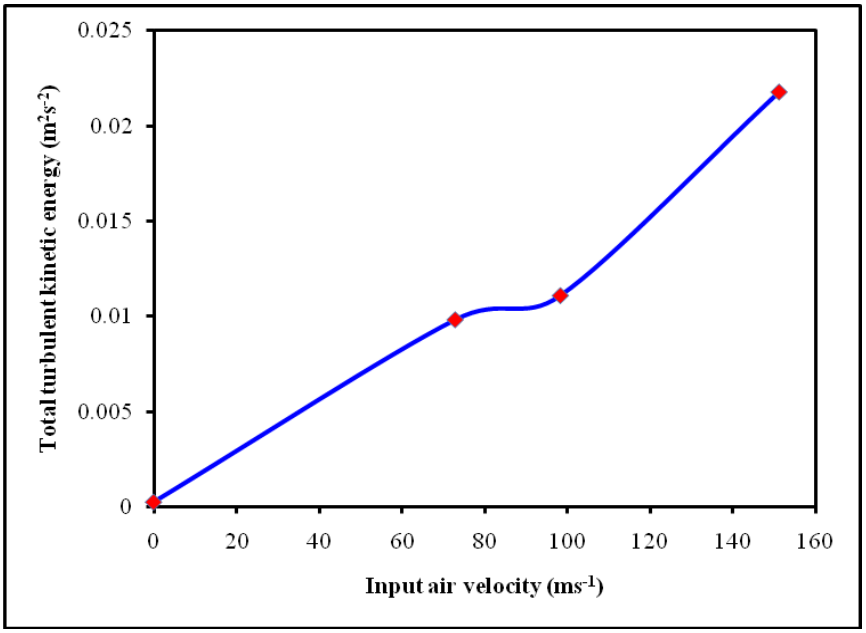

Figure 3: Turbulence kinetic energy with respect to input air velocity - Redrawn from Real et al. (2007)

Analysis of **Table 3** revealed that mean specific energy of the bath does not increase considerably with the increase in inlet air power. However the increase is significant in turbulence and its dissipation which serves to show that most of the air power is expended in turbulence generation rather than generation of bath recirculation speeds. This is contrary to

the high submergence processes where power of mixing has been observed to increase at higher gas injection rates.

Findings by Valencia et al. (2004) were confirmed by recent studies by Real et al. (2007) and Gonzalez et al. (2008) whose works evaluated mixing in PSC using calculated integral quantities of turbulent kinetic energy and copper bath average velocity respectively. Major conclusion in Real et al. (2007) was that turbulent kinetic energy increases with increase in air inlet velocity as shown in **Figure 3.** Results have shown that high inlet velocities are not necessary to obtain adequate copper matte mixing conditions as normalization of turbulent kinetic energy with inlet air velocity resulted in minima at input air velocity of $100ms^{-1}$ as shown in **Figure 4**. This figure shows poor mixing conditions in the converter at higher air inlet velocity.

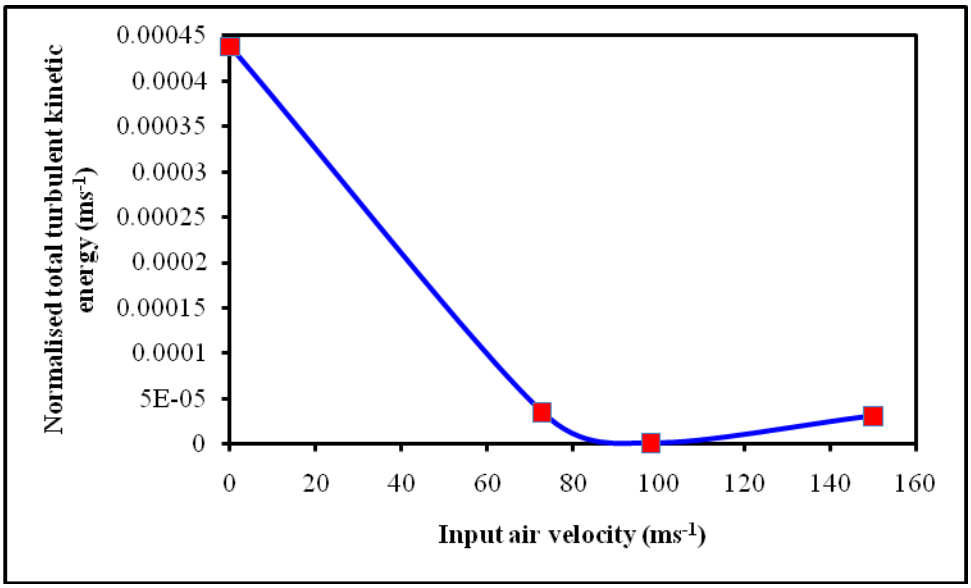

Figure 4: Normalized turbulence kinetic energy with respect to input air velocity - Redrawn from Real et al. 2007)

Gonzalez et al. (2008) analyzed mixing in a PSC converter employing bottom injection by calculation of copper bath average velocity as shown in **Figure 5**. Cases A, B and C where simulated with bottom input air velocities of $5ms^{-1}$, $25ms^{-1}$ and $50ms^{-1}$ respectively with Case D simulated with lateral (side-blown) input air velocity of $50ms^{-1}$. The study revealed that the bulk average flow velocity is oscillatory in nature with amplitude of oscillations increasing with input air velocity. Observation of interest in the study is that Case D, which is typical PSC injection practice, though at one-third of current operating conditions, displayed almost sustained rise of the copper bath mean velocity.

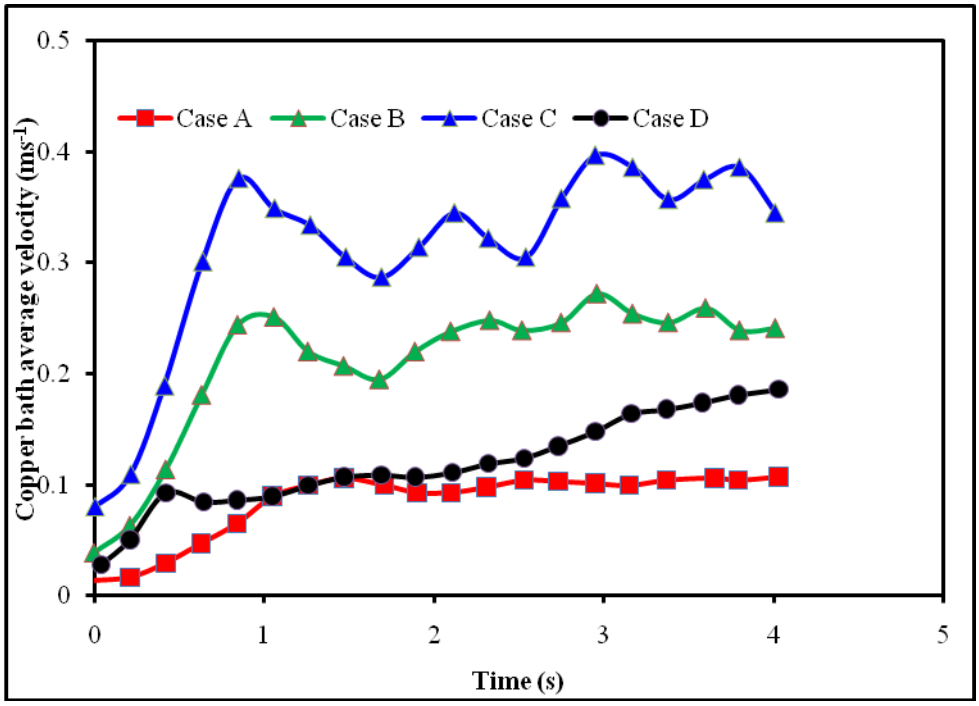

Figure 5: Bath average velocity with respect to input air velocity - Redrawn from Gonzalez et al. (2008)

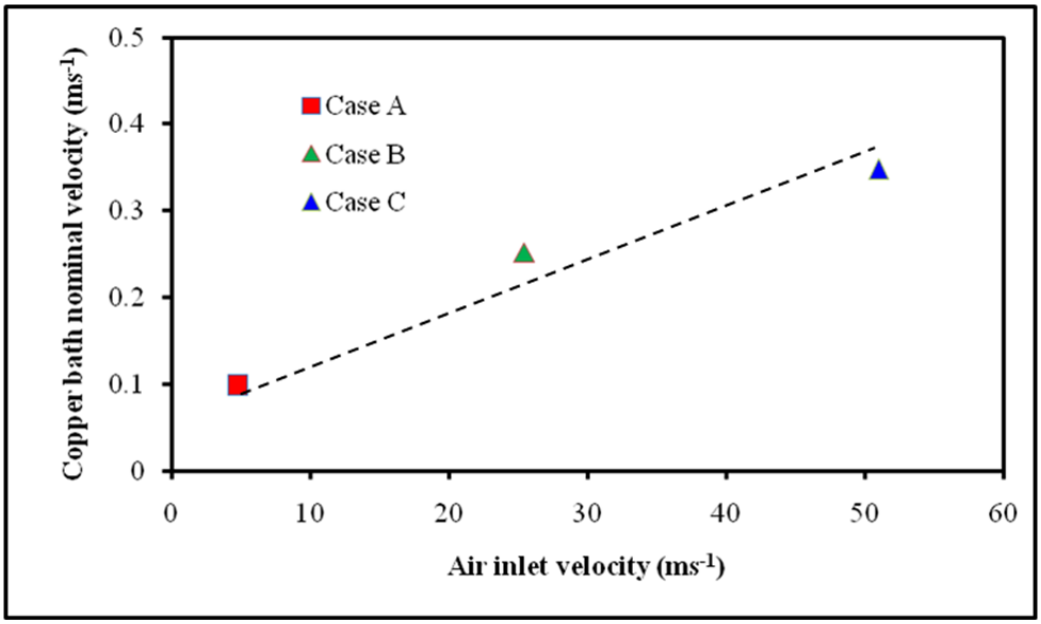

Figure 6: Bath nominal velocity with respect to input air velocity - Redrawn from Gonzalez et al. (2008)

Furthermore, the relationship between air inlet velocity and bath mixing was shown to be non-linear as revealed by calculated copper bath nominal velocities in **Figure 6**.

2.6 Mass Transfer in Pyrometallurgical Processes

Pyrometallurgical processes are multiphase in nature as discussed in **section 2.4.2.3** involving gas-liquid-solid interactions. In the Peirce-Smith converter, the additions of fluxing agents in the form of silica for slag liquefaction and cold process scrap and reverts for temperature control as well as utilization of scrap is a common practice. It is a reasonable postulation that with such practice, solid-liquid mass transfer step may play an important role in the performance and turnaround time of the process. As such, accurate knowledge of this step is thus essential for a fundamental understanding of the process.

2.6.1 Solid-Liquid Processes

Literature pertaining to solid-liquid mass transfer in ladle metallurgy is fairly comprehensive with studies have been conducted by Stapurewicz & Themelis (1987), Szekely et al. (1979), Arters & Fan (1986), Nikov & Delmas (1987) and Prakash et al. (1987). No studies have appeared in literature to the PSC operations. In these studies, mass transfer data has been expressed in the form of dimensionless numbers, often in the form of power series (Arters & Fan 1986).

The Sherwood number, *Sh* which represents the ratio of convective to diffusive mass transport relating the physical properties of the system to the mass transfer coefficient have been frequently used. The major challenge in the development of classical correlations for the translator flows encountered in these submerged gas injection processes to yield more realistic connection between the hydrodynamic phenomena and transport rates (Singh & Mazumdar 1997). In order to estimate mass transfer rates in gas stirred systems effectively, functional relationships embodying the combined influence of flow and turbulence have been proposed. The subsequent section discusses the mass transfer measurements and correlations found in literature.

2.6.2 Mass Transfer Correlations

Experimentally, dissolution of a solute into solvent is the simplest and most popular method for determining solid-liquid mass transfer data (Arters & Fan 1986). Several correlations have been developed by different researchers such as Szekely et al. (1979), Koria (1988) and Mazumdar et al. (1990) using the Sherwood number as given in **Table 4** below using elevated temperature and ambient water model experiments.

The correlations are specific to the experimental condition and as such are not generally applicable. Singh & Mazumdar (1997) using purely experimental technique employing observations of dissolution rates of solid benzoic acid compacts in aqueous gas bubble driven system, assessed the adequacy and appropriateness of the various Sherwood number based correlations. This work conclusively recommended that the correlation by Mazumdar et al. (1990) given in **eq.(35)** is likely to provide reasonable estimates of solid-liquid mass transfer rates in gas bubble systems due to the observed measured and predicted distribution of flow parameters and various dimensionless groups notably, $(\mathrm{Re}_{loc,r})$, (Re_t) and (Sc) with the application of this equation.

$$Sh = 0.73(\mathrm{Re}_{loc,r})^{0.25}(\mathrm{Re}_t)^{0.32}(Sc)^{0.33} \qquad \textbf{Equation 35}$$

Reference	Correlation	Experimental technique and remarks
(Szekely et al. 1979)	$Sh = 2 + 0.7(\mathrm{Re})^{0.5}(\mathrm{Re}_t)^{0.25}(Sc)^{0.33}$	Graphite rods dissolution rates dipped in molten steel-Elevated temperature operation
(Koria 1988)	$Sh = 0.079(\mathrm{Re})^{0.7}(Sc)^{0.356}$	Oxalic acid compacts dissolution rates in aqueous bath-room temperature operation
(Mazumdar et al. 1990)	$Sh = 0.73(\mathrm{Re}_{loc,r})^{0.25}(\mathrm{Re}_t)^{0.32}(Sc)^{0.33}$	Benzoic acid cylinder compacts dissolution rates in aqueous bath-room temperature operation

Table 4: Liquid-solid mass transfer correlations developed

In this equation, (Sh), $(\mathrm{Re}_{loc,r})$, (Re_t), (Sc) is the Sherwood number, local nominal Reynolds number, local turbulent Reynolds number and Schmidt number respectively.

Sherwood number is mathematically expressed as:

$$Sh = \frac{KD}{D_o} \qquad \textbf{Equation 36}$$

In this equation, K (ms^{-1}) is the mass transfer coefficient; D (m) is characteristic diameter and D_o is diffusivity respectively.

The expressions for local nominal Reynolds number and local turbulent Reynolds number are given below:

$$\mathrm{Re}_{loc,r} = \frac{d\rho_f \sqrt{v_x^2 + v_y^2}}{\mu_f} \qquad \textbf{Equation 37}$$

$$\mathrm{Re}_t = \frac{d\rho_f v_x}{\mu_f} \qquad \textbf{Equation 38}$$

In these expressions, $d, v_x, v_y, \mu_f, \rho_f$ is the tuyere diameter, axial component of flow velocity, radial component of flow velocity, fluid viscosity and fluid density respectively.

Schmidt number which is defined as the ratio of momentum diffusivity (viscosity) and mass diffusivity is commonly used to characterize fluid flows in which there are simultaneous momentum and mass diffusion convection process. It is given by:

$$Sc = \frac{\mu_f}{\rho_f D_o} = \frac{\nu}{D_o} \qquad \textbf{Equation 39}$$

In this equation, ν (m^2s^{-1}) is the kinematic viscosity.

All solid-liquid mass transfer reviewed has studied the influence of blowing conditions and size of solid additions on the rate of dissolution, with the major conclusions that increase in flow rate increases mass transfer rates with the rate of mass transfer coefficients being independent of particle size (Nikov & Delmas 1987). It is worth noting that no realistic attempts have been made to ascertain the influence of overlaying slag on solid-liquid mass transfer process which is associated with smelting, converting and refining operation.

Akdogan & Eric (1999) instead investigated the effects of bath stirring on the steel – slag reactions shedding light on the dependence of mass transfer parameter on operating system variables with simulated slag phase. Their work focused on liquid-liquid mass transfer mechanism and concluded that mass transfer rates from simulated steel to simulated slag of an injected tracer increases with increasing agitation rates.

2.7 Project Specific Objectives

It has been observed that physical modelling could be effectively used to investigate and unveil pertinent information in all metallurgical processes. On the basis, this will work will present a first attempt to understand solid-liquid mass transfer rates in a Peirce-Smith converter model. Numerical simulations employing computational fluid dynamics will be used to explain physical experimentation findings. In so far as the scope is concerned, the work will focus on answering key questions.

2.7.1 Project key questions

- ✓ Is it possible to characterize fluid flow behavior in the PSC using physical and numerical modelling?
- ✓ Do phase interactions in the PSC affect fluid flow behavior, mixing and mass transfer efficiency?
- ✓ Is computational fluid dynamics (CFD) capable of interpreting physical modelling results trends?

The subsequent chapter outlines experimental and model development of this work.

2.7.2 Project hypothesis

Phase interactions have influence on fluid flow dynamics in the converter.

CHAPTER 3

EXPERIMENTAL METHODS

3. INTRODUCTION

The experimental methods section outlines the detailed presentation of experimental developments for physical modelling and numerical simulation. Moreover, this section highlights and discusses major considerations and assumptions made with overall objective to produce simulation results that could be used to shed some lights on process challenges and possible solutions.

3.1 Physical Simulation and Model Development

The water bath model developed would be used for physical experimentation to characterize mixing and mass transfer phenomena in the converter using fundamental modelling techniques through the application of similarity criterion.

3.1.1 Dynamic similarity

A rigorous physical model was developed for studying mixing and mass transfer in a typical generic Peirce-Smith converter used in the copper making industry with the objective of direct extrapolation of results to the commercial unit. During the development of the physical model under current study, geometrical, dynamic and kinematic similarity was considered. Geometric similarity was observed by scaling down physical measurements of the typical converter by a scale factor $\lambda = 0.2$. Dynamic similarity which gives blowing parameters of the water bath was observed by using Modified Froude number, N_{Fr}^{*} given by:

$$N_{Fr}^{*} = \frac{v_t^{\,2}\rho_g}{g(\rho_l - \rho_g)d_o} \qquad \textbf{Equation 40}$$

To ensure that dynamic similarity is the same between prototype (real PSC) and model, N_{Fr}^{*} equality should exist as given by **eq. (41)**.

$$\left(N_{Fr}^{*}\right)_{ptype} = \left(N_{Fr}^{*}\right)_{model} = 12.45 \qquad \textbf{Equation 41}$$

Eq. (41) can be simplified to:

$$\left(\frac{v_t^{\,2}\rho_g}{g\left(\rho_l-\rho_g\right)d_o}\right)_{ptype} = \left(\frac{v_t^{\,2}\rho_g}{g\left(\rho_l-\rho_g\right)d_o}\right)_{model} = 12.45 \qquad \textbf{Equation 42}$$

Taking into consideration that;

$$v_t = \frac{Q}{A} = \frac{4Q}{\pi d^2} \qquad \textbf{Equation 43}$$

Then;

$$\left(\frac{Q^2\rho_g}{\left(\rho_l-\rho_g\right)d^5}\right)_{ptype} = \left(\frac{Q^2\rho_g}{\left(\rho_l-\rho_g\right)d^5}\right)_{model} \qquad \textbf{Equation 44}$$

$$Q_{model} = \sqrt{\left(\frac{\rho_l-\rho_g}{\rho_g}\right)_{model}} \cdot \sqrt{\left(\frac{\rho_g}{\rho_l-\rho_g}\right)_{ptype}} \cdot \sqrt[5]{\left(\frac{d_{model}}{d_{ptype}}\right)} \cdot Q_{ptype} \qquad \textbf{Equation 45}$$

Substituting physical quantities into **eq. (45)** yields,

$$Q_{model} = 0.01066 Q_{ptype} \qquad \textbf{Equation 46}$$

In the development of the blowing parameters for the model, injection Modified Froude number was used assuming normal conditions at standard temperature and pressure (S.T.P). However, in working systems, temperature and tuyere pressure significantly affect gas densities. Temperature and pressure correction calculations to derive the injection parameters were developed and are presented in **Appendix A1.**

Temperature and pressure corrected calculation of model to prototype air volumetric flow rate equivalency yielded:

$$Q_{model} = 0.0091 Q_{ptype} \qquad \textbf{Equation 47}$$

Scaling factor coefficient of **eq. (46)** and **eq. (47)** had a standard deviation of 0.11% and as such an average of the two was taken to derive the blowing conditions in the model. Typical industrial PSC dimensions were adopted from the work by Vaarno et al. (1998). A summary of comparative data for dimensions and blowing parameters for typical real PSC and developed water model are given in **Table 5**. The pictorial assembly of the developed water bath model of a Peirce-Smith converter is shown in **Figure 7**.

Figure 7: Pictorial assembly of the developed water bath model of a Peirce-Smith converter

3.1.2 Kinematic Similarity

In order to capture the rates of change of motion of fluid flow (velocity gradients) between the prototype and the model fluids, a dimensionless number known as the Morton number, N_{Mo}, was used.

Component	Parameter	Prototype	Model
Injected air	Volumetric flow rate, Nm^3s^{-1}	7.55	0.005-0.015
	Density, kgm^{-3}	1.2	1.2
Liquids	Mass, kg	144247	135
	Height, m	1.36	0.27
	Volume, m^3	31.4	0.14
	Density, kgm^{-3}	4600	998
	Temperature, K	1493	292
Tuyeres (Nozzles for air injection)	Number	42	7
	Spacing, m	0.205	0.1
	Diameter, m	0.041	0.008
	Gas velocity, ms^{-1}	138.5	14.2-42.6
	Submergence, m	0.52	0.11
Geometry	Inner diameter, m	3.46	0.69
	Length, m	9.14	1
	Filling ratio	0.39	0.39
Flow dimensionless numbers	Modified Froude number	12.45	12.45
	Reynolds number	475155	7175-21524
Flow specific values	Specific volumetric flow rate, s^{-1}	0.23	0.036-0.11
	Specific power of buoyancy, $kWton^{-1}$	2.07	0.08-0.23
	Specific power of gas kinetic energy, $kWton^{-1}$	0.56	0.004-0.12

Table 5: Summary of dimensions and blowing parameters for prototype and model

It incorporates viscosity, surface tension and density was applied to primary fluids of interest. In this work the copper matte at converter operating temperatures and water at ambient temperature physical properties as given in **Table 6** were used to calculate the Morton number using **eq. (8).**

The Morton number equivalence of the two fluids indicates that water exhibits similar fluid streamlines as copper matte at the operational temperatures as such in this study, water will be used to simulate matte. Kerosene which is an organic phase will be used to simulate slag in this work and the physical properties are as given in **Table 6**. Converter slag physical properties were extracted from the works of Davenport et al. (2002) and Vaisburd et al. (2002).

System component	**Physical properties**			**Morton Number**
	Density, ρ kgm^{-3}	**Viscosity, μ Pas**	**Surface tension, σ Nm^{-1}**	
Copper matte	4600	0.01	0.93	2.65 x 10^{-11}
Water-Simulated matte	998	0.001	0.0718	2.65 x 10^{-11}
Converter slag	3500	0.06	0.40	5.67 x 10-7
Kerosene-simulated slag	774	0.00115	0.0275	1.07 x 10^{-9}

Table 6: Physical properties of converter matte, converter slag, water and kerosene

The density ratios of converter slag to converter matte and kerosene and water are 0.717 and 0.775 respectively presenting some veracity on the choice of the simulating fluids. In the body of this work, water and kerosene used will be referred to as simulated matte and simulated slag respectively.

3.1.3 Experimental measurements

The experimental schedule consisted of mixing time measurements in the model using a tracer dispersion technique employing acid concentration diffusion measurements with time and solid-liquid mass transfer using benzoic acid sintered cylindrical compacts. Controlled variables in the experiments were air volumetric flow rate and simulated slag thickness. Both experimental works were conducted in the same ranges of the controlled variables.

3.1.3.1 Mixing time experiments

The developed model of the Peirce-Smith converter was used in these experiments. Critical in any mixing time measurements is the location of the tracer addition position and monitoring point that would give a true reflection of unbiased mixing as it has been found that these positions greatly affect the mixing time. In this work, we used the similitude criterion to have the tracer addition point.

In a typical Peirce-Smith converter, an aperture in the center of the converter serves as the opening through which molten matte, internal reverts like ladle skulls, copper scrap, siliceous and/or basic flux and anode scrap are charged. As such, the central spot in the converter model was chosen as the tracer injection point, 100mm below the simulated matte interface. Due to symmetrical issues, the tracer diffusion monitoring point was located at one end on the model, 100mm from the circular side walls and 100mm below the simulated matte-simulated slag interface. **Figure 8** shows the schematic arrangement of experimental apparatus in the mixing time experiments, showing the pH probe and tracer addition point positions.

3.1.3.2 Measuring time measurement methods

Literature sources have revealed three main tracer monitoring techniques to find mixing time in physical experimentation as discussed in **section 2.5.1.2**. In this work, pH measurement technique was used as best option against the conductivity technique which was reported to have poor data reproducibility in flow rates with narrow spacing levels as observed and proved by Nyoka et al. (2003). Distinct tracer additions of approximately 6ml of concentrated sulphuric acid were injected into the central spot of the model as pointed out in **section 3.1.3.1** at approximately 100mm below the simulated matte-simulated slag interface as shown in **Figure 8**, when the required air flow rate has reached a steady state value within +/-1% of the required value and simulated slag thickness added.

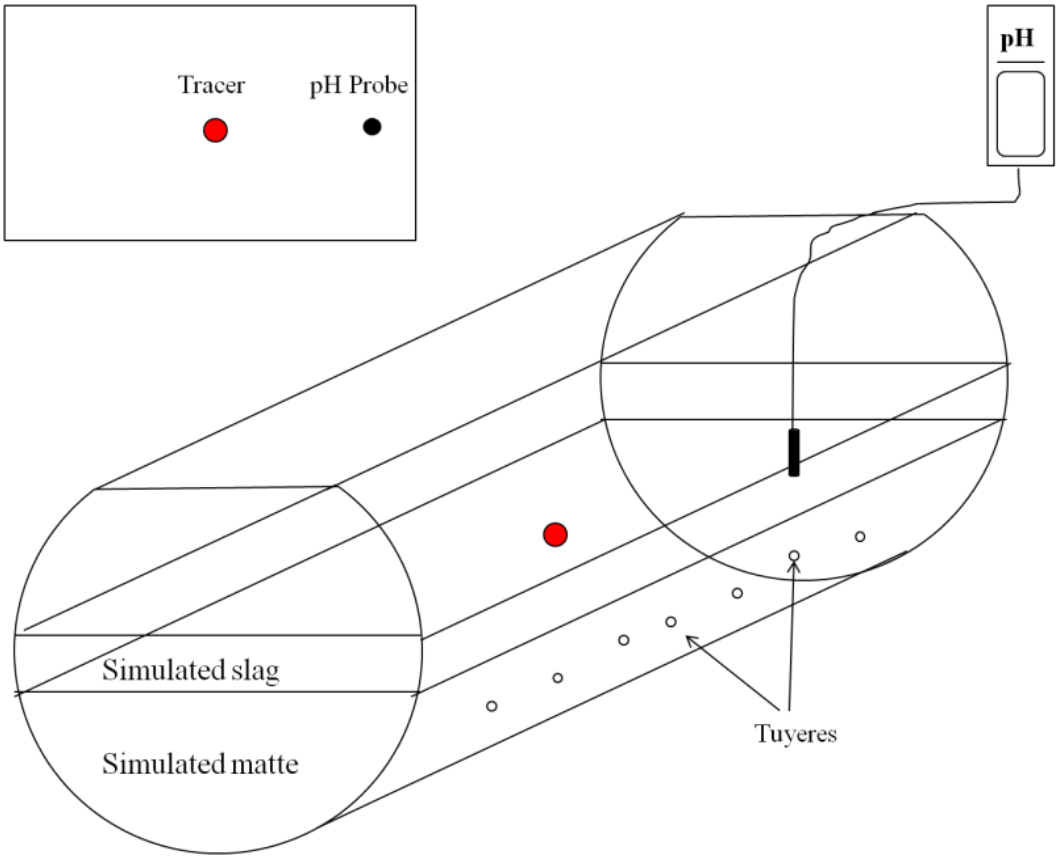

Figure 8: Schematic 3-D view of the model showing tracer and pH probe arrangement as used in the mixing experiments

The mixing time, T_{mix} was defined as the time in which the tracer concentration in the water falls within around 1% of the steady-state concentration. Mixing was considered complete when the pH of the solution had stabilized to within +/-0.01 pH units. This corresponds to a mixing degree of about 99%. The air flow rate, Q, was varied from 0.000875Nm^{3}s^{-1} to 0.01375m^{3}s^{-1}, which were determined via dynamic similarity. Q was varied at five equidistant levels with the calculated industrial Peirce-Smith converter blow rate equivalence of 0.01125Nm^{3}s^{-1} as the central point. Likewise, the simulated slag thickness SS_t was ranged from 0mm to 108mm in five equidistant levels. The highest simulated slag thickness represented 40% relative to the simulated matte height in the model.

In order to reduce experimental error, each experimental condition was repeated five times and mixing time was taken as the average of the runs which were all had reproducibility within 9% standard deviation. This experimental plan yielded a matrix of 125 experiments. The actual dimensions of the converter model are given in **Table 5** in the geometry and

tuyere (air injection nozzles) component sections of the table. The straight bore injection tuyeres were made flush with the converter side walls.

3.1.3.3 Solid-liquid mass transfer experiments

Cylindrical benzoic acid sintered compacts were used in the mass transfer experiments employing the same air volumetric flow rates and simulated slag thickness as used in the mixing time measurement experiments. Due to low sublimation temperatures for commercial grade benzoic acid flake, production of the solid compacts proved challenging using the muffle furnace. However a reputable and reliable melting, casting and sintering cycle was developed which is presented by temperature-time graph given in **Figure 9**.

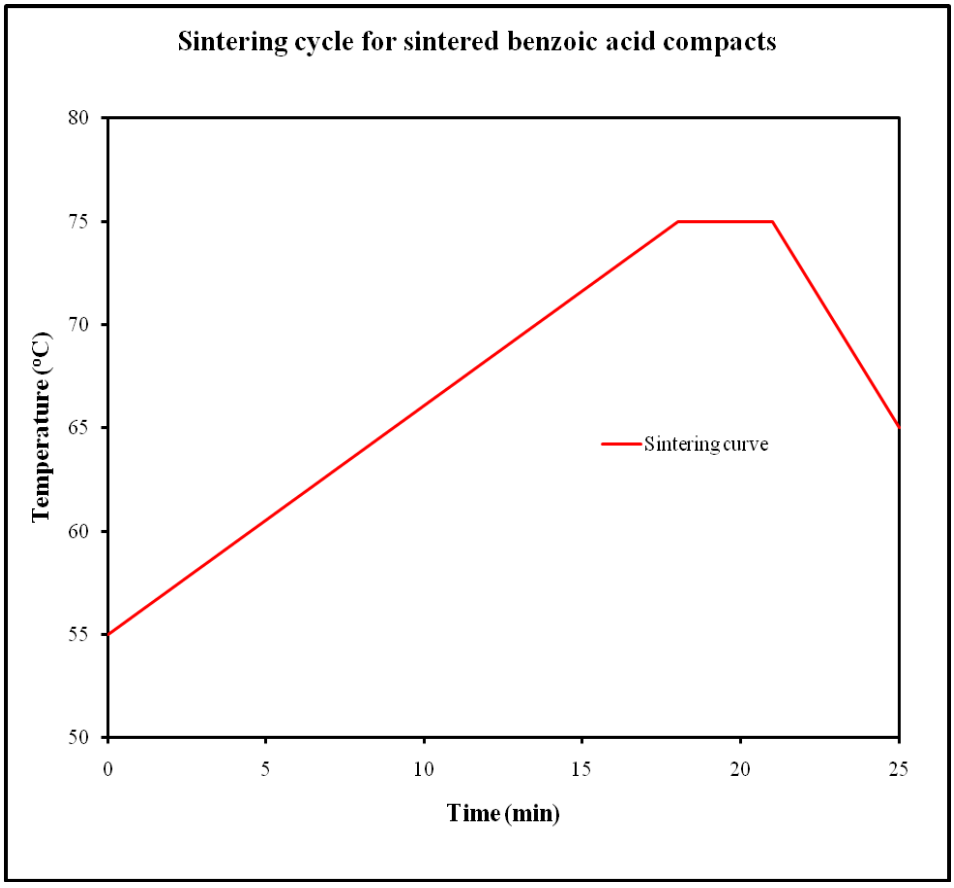

Figure 9: Temperature-Time graph for benzoic acid sintered compacts production

Using the temperature-time graph in **Figure 9**, sintered benzoic acid compacts were produced as shown in **Appendix A8** with the average outside dimensions as specified. This process involved preheating the muffle furnace to 55^{o}C, charging steel moulds with benzoic acid flake inside with an aluminum foil outside and increasing the temperature at a rate of 1.05^{o}C/min to 75^{o}C. A holding time of 3mins at this temperature was allowed before furnace

cooling and discharging the cast at +/- 65^{o}C. After successfully casting benzoic acid compacts, they were mounted to a steel grid fastened with threaded rod as shown in **Appendix A8** (bottom-left picture). After that, a total of 8 samples were spatially located in the converter model at predetermined depth for every experimental run. The samples were introduced and immersed into the water bath after the required air volumetric flow rate has reached a steady state value within +/-1% of the required value and the simulated slag thickness has been added. The samples were enclosed between two 1mm thin mild steel washers on both ends in order to promote radial dissolution only.

Spatial locations in the converter model of the samples as considered in this study are shown in **Figure 10**. Due to shallow simulated matte and simulated matte depth relative to the sample lengths, two sample depths were considered in these experiments. The first depth was defined as depth when the foot of the sample is 50mm from the bottom of the converter and shall be termed H_{50}.

The second depth was defined as the depth when the foot of the sample is 90mm from the simulated matte-simulated slag interface and shall be termed H_{90}. Each sample in the spatial location is appended with sample number and position as shall be referred to in the subsequent chapter (Results and Discussion).

3.1.3.3.1 Measuring experimental spatial arrangement

After treatment of the samples in the water bath for 900 seconds, the samples were withdrawn, furnace dried at 30^{o}C and eventually air cooled and weighed before getting them back into the converter and the procedure being repeated four times giving a maximum of 3600 seconds treatment time. Each experimental condition was repeated twice and weight was taken as the average of the runs which were all had reproducibility within 3% standard deviation.

Due to the unevenness of the samples after treatment, direct measurement of radii was precluded and not feasible. Instead, the weight loss measurements were used to obtain the equivalent radii as shall be discussed in the subsequent section. Due to chemical interaction of the kerosene, benzoic acid and water, highly flammable vapors were produced.

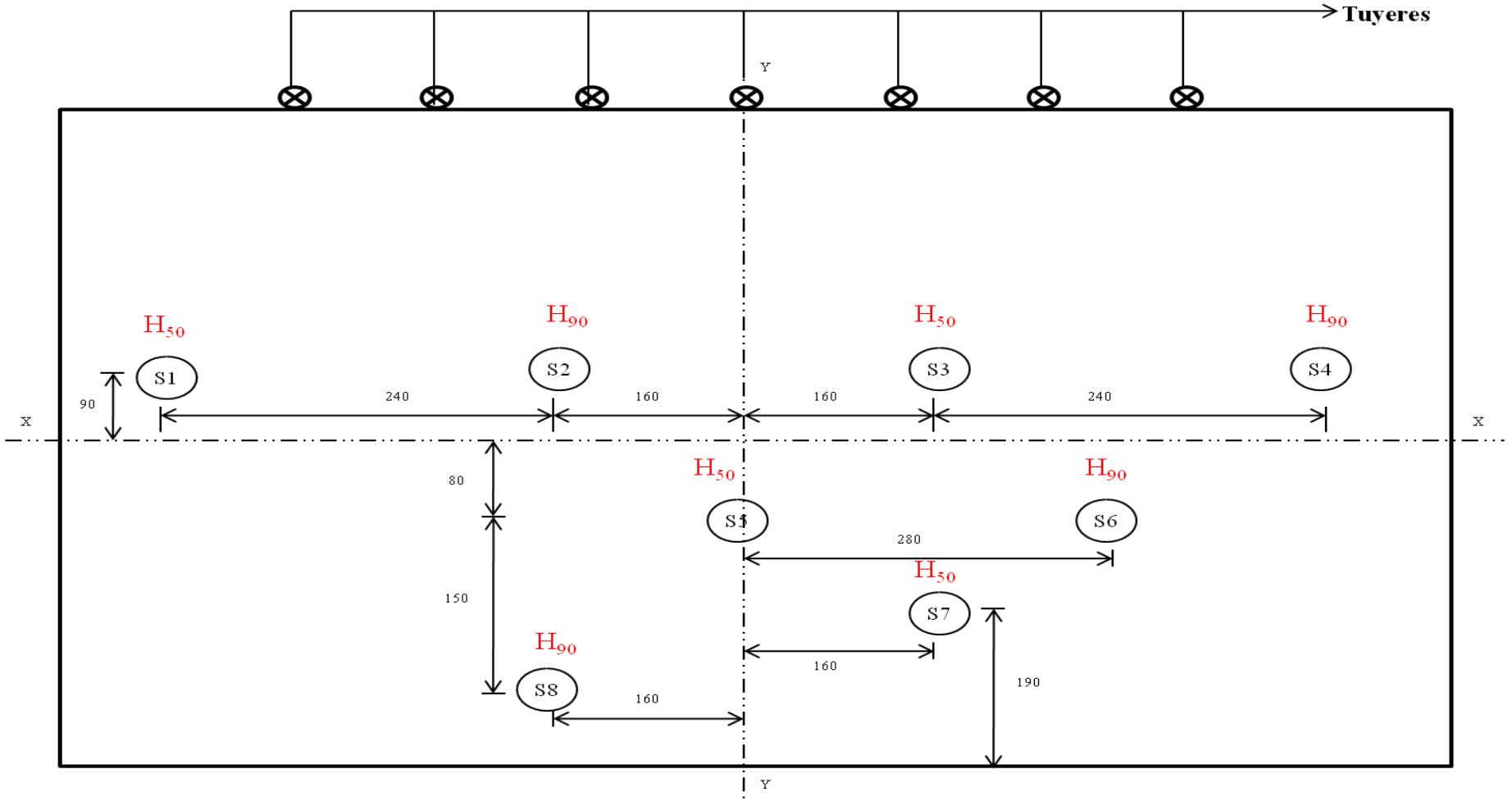

Figure 10: Schematic aerial view of the samples spatial locations in the converter model

Exposure of carbide heating elements in the muffle furnace used in this work would result in ignition. To alleviate this problem, drying temperature was kept between 30^{o}C and 40^{o}C. This temperature range was found sufficient for drying the samples. The influence of drying conditions on weight loss measurement was considered negligible.

3.1.3.3.2 Mass transfer coefficient estimation

Benzoic acid sintered compacts produced for this work were relatively insoluble in water and as such effects of natural convection are minimal and negligible. The mass transfer mechanism assumed in this study was due to steady streaming flow induced by the recirculation of simulated matte in the converter over the benzoic acid sintered compacts. According to Arters & Fan (1986), the driving force for interfacial mass transfer on the effective liquid film which surrounds a solid particle is the difference between the saturated solute concentration at the particle surface and the concentration in the bulk liquid.

Mathematical model expression of the statement is applied to the current study as:

$$\frac{dm}{dt} = KA(C - C_{sat}) \qquad \textbf{Equation 48}$$

In this equation; C is the dissolved concentration of the solute in the bulk liquid.

C_{sat} is the concentration of the solute in the boundary layer.

A is the total interfacial area.

K is the mass transfer coefficient.

m is the mass of the benzoic acid sintered compacts.

Considering that $m = \rho_s \pi r^2 L$ and $A = 2\pi rL$, where L (mm) is the sample length and r (mm) is the sample radius, mass transfer coefficient K (ms^{-1}) may be estimated from **eq. (49)**.

$$K = \left(\frac{dr}{dt}\right) \cdot \frac{\rho_s}{C_{sat}} \qquad \textbf{Equation 49}$$

Where ρ_s (kgm^{-3}) is the sample density. The assumption made in the derivation of the equation is that the concentration of the liquid surrounding the sample surface is equal to the

saturation concentration of the bulk liquid. The $\left(\frac{dr}{dt}\right)$ values were found by converting instantaneous weight loss of the sample with time and the expression used is:

$$\left(r_i^2 - r_f^2\right) = \frac{\Delta m}{\rho_s \pi L} \qquad \textbf{Equation 50}$$

In this equation; r_i is the sample initial radius.

r_f is the equivalent final sample radius.

Δm is the weight loss.

L is the sample length.

3.1.3.3.3 Turbulence parameter values estimation

As discussed in **section 2.6.2**, Sherwood number related exponential relationships characterizing turbulence in various systems under various conditions have been developed. The correlations are specific to the experimental condition and as such are not generally applicable. Singh & Mazumdar (1997) using purely experimental technique employing observations of dissolution rates of solid benzoic acid compacts in aqueous gas bubble driven system, assessed the adequacy and appropriateness of the various Sherwood number based correlations. This work conclusively recommended that the correlation by Mazumdar et al. (1990) given below is preferred to provide reasonable estimates of solid-liquid mass transfer rates in gas bubble systems.

$$T_i = \left(\mathrm{Re}_{loc,r}\right)^{0.25}\left(\mathrm{Re}_t\right)^{0.32} = \frac{Sh}{0.73\left(Sc\right)^{0.33}} \qquad \textbf{Equation 51}$$

This was due to the observed measured and predicted distribution of flow parameters and various dimensionless groups notably, $\left(\mathrm{Re}_{loc,r}\right)$, $\left(\mathrm{Re}_t\right)$ and $\left(Sc\right)$ with the application of this equation. Therefore, **eq. (51)** will be used to characterize the turbulence effect as it effectively resolves fluctuating components of integral flow quantities of velocity and turbulence as applicable to the current study. As such, the turbulence characteristic values will be calculated from **eq. (51)**.

In this equation, the middle portion of the equation has been considered as the turbulence characteristic in this study as the right hand side of the equation contains dimensionless

groups which contain kinematic viscosity, molecular diffusivity and geometrical effects of the model.

3.2 Numerical Simulation and Model Development

The Peirce-Smith converter experimental model was developed in stages through identification and formulation of the flow problem in terms of the physical and chemical phenomena. The aim is simply to produce mixing times at selected simulation conditions to verify physical experimental results as well as calculation of integral flow quantities to explain both mixing and mass transfer results. In the subsequent sections, the reasoning behind the model development will be discussed simultaneously with the details of the solution domain and model specifications considered in this study.

3.2.1 Solution Domain Creation

The first step in building and analyzing the flow model was done using the pre-processing commercial package accompanying Fluent called Geometry and Mesh Building Intelligent Toolkit (Gambit) in creation of the geometry, application of suitable computational mesh, assigning flow boundary conditions specification and fluid materials properties used. Gambit 2.4.6 was used in this study. In order to obtain system replication between the numerical and physical model, dimensions and boundary conditions as applied to the physical model were used for the development of numerical model.

3.2.2 Geometry

A one-fifth water bath scale model of the PSC was developed as shown in **Figure 11 and Figure 12**, which shows the 2-D and 3-D domain of the geometry respectively. The 3-D geometry was the full scale development with seven circular tuyeres on one side of the cylindrical vessel.

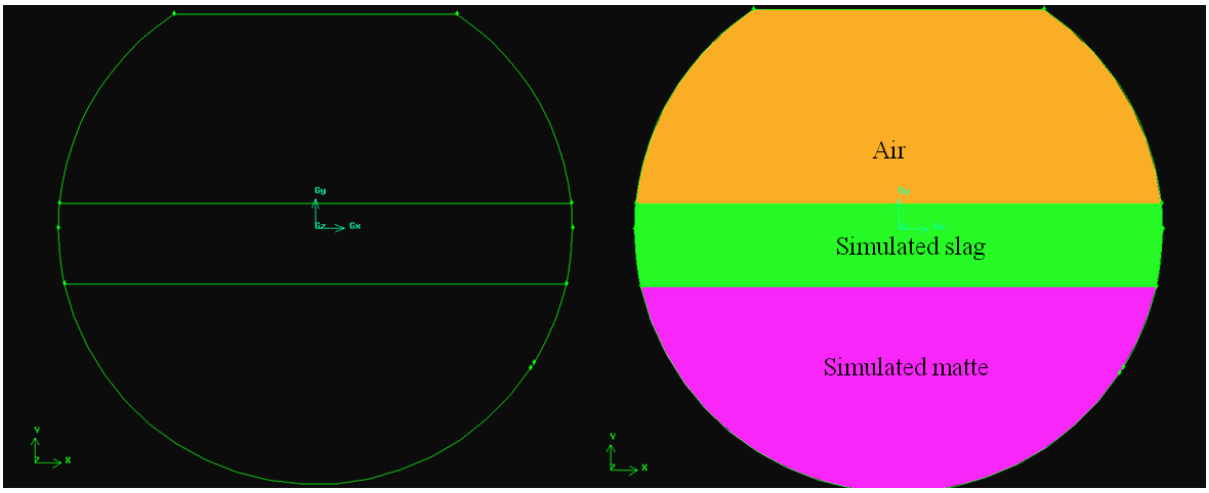

Figure 11: Gambit sketch of the 2-D drawing of the Peirce-Smith converter model

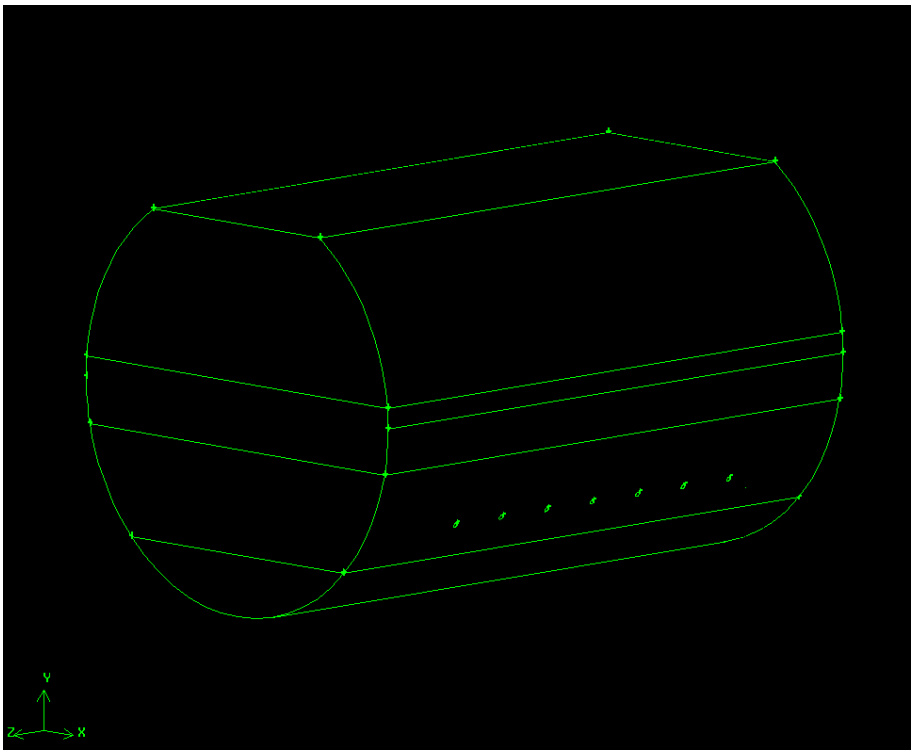

Figure 12: Gambit sketch of the 3-D drawing of the Peirce-Smith converter model

The simulated slag thickness was varied in five levels (0, 27, 54, 81 and 108mm) and as such, 10 geometries were created with various simulated slag thickness. In all simulations, simulated matte height was kept constant at 270mm. The development of the 2-D was done to test the applicability and feasibility of the boundary conditions, mesh generation and solution set up procedure. The solutions obtained in the 2-D simulations were two dimensional and

could not reveal all the information of the three dimensionality of the PSC which resulted in the development of the 3-D geometry.

Figure 13 shows the half sections of 3-D domain created in Gambit with the specified fluid zones considered in this study for the highest simulated slag thickness. The flow domain was meshed as detailed in the subsequent section.

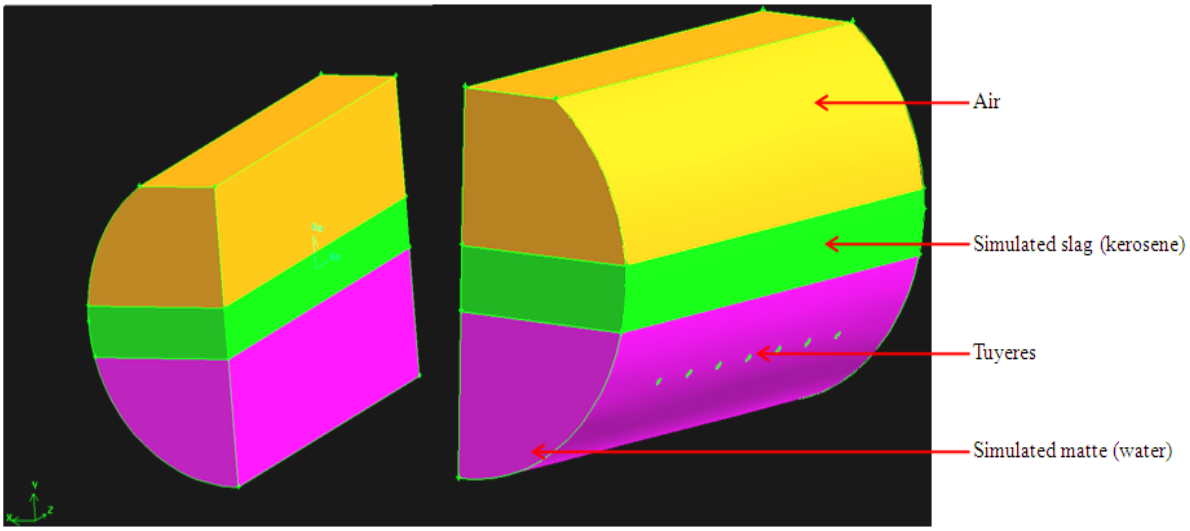

Figure 13: The different continuum zones specified with material type

3.2.3 Meshing the computational domain

The subdivision of computational domain given in **Figure 13** into a discrete number of smaller and non-overlapping finite control volumes or computational cells (mesh) was performed with the endeavor to produce most favorable mesh to better the solution precision. In the creation of the mesh, application was made of the size function capability of the **Gambit 2.4.6** package in order to produce finer mesh in areas of high solution gradients, with the coarser mesh being implemented in regions with relatively small solution gradients.

A structured grid, consisting essentially of hexahedral mesh elements was used because of its superiority on producing more accurate solutions, greater possibility of flow alignment with the grid coupled with the ability to be anisotropically subdivided without elements quality deterioration as discussed in **section 2.4.2.4.1**. Unstructured grid tetrahedral mesh elements were avoided as they are susceptible to numerical diffusion and higher storage capacity. In order to have hexahedral mesh elements on the entire flow domain, the cooper tool method was used on all created volumes. Due to the tuyere inlets which were developed as faces on the circular face of the volume containing simulated matte continuum, the volume was

divided into two connected volumes in order to create mappable faces to serve as source faces for coopering.

Main features of the flow domain are namely; the simulated matte-simulated slag interface, simulated slag-air interface and high velocity plume regions. The high velocity plume regions elongate from the tuyere exit to the bath surface which needs to be adequately resolved with finer grid resolution, adequate enough to capture the phase emulsification and bubble formation at the tuyere exit and the entire flow domain. Size functions were applied to the three geometrical faces of interest where there is need of improved solution accuracy.

The mesh was growing into the entire flow domain with a maximum size of 20mm which was found to be the optimal mesh size after grid solution sensitivity analysis. The cooper tool was applied for the generation of hexahedral mesh cells. The size function was followed as the mesh spacing specifications during meshing of any specified volume.

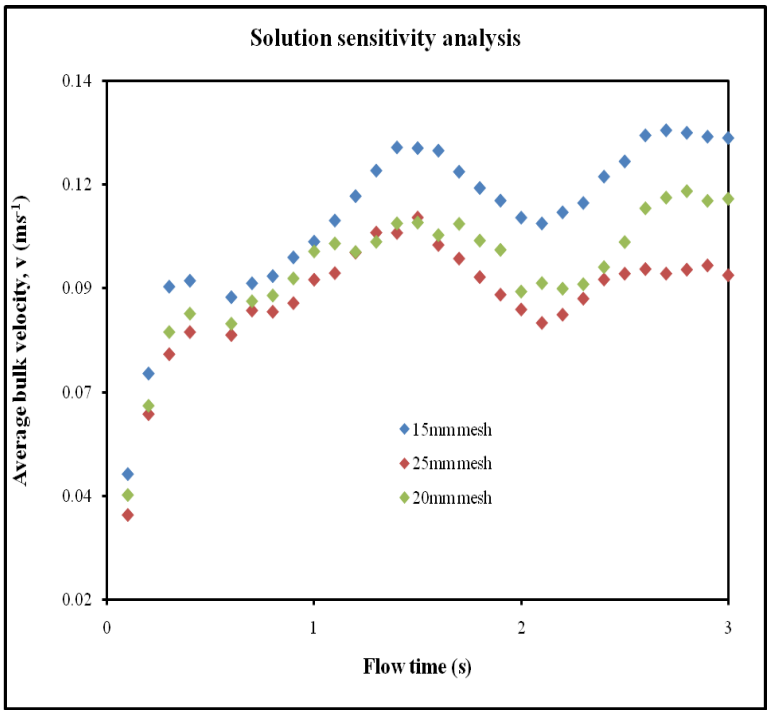

Figure 14: Grid solution sensitivity analysis

Figure 14 shows mesh dependence sensitivity analysis results. The data points at specific sampling points for the three mesh sizes were considered. The average standard deviation of all the points was within 0.95%. A maximum of 20mm mesh size was thus used in this study with one grid adaptation in the tuyere line region. Refinement was done in this region until it

was found that there is no flow variables variation in this region, thus grid independence achievement.

3.2.4 Mesh quality

The mesh quality can have a considerable impact on the computational analysis in terms of the quality of the solution and the time needed to achieve it. This aspect becomes especially important in case of inadequately conditioned problems, non-linear, and/or transient analyses are considered. From this point of view, the evaluation and assessment of the quality of the mesh is very useful because it provides some indication of how suitable a particular discretization is for the analysis type under consideration.

There are several ways on how to compute the quality of individual elements and how to quantify the overall quality of a mesh. Full documentation is provided in ANSYS (2008). In the present work, the computational cell skewness which is defined as the measured difference between the shape of the cell and the shape of an equilateral cell of equivalent area (for 2-D domain) or volume (for 3-D domain) was used as the mesh quality measurement criteria. Highly skewed computational cells can decrease accuracy and stability of the solution. Equisize skewness M_{eqs} is defined as follows:

$$M_{eqs} = \frac{\left(S_{eq} - S\right)}{S_{eq}} \qquad \textbf{Equation 52}$$

In this equation, S and S_{eq} are the area (2-D) or volume (3-D) of the computational mesh element and the maximum area (2-D) or volume (3-D) of an equilateral element with the circumscribe radius which is identical to that of the computational mesh element respectively. For the 2-D and 3-D computational domain used in this study, computational cells (mesh) had greater 92% of elements with an Equisize skew of 0.4 which translates to high quality mesh.

Figure 15 shows mesh quality distribution for the 2-D and 3-D domain used for the case with simulated slag thickness of 54mm. This figure shows 99.97% and 98.86% elements with less than 0.4 Equisize skew respectively. This translates to high mesh quality (ANSYS 2008), which is a requirement for accurate and converged solution.

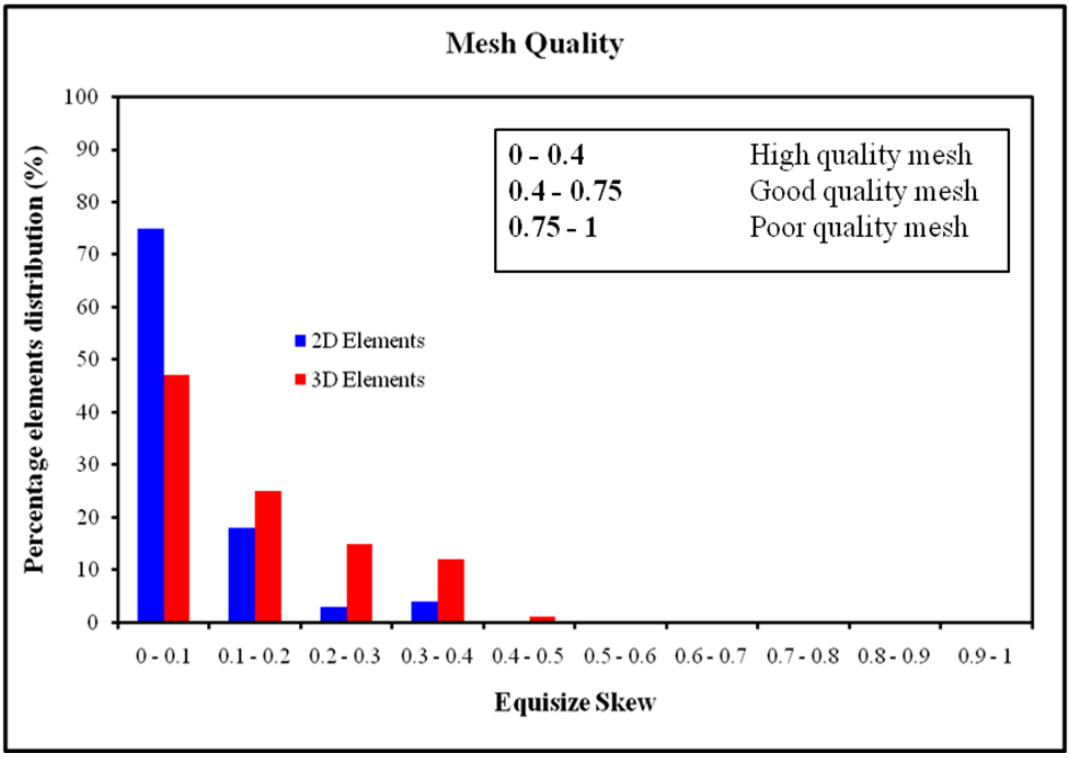

Figure 15: Computational domain mesh quality distribution for 2-D and 3-D elements

3.2.5 Boundary conditions and zones

Numerical simulations consider the physical nature of the physical process and as such assignment of boundary conditions is very important. This is achieved through assigning materials to components and mathematical formations in the simulation domain. In this study, models of mathematical formulations to resolve the physics of flow in space and time were employed.

3.2.6 Flow field models

In this work, three models of flow were implemented to account for the multiphase, turbulent nature of the converter operation and mass transport for the traversing of tracer in the converter.

3.2.6.1 Volume of Fluid Model (VOF)

Volume of fluid model was used for tracking and locating the free surface and fluid-fluid interface. As mentioned in **section 2.4.2.3.1** the model belongs to the class of Eulerian methods which are characterized by a computational cell that is either stationary or moving in a certain prescribed manner to accommodate the evolving shape of the interface. The VOF

method is known for its ability to conserve the "mass" of the traced fluid. When fluid interface changes its topology, this change is traced easily, so the interfaces can for example unite, or rupture away from each other.

3.2.6.2 Realizable $k-\varepsilon$ (RKE) turbulence model

There are numerous engineering turbulence models as discussed in **section 2.4.2.3.3** ranging from simple algebraic models to second-moment closure models. The group of two-equation turbulence models seems to be the most widely used (Salas et al. 1999).

With so many choices of turbulence models with varying sophistication and associated computational effort, one big challenge is the order of magnitude analysis of results offered by the variety of options available. In this work, the RKE model was used due to superior performance for flows involving rotation, boundary layers under strong adverse pressure gradients, separation and recirculation (Shih et al. 1995).

3.2.6.3 Species transport

The species model equation as discussed in **section 2.4.2.2.4** was employed to track the spread and dispersion of a tracer through the domain for determining the mixing time hence mixing efficiency of the process. The material for species was 98% sulphuric acid (H_2SO_4) with the properties as tabled in **Table 7**.

Spherical region adaptation in the model geometry was done at the coordinates same with the tracer injection point in the physical modelling experiments. Point surface creation was also done in the computational domain to specify the measuring point of the mass fraction distribution of the liquid species in the predefined transport medium. Tracer specified physical data such as diffusion coefficient, density and molar weight were used to recalculate effective transport coefficients using the distribution of the species concentration in space and time.

Material	Value	Reference
Simulated matte		
Density, kgm^{-3}	998	(ANSYS 2008)
Viscosity, Pas	0.0105	(ANSYS 2008)
Molecular weight, kg/kgmol	18.02	(ANSYS 2008)
Surface tension, Nm^{-1}	0.0728	(The Engineering ToolBox)
Simulated slag		
Density, kgm^{-3}	774	(Shell 2006)
Viscosity, Pas	0.00242	(Cameo Chemicals 1999)
Molecular weight, kg/kgmol	167	(ANSYS 2008)
Surface tension, Nm^{-1}	0.0275	(Cameo Chemicals 1999)
Simulated matte - simulated slag interfacial tension	0.048	(Johansen 1924)
98% Sulphuric acid		
Density, kgm^{-3}	1840	(Sullivan 2008)
Viscosity, Pas	0.0267	(Sulphuric acid)
Molecular weight, kg/kgmol	98.08	(Sulphuric acid)
Surface tension, Nm^{-1}	-	
Air		
Density, kgm^{-3}	1.205	(Density of air)
Viscosity, Pas	0.0000179	(ANSYS 2008)
Molecular weight, kg/kgmol	28.97	(ANSYS 2008)
Surface tension, Nm^{-1}	-	

Table 7: Physical properties of the fluids used in the model

3.2.7 Materials properties

Multiphase nature of this model considered three materials namely simulated matte, simulated slag and compressed air with their physical and chemical interactions for the integral fluid flow quantities simulations. However for the purposes of mixing time measurement numerical simulations, concentrated 98% sulphuric acid was included. **Table 7** shows the physical properties of the materials used in the model. The interfacial surface tension between simulated matte and simulated slag was accounted for with the assumption that the two fluids are insoluble in each other and are immiscible with no water soluble substances absorbable at the interface.

3.2.8 Boundary conditions

The precision of boundary conditions on the solution domain contributes to accuracy of the solutions. They consist of flow inlets and exit boundaries which have to be specified with their scalar properties of the flow such as turbulence parameters, velocity and pressure. Walls and internal faces are also boundary conditions that need specification. Wall treatment, air inlet volumetric flow rates and outlet boundary conditions employed in this work will be discussed in the subsequent sections.

3.2.8.1 Air inlet boundary condition

Velocity inlet boundary condition was used for the specification of flow conditions into the model at the tuyere inlets. With this boundary condition, the total (or stagnation) pressure is not fixed but will rise in response to the computed static pressure to whatever value is necessary to provide the prescribed spatial velocity distribution. Through calculation of the total cross sectional area, A of the air flow inlet surfaces and using the total line air volumetric flow rate, Q the tuyere inlet velocity, v_t was calculated from **eq. (43)**.

Air volumetric flow inlet turbulence specification method was implemented and calculation of the turbulence intensity, I and hydraulic diameter, D_H was done. The turbulence intensity, I is defined as the ratio of the root-mean-square of the velocity fluctuations, v' to the mean flow velocity, $\bar{v}$. Assuming fully developed flow at the tuyere exit, turbulence intensity was calculated as:

$$I \equiv \frac{v'}{\bar{v}} = 0.16\left(\mathrm{Re}_t\, D_H\right)^{-\frac{1}{8}} \qquad \textbf{Equation 53}$$

In this equation, Re_t is the tuyere exit Reynolds number.

The hydraulic diameter D_H (mm) is used to calculate the dimensionless Reynolds number to determine if a flow is turbulent or laminar. It is found by the ratio of cross sectional area and wetted perimeter as given in **eq. (54)**.

$$D_H = \frac{4A}{P_w} \qquad \textbf{Equation 54}$$

In this equation, P_w (mm) is the tuyere wetted perimeter. The air inlet specifications used in the numerical modelling are shown in **Table 8**.

Air flow rate, Q (Nm^3s^{-1})	**Tuyere inlet Velocity, v_t (ms^{-1})**	**Tuyere Reynolds Number, Re_t**	**Turbulent Intensity, I (%)**	**Hydraulic diameter, D_H (mm)**
0.00875	20.78	11532	8.98	8.75
0.01000	23.76	13185	8.84	8.75
0.01125	26.73	14833	8.70	8.75
0.01250	29.70	16482	8.59	8.75
0.01375	32.67	18130	8.49	8.75

Table 8: Summary of air velocity inlet specification

3.2.8.2 Outlet boundary condition

Pressure outlet boundary condition was used for the specification of flow conditions at the model open top. Static (gauge) pressure specification was included and is valid for subsonic flow regime as the current situation. The static pressure specified was relative to the operating pressure which in this study is set to atmospheric pressure. Outlet turbulence specification method was carried out, specifying turbulence intensity and hydraulic diameter as given by **eq. (53)** and **eq. (54)** respectively. The calculated values of 8.6% and 460 were

used for turbulence intensity and hydraulic diameter, calculated from **eq. (53)** and **eq. (54)** respectively.

3.2.8.3 Walls boundary condition

Wall boundary conditions are used to bound fluid and solid regions. Wall boundary conditions were specified to simplify the operational conditions. A boundary condition of frictionless stationary wall was imposed on the side walls of the cylinder to ensure that the wall does not have influence on the fluid flow. Frictionless condition indicates that the fluid sticks to the wall and moves with the same velocity as the wall (if the wall moves) with resultant shear stress equal to zero.

3.2.9 Monitoring solution convergence

Monitoring solution convergence and stability provides one of the major challenges in numerical simulations as there are a number of factors that limit and hinders attainment of convergence and stability. These are specified as large numbers of computational cells, overly conservative under-relaxation factors and complex flow physics. As such, there are no universal metrics for judging convergence. Residual monitoring is applied in most cases. However, residual definitions that are useful for one class of problem are sometimes misleading for other classes of problems.

Therefore, in this study, convergence was judged by simultaneous examination of residual levels and predefined area weighted averages of surface monitors. These are relevant integrated quantities of interest such as mean bulk flow velocity in simulated matte phase and/ or simulated slag phase and turbulence kinetic energy in simulated matte phase and/ or simulated slag phase.

CHAPTER 4

RESULTS AND DISCUSSION

4. INTRODUCTION

The physical and numerical modelling of the Peirce-Smith converter model considered in this work yielded a series of distinct results. These investigations were centered on the mixing time characterization and solid-liquid mass transfer phenomena in the converter as discussed in the preceding chapter. This chapter presents simultaneously the results and comprehensive discussion of experimental findings in this study. The effects of considered simulated slag thickness and air flow rate on mixing efficiency characteristics and mass transfer will be detailed in the subsequent sections.

4.1 Mixing Time Measurements

After identification of suitable method by using sulphuric acid, pH meter probe and suitable tracer injection point, a total of 125 experiments were conducted to investigate the mixing efficiency of the model. Mixing time as defined in **section 3.1.3.2** was measured for various simulated slag thickness and air flow rates. Total specific mixing power as given in **eq. (32)** was used to obtain the mixing efficiency in the experiments.

4.1.1 Effects of Simulated Slag on Mixing Efficiency

The measured mixing time against total specific mixing power caused by different air flow rates, at constant simulated slag thickness results are given in **Figure 16.** As seen from **Figure 16**, simulated slag presence has been observed to affect the mixing characteristics in the converter. Analysis of **Figure 16** shows a complex phase interaction phenomena. In **Figure 16**, there appears to be two different bands of mixing time distributions, one with no and/ or with thin simulated slag layer and the other one is with high simulated slag thickness.

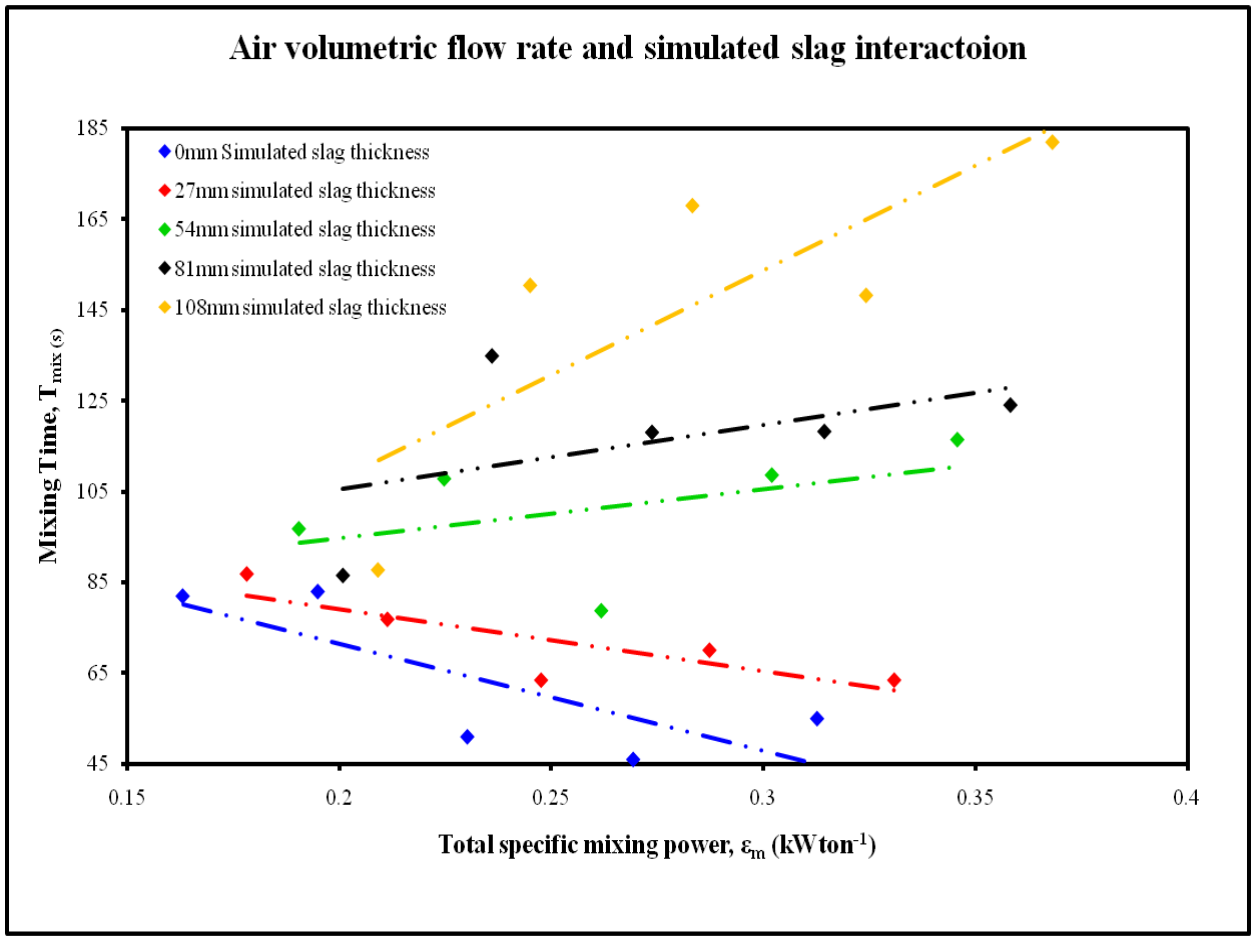

Figure 16: Effect of specific mixing power and simulated slag thickness on mixing time

Mixing time was observed to decrease with increase in total specific mixing power for the cases with no and with thin simulated slag thickness. With high simulated slag thickness of 54mm and above, this trend shifted to an increased mixing time with increase in total specific mixing power.

It is logical to assume that at no and thin simulated slag thickness, the effect of interphase interaction i.e. interphase friction, interphase diffusion, and two-phase turbulence modification in bath recirculation, is not yet fully developed (Schwarz 1996), hence the reduced mixing times observed. Numerical simulations have revealed that in thin simulated slag thicknesses, all slag is pushed ashore with the plume region being composed of almost only matte as shown in **Figure 17**. This increases hydrodynamic pressure to the rising bubbles and hence increased specific energy dissipated to the liquid phase for bath recirculation due to high bubble retention time thus increased mixing efficiency.

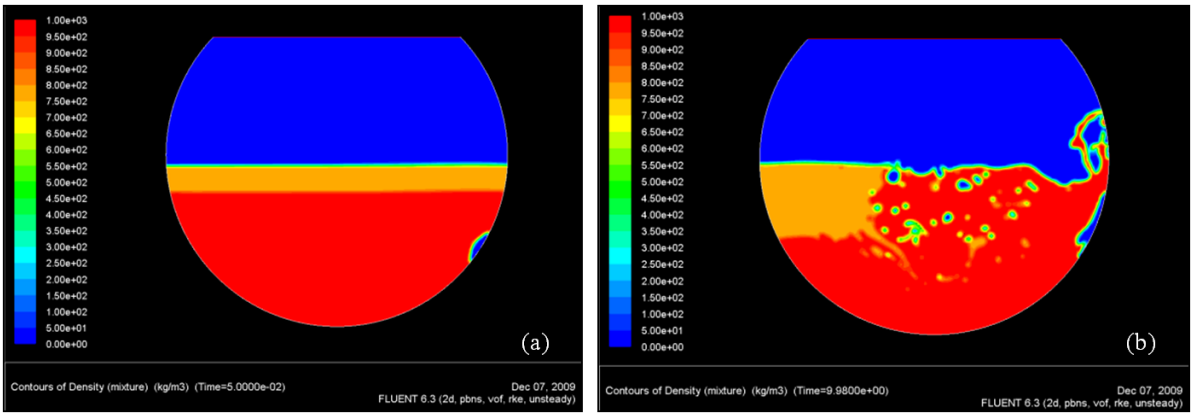

Figure 17: 2-D density contour plots with 54mm simulated slag thickness at 0.01125Nm^{3}s^{-1} (a) at 0.05 sec and (b) at 10 sec flow time

Also as a comparison, mixing time numerical simulations were also done with equivalent heights of only matte and matte plus simulated slag of which simulated slag was 108mm. Numerical simulations with only simulated matte depth show improved mixing efficiency. This could be attributed to improved gas bubble – bulk liquid momentum transfer due to high gas retention time hence increased mixing efficiencies.

Figure 18 show mixing time simulation results for 108mm simulated slag thickness case and equivalent total simulated matte depth which is 378mm.

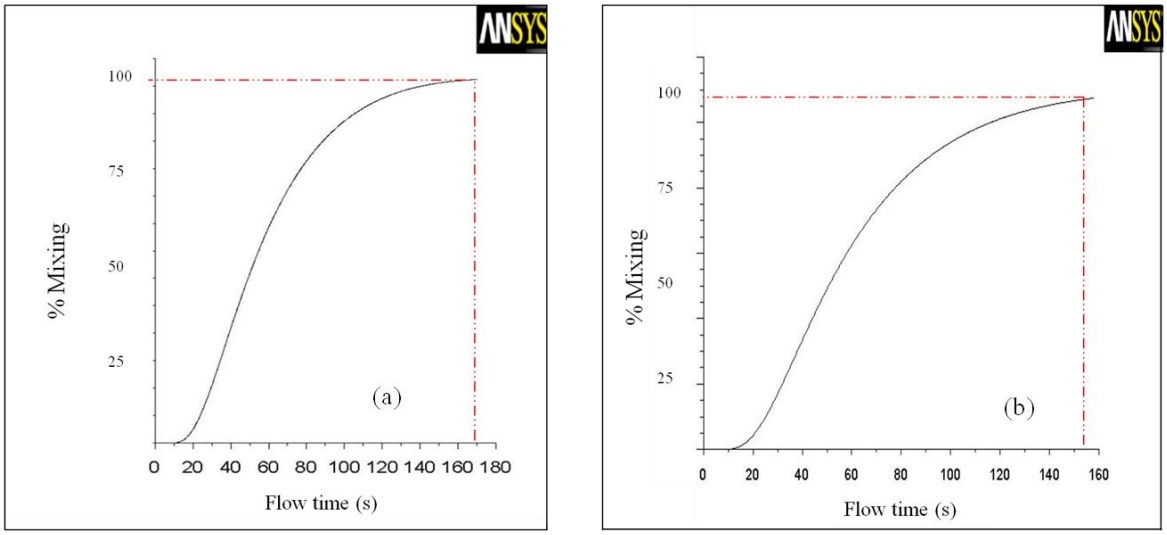

Figure 18: Numerical mixing time results for (a) 108mm simulated slag thickness case and (b) equivalent total simulated matte depth of 378mm at air volumetric flow rate of 0.01125Nm^{3}s^{-1}.

From **Figure 18**, mixing time decreased from 168s for 108mm simulated slag thickness to 153s for the equivalent simulated matte total depth showing that presence of simulated slag dissipates some useful energy. It is enlightening to note that the mixing time is higher for 27mm simulated slag thickness than the case with no simulated slag, indicating mild phase interaction effects, dissipating some useful bath induced energy of recirculation.

Therefore, the observed decrease in mixing efficiency at higher simulated slag thickness could be attributed to three-fold effect namely; channeling, manifestation of phase interaction between simulated matte and simulated slag and tuyere flow dynamics. Channeling and tuyere flow dynamics shall be discussed in the subsequent section in the effects of air volumetric flow on mixing efficiency discussion.

In **Figure 19** and **Figure 20**, numerical solution of flow at no simulated slag thickness and 108mm simulated slag thicknesses is shown.

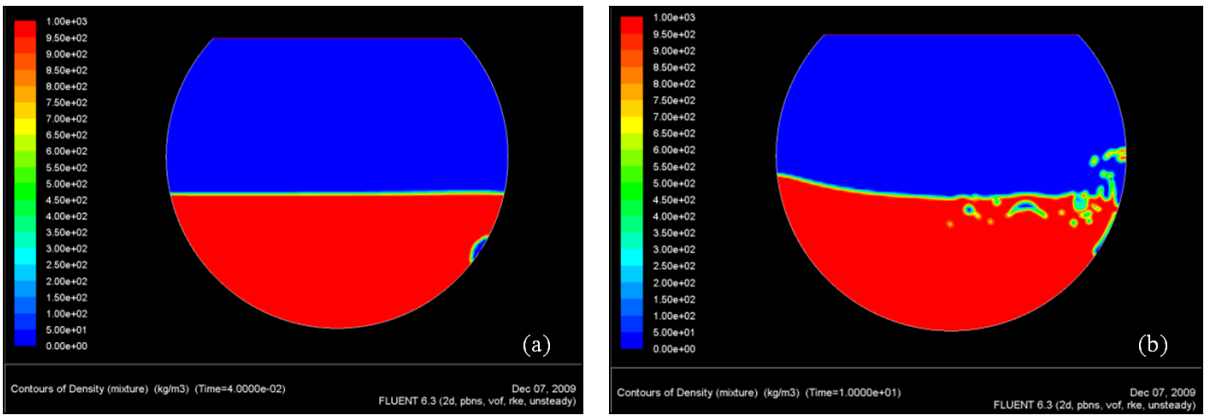

Figure 19: 2-D density contour plots with no simulated slag thickness at 0.01125Nm^3s^{-1} (a) at 0.05 sec and (b) at 10 sec flow time

Analysis of **Figure 19 (b)** shows that at no simulated slag thickness, all the power input to the system is distributed between the bulk flow recirculation and formation of splash in the plume region. With 54mm thickness of simulated slag, **Figure 17 (b)** shows dispersion of the simulated slag into simulated matte and also large splashes above tuyere line. Noticeably, the simulated slag phase is pushed ashore to the area opposite to air injection nozzles thereby forming a plume which is mainly composed of simulated matte. Such a scenario is beneficial as it increases the tuyere bubble trajectory path and retention time for energy transfer from the bubbles to the bulk liquid before they rupture at the bath surface as confirmed by the mixing times shown in **Figure 18**.

However, the benefits of such retention time are offset by the effects of phase interaction, friction and diffusion mechanism which dissipates substantial amount of energy. Also mechanisms of momentum transfer at simulated matte-simulated slag-air interfaces fritter away potential recirculation energy. At increased simulated slag thickness of 108mm, the effect of interaction and dispersion is highly pronounced as seen in **Figure 20 (b)**. As such, mixing efficiency is expected to decrease.

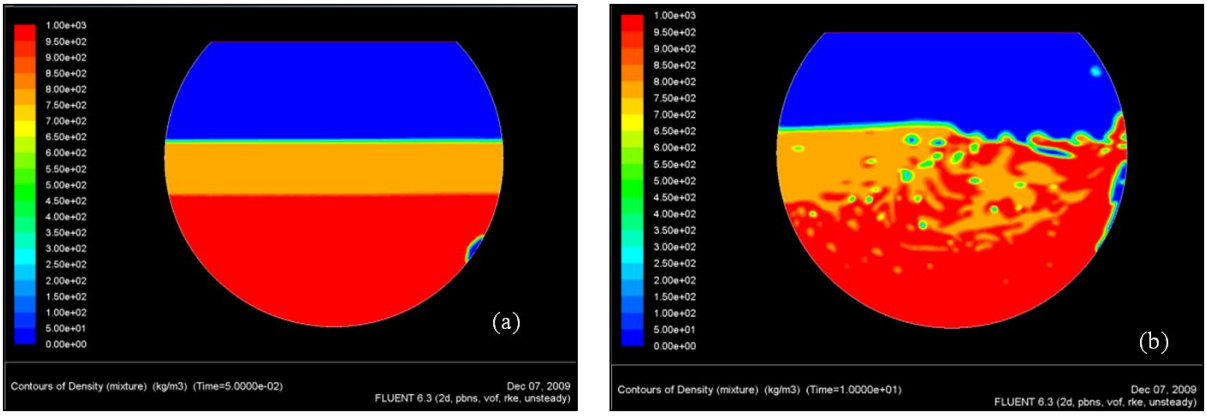

Figure 20: 2-D density contour plots with 108 simulated slag thickness at 0.01125Nm^{3}s^{-1} (a) at 0.05 sec and (b) at 10 sec flow time

Calculations of flow variables namely total bulk velocity and turbulence kinetic energy were carried out to see the effects of simulated slag thickness as a function of air volumetric flow rate on the dynamic state of the converter in space and time. The results of numerical simulations will be linked to physical simulation results through the calculation of these flow quantities and the physical quantitative observations,

Figure 21 shows how simulated matte recirculation velocity (average bulk velocity) and turbulence kinetic energy vary with simulated slag thickness at constant air flow rate of 0.00875Nm^{3}s^{-1}. It was observed that both values decrease with increase in simulated slag thickness. Reduction in recirculation velocity and turbulence with increased simulated slag thickness results in decreased mixing efficiency hence an increase in mixing times as observed in the measured physical experiments. The observed increase in mixing times at higher simulated thickness in **Figure 16** can be interpreted as a result of fully developed complex interphase interactions

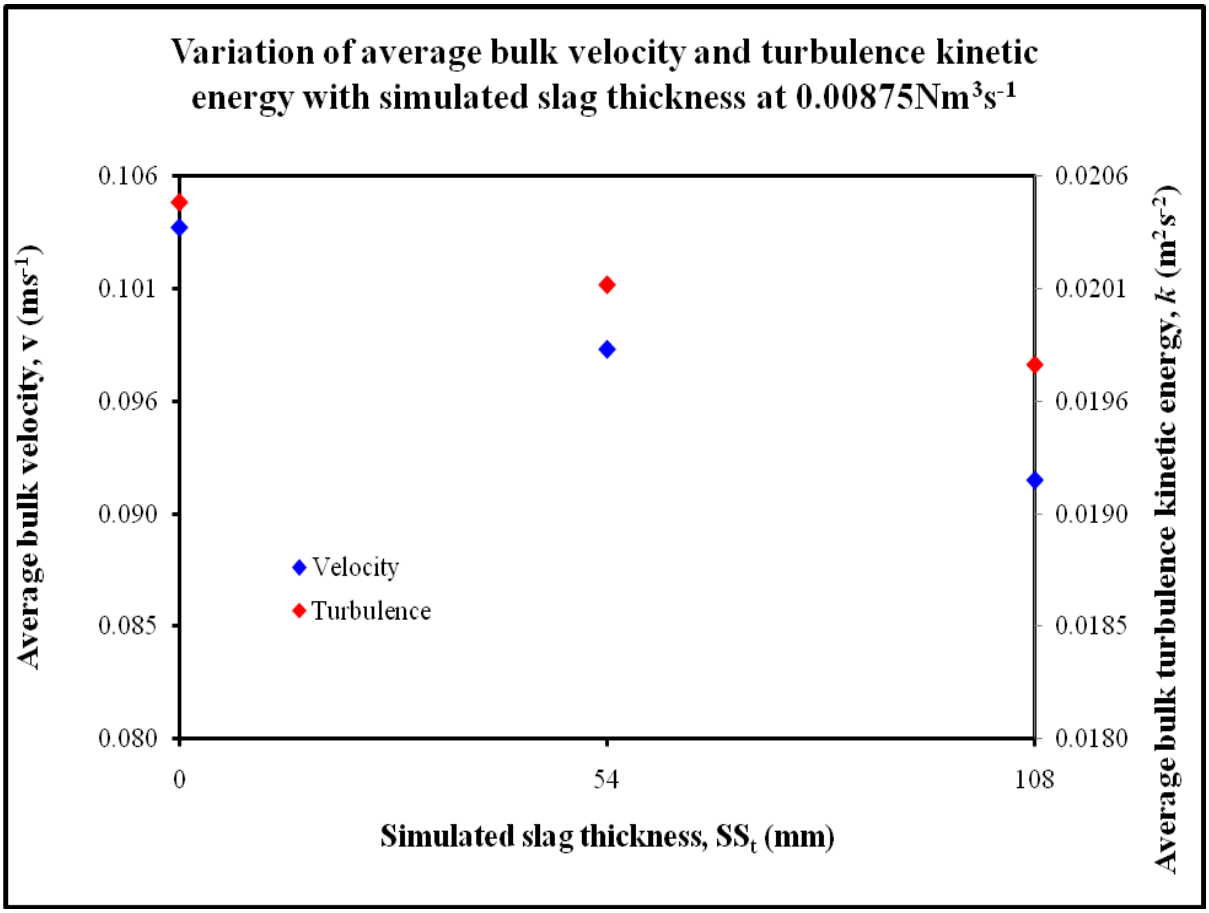

Figure 21: Variation of average simulated matte bulk flow velocity and turbulence kinetic energy as a function of simulated slag thickness at 0.00875Nm^3s^{-1}

Substantial amount of turbulence kinetic energy is dissipated in recirculation flows inside the simulated slag as shown by the velocity and turbulent vector plots in **Figure 22**, **Figure 23**, **Figure 24** and **Figure 25**. Analysis of **Figure 22**, **Figure 23**, **Figure 24** and **Figure 25** shows substantial amount of recirculation velocity and turbulence kinetic energy set up in the simulated slag layer relative to the velocity in the simulated matte. Kim & Fruehan (1987) observed in slag incorporated systems that such large distribution of velocity in multiphase metallurgical vessels cause decreased mixing efficiency. Relative amounts of velocity and turbulence are more pronounced in the 108mm simulated slag thickness than in the 54mm simulated slag thickness simulation shown in **Figure 22** and **Figure 24**.

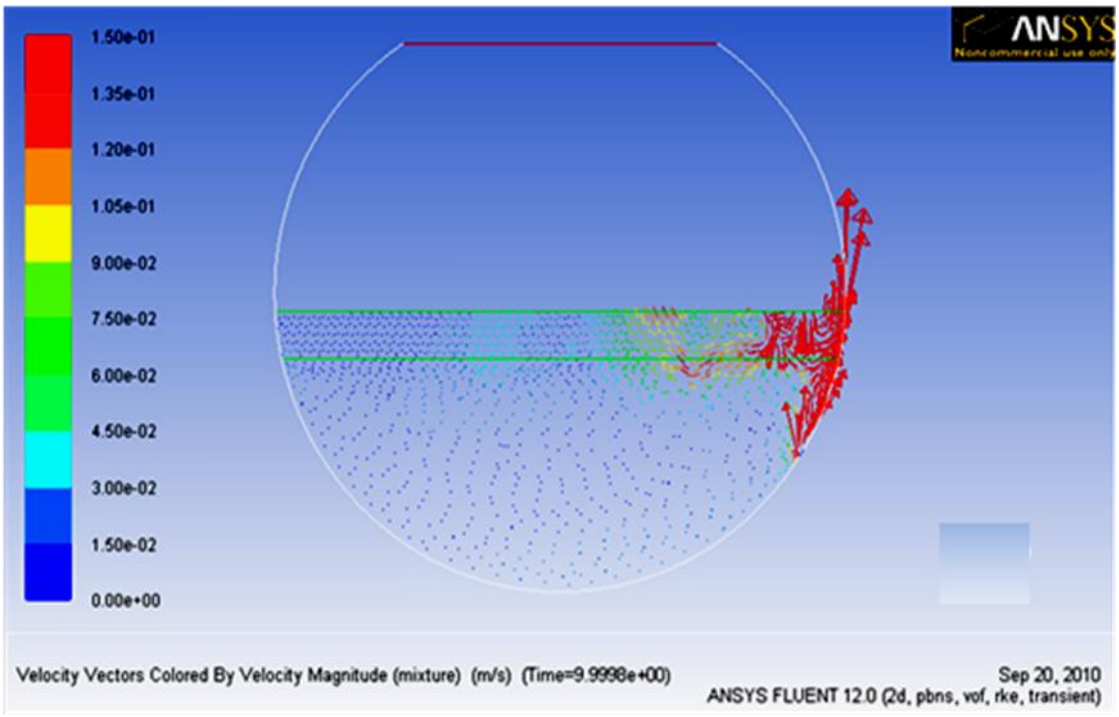

Figure 22: Velocity vector plots for 54mm simulated slag thickness at air flow rate of 0.01125Nm^3s^{-1}

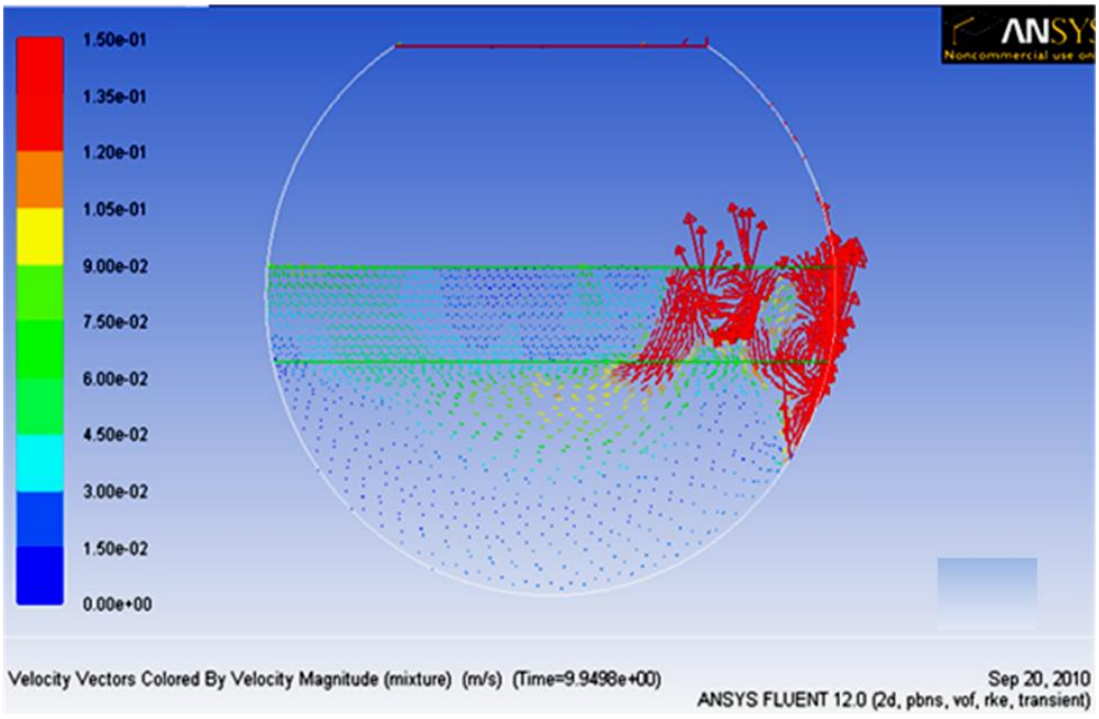

Figure 23: Velocity vector plots for 108mm simulated slag thickness at air flow rate of 0.01125Nm^3s^{-1}

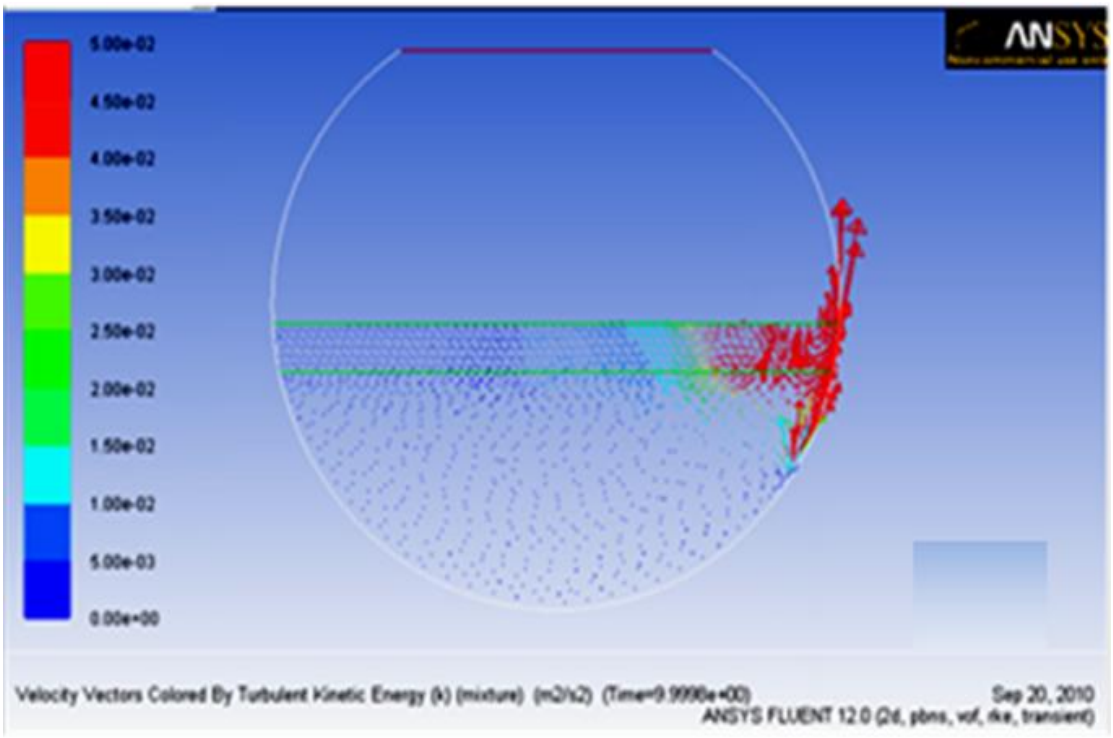

Figure 24: Turbulence kinetic energy vector plots for 54mm simulated slag thickness at air flow rate of 0.01125Nm^3s^{-1}

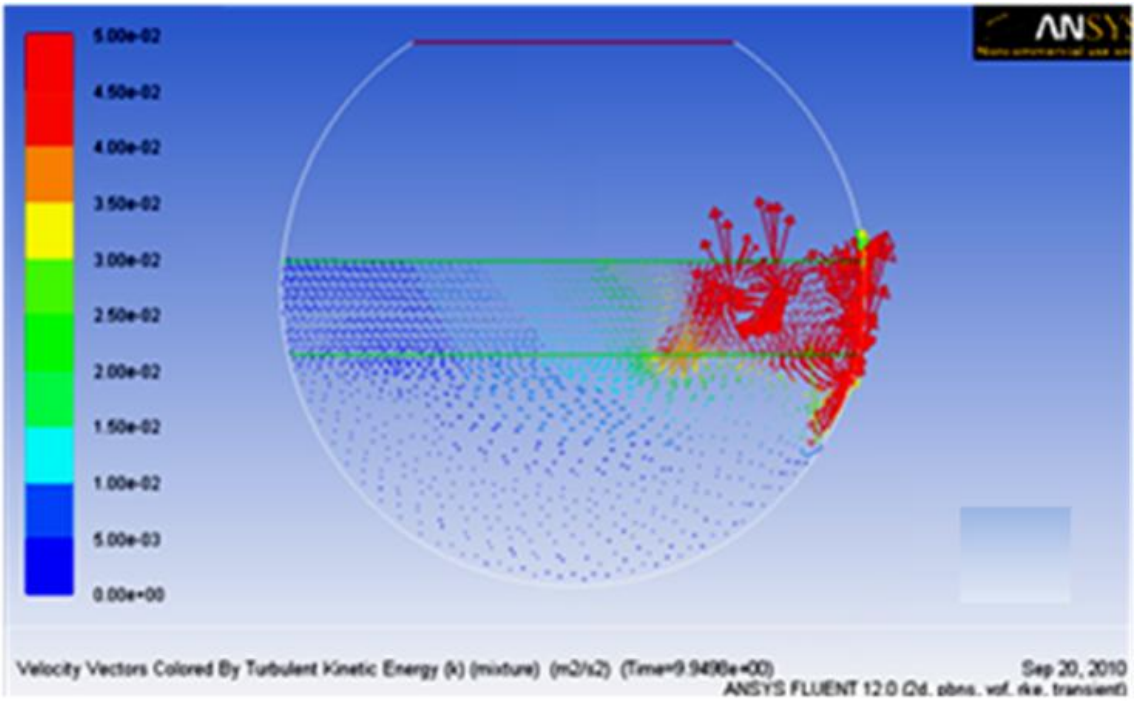

Figure 25: Turbulence kinetic energy vector plots for 108mm simulated slag thickness at air flow rate of 0.01125Nm^3s^{-1}

Numerical results of integrated flow quantities of bulk simulated matte velocity and turbulence kinetic energy at 0.01125Nm^{3}s^{-1} are presented in **Figure 26**. At this flow rate, which is equivalent to the real converter operational gas flow rate, an increase in simulated slag thickness resulted in decrease in bulk turbulence for all simulated slag layers.

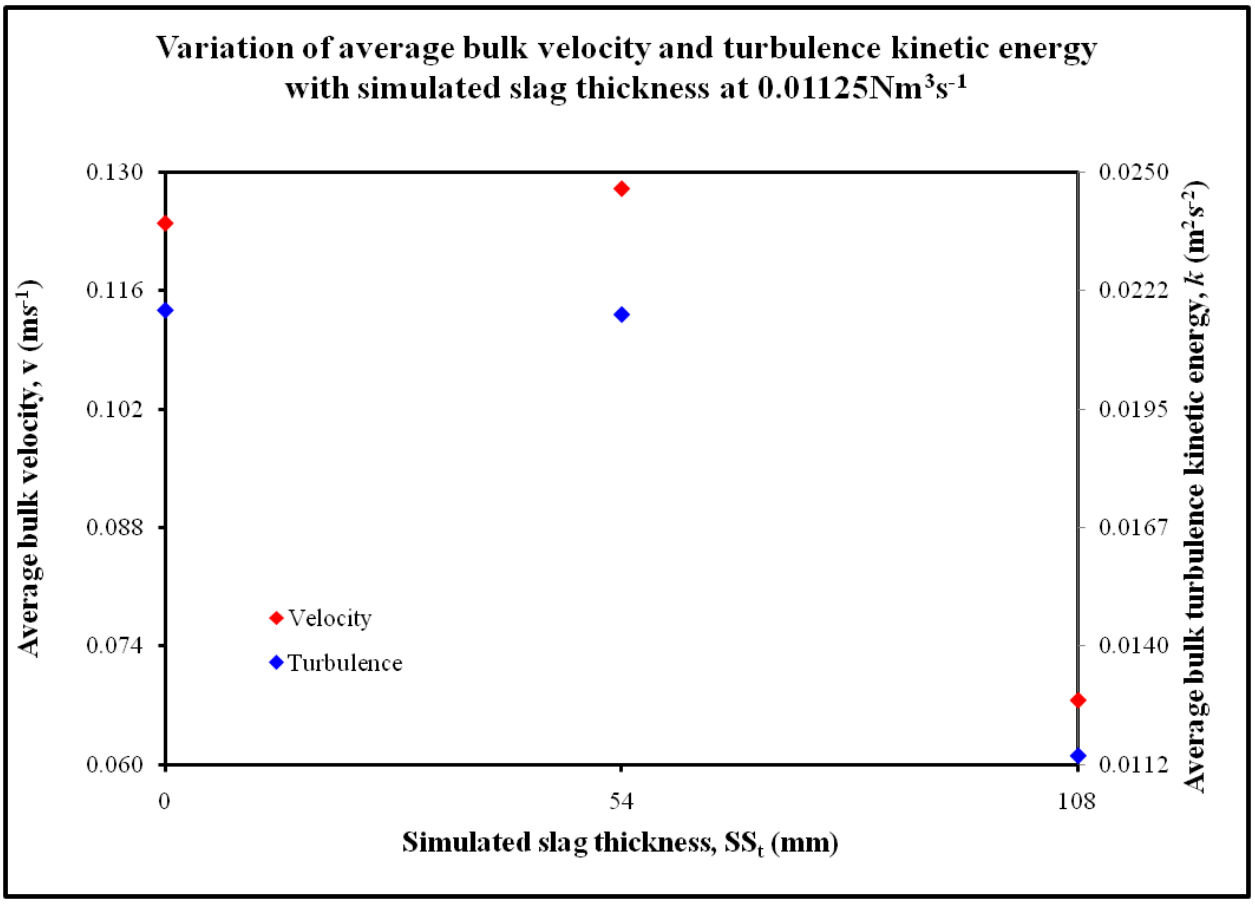

Figure 26: Variation of average simulated matte bulk flow velocity and turbulence kinetic energy as a function of simulated slag thickness at 0.01125Nm^{3}s^{-1}

However, there is a temporal bulk velocity increase from 0 to 54mm slag thickness which eventually drops drastically with a further increase in simulated slag thickness. This scenario presents a fact of trade off between utilization of power input and presence of thin slag layer compared to thick slag layers.

At shallow slag depths up to 54mm, the slag helps to create beneficial matte depth as it is pushed off the tuyere line as explained earlier. This occurrence increases retention and bubble trajectory path thus allowing sufficient momentum transfer as mentioned earlier. A numerical mixing time result for 81mm simulated slag thickness simulation and equivalent 351mm simulated matte depth simulations are given in **Figure 27**. This figure shows the benefits of

increased matte depth as mixing time has decreased with only simulated matte depth equivalent to summation of simulated matte and simulated slag depth.

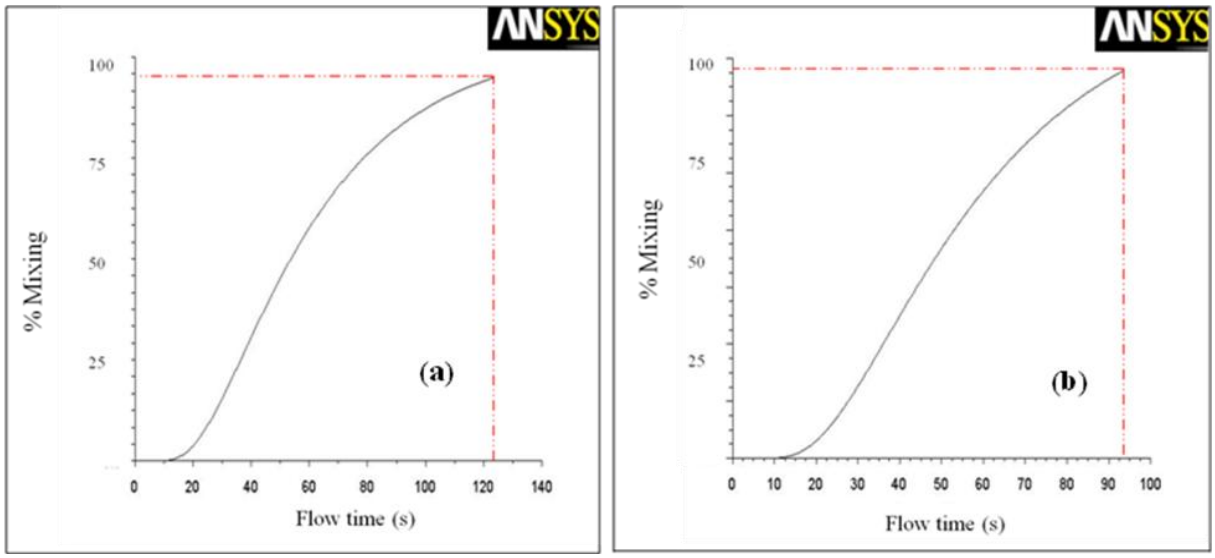

Figure 27: Numerical mixing time results for (a) 81mm simulated slag thickness case and (b) equivalent total simulated matte depth of 351mm at air flow rate of 0.01125Nm^{3}s^{-1}

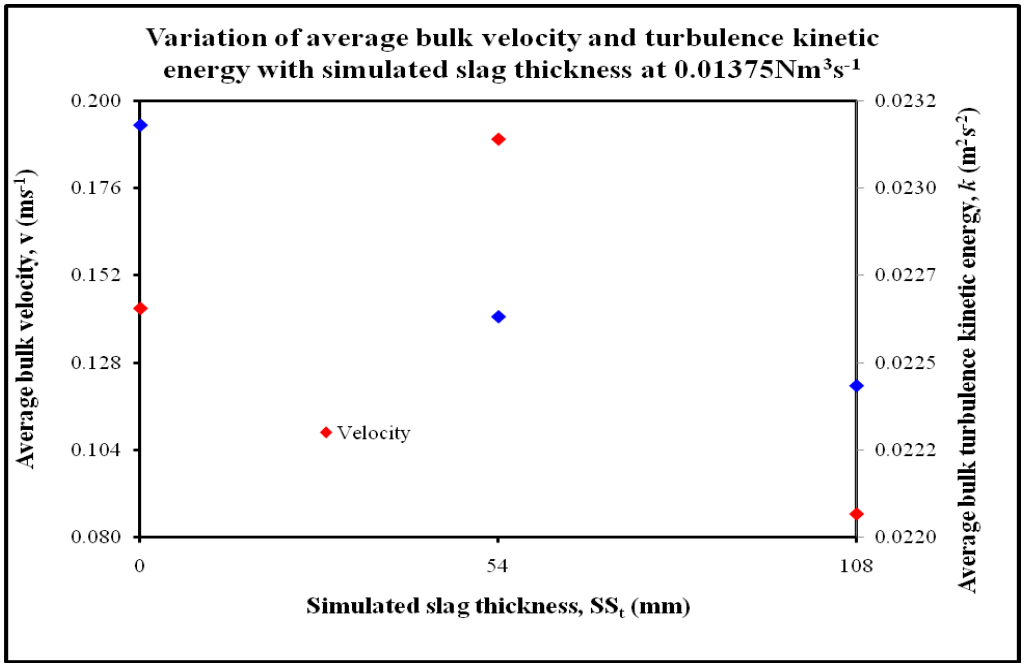

Figure 28: Variation of average simulated matte bulk flow velocity and turbulence kinetic energy as a function of simulated slag thickness at 0.01375Nm^{3}s^{-1}

At higher slag volumes the benefit of increased bubble retention is outweighed by phase interaction which detrimentally spent substantial amount of energy in the system and thus

reduced average bath velocity which results in decreased in mixing efficiency. The same scenario is observed for the simulated condition at 0.01375Nm^3s^{-1}, results which are given in **Figure 28**. It is valuable to note the point of inflexion on simulated slag thickness of 54mm which has shown to be the optimal slag volume acceptable for high mean bulk flow velocities required for high mixing efficiency.

4.1.2 Effects of Air Volumetric Flow Rate on Mixing Efficiency

Mixing efficiency in the converter has been found to be influenced by the amount of air injected as the air serves as the driving source of energy for recirculation flow. **Figure 29** shows an increase in mean bath velocity and turbulence kinetic energy with increased air volumetric flow rate when simulations were conducted without simulated slag.

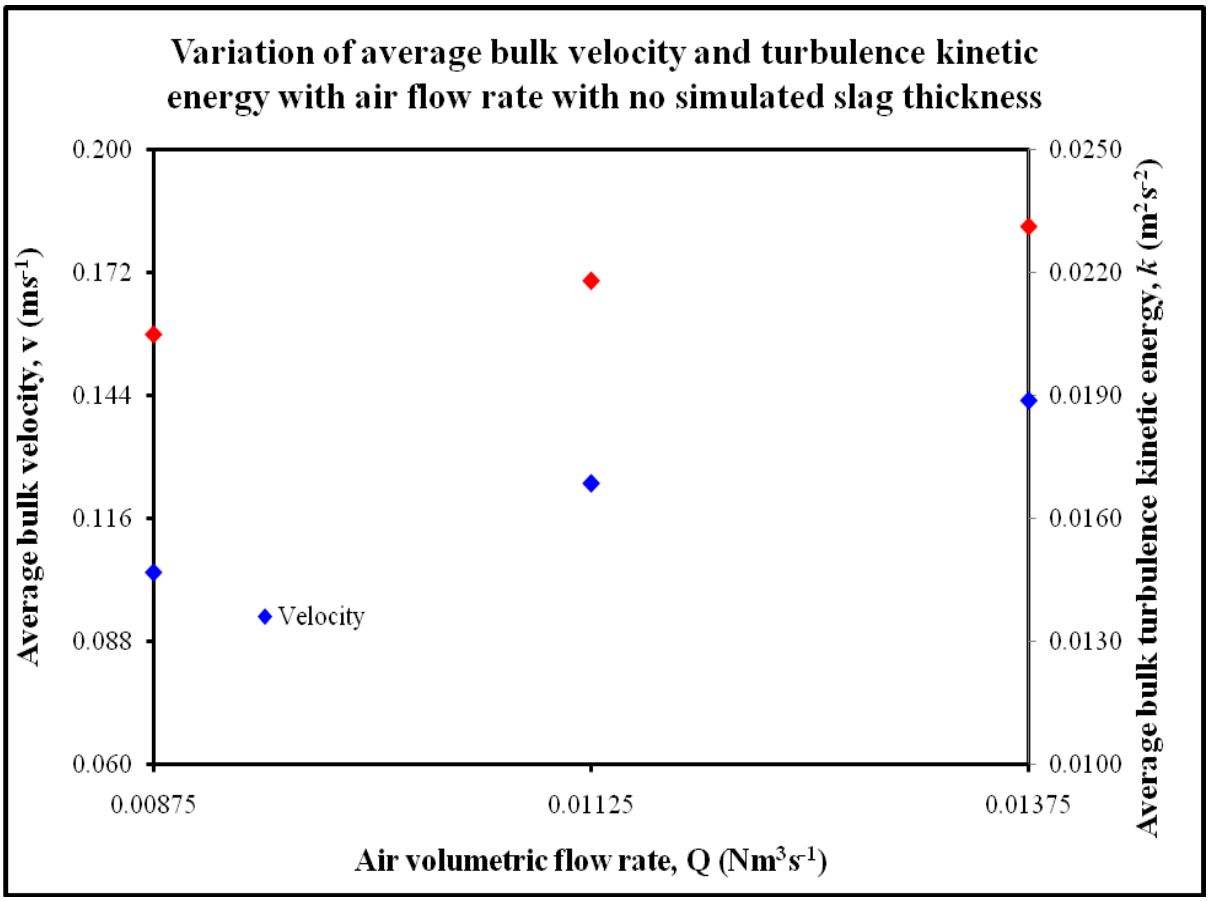

Figure 29: Variation of average simulated matte bulk flow velocity and turbulence kinetic with air flow rate with no simulated slag thickness

The presence of simulated slag has been observed to seriously affect the bulk flow characteristics of the bath. With 54mm simulated slag thickness, both bulk velocity and

turbulence kinetic energy were observed to increase with increase in air volumetric flow rate as shown in **Figure 30**.

In their study on the bubble behavior with gas injected into immersed liquid bath, Komarov et al. (1996) observed that mixing time decreased with increasing specific power of gas injection into the deep bath. On the contrary, mixing time was found to increase with increasing specific power in shallower baths in the studies by Komarov et al. (1996) which is similar to the current bath heights in the current study.

Their work concluded that channeling phenomena was responsible for decrease in mixing efficiency with increasing specific power injected as there will be under utilization of high tuyere air velocity due to channeling. During channeling, injected air channels straight to the bath surface, thereby depriving the bath of potential recirculation power and thus mixing. Liow & Gray (1990a) concluded that bubble plume is narrowed by high gas flow rate and thus caused channeling. Channeling effect reduces momentum transfer to the bath.

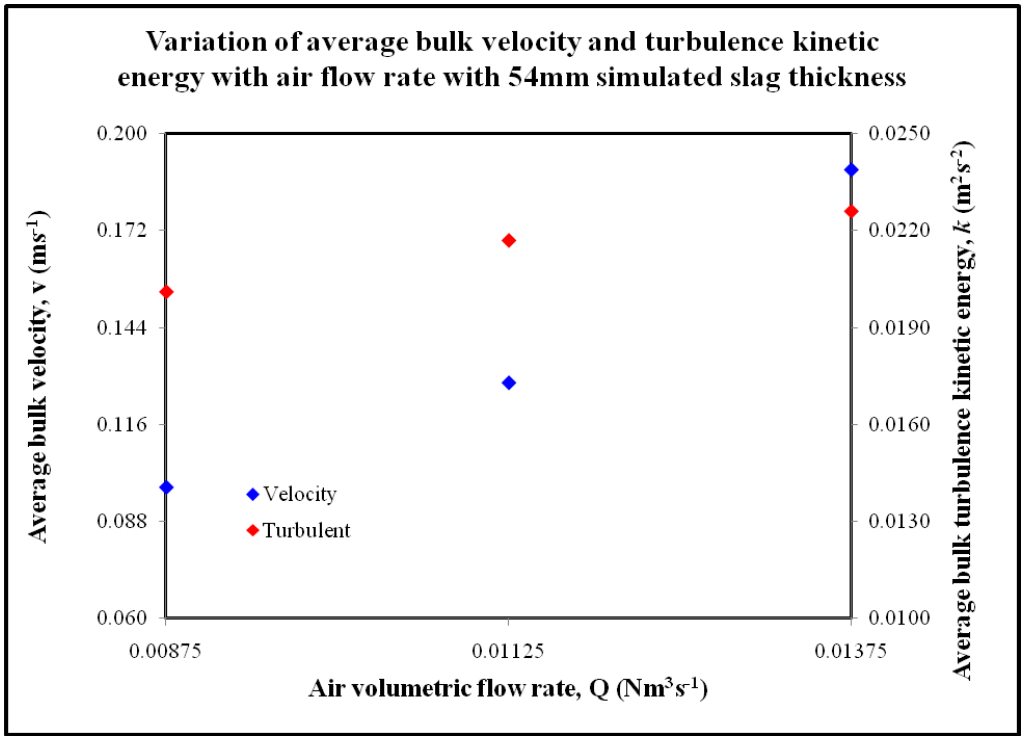

Figure 30: Variation of average simulated matte bulk flow velocity and turbulence kinetic with air flow rate with 54mm simulated slag thickness

Gray et al. (1984) also investigated mixing times in nonferrous converters. They observed that mixing is promoted by large bubbles. Specific power input by injection gas was used to investigate mixing time in their study.

Ashman et al. (1981) have also shown that mixing time depends on the bubble size, which in turn largely depends on the air flow rate, heat transfer and bath circulation velocities as set by the blowing conditions in the reactor. It was postulated and proven in various studies that mixing is promoted by large bubbles as large bubbles increase the turbulence in molten metal (Vaarno et al. 1998).

At 108mm simulated slag thickness, increase in air flow rate up to the nominal flow rate of $0.01125Nm^3s^{-1}$ resulted in decreased both bulk velocity and turbulence kinetic energy. This translates to poor mixing conditions in the converter. In the air flow rate of up to $0.01125Nm^3s^{-1}$ the flow is bubbly and it should be expected to have high mixing efficiency but however phase interactions outweighing the specific mixing power at such high slag volumes. As shown in **Figure 31**, the balance is offset at higher air flow rates, where both recirculation velocity and turbulence kinetic energy in the simulated matte are observed to increase and attain values equivalent to the lowest air flow rate of $0.00875Nm^3s^{-1}$.

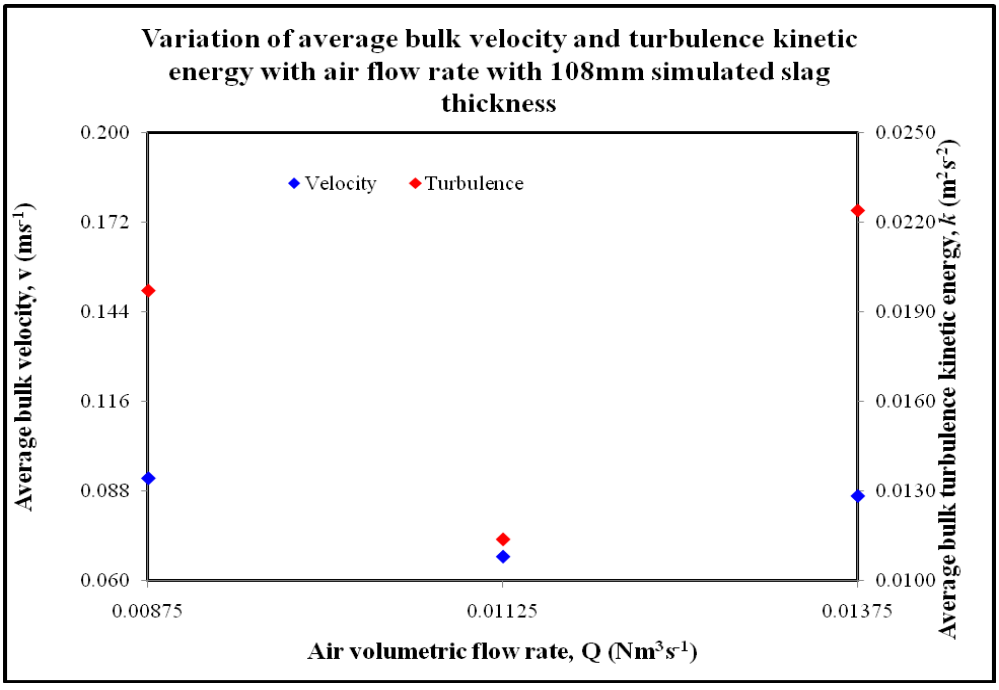

Figure 31: Variation of average simulated matte bulk flow velocity and turbulence kinetic with air flow rate with 108mm simulated slag thickness

Taking into cognisance the fact that $0.01375Nm^3s^{-1}$ is 22% more that the nominal air flow rate of $0.01125Nm^3s^{-1}$, such an increase in flow parameters is not plausible as it comes at extra costs. The results of **Figure 31** serves to indicate that high slag volumes are detrimental

to flow characteristic in the converter, where process performance is measured by the quality and quantity of mixing.

4.1.3 Mixing Time Correlation

In this work, it was assumed that all the specific power due to buoyancy and gas kinetic energy supplied contributed towards model agitation. Using regression analysis, all the mixing time results given in **Appendix A3** were combined and represented by a single T_{mix} in terms of total specific mixing power, ε_m as given in **Figure 32**.

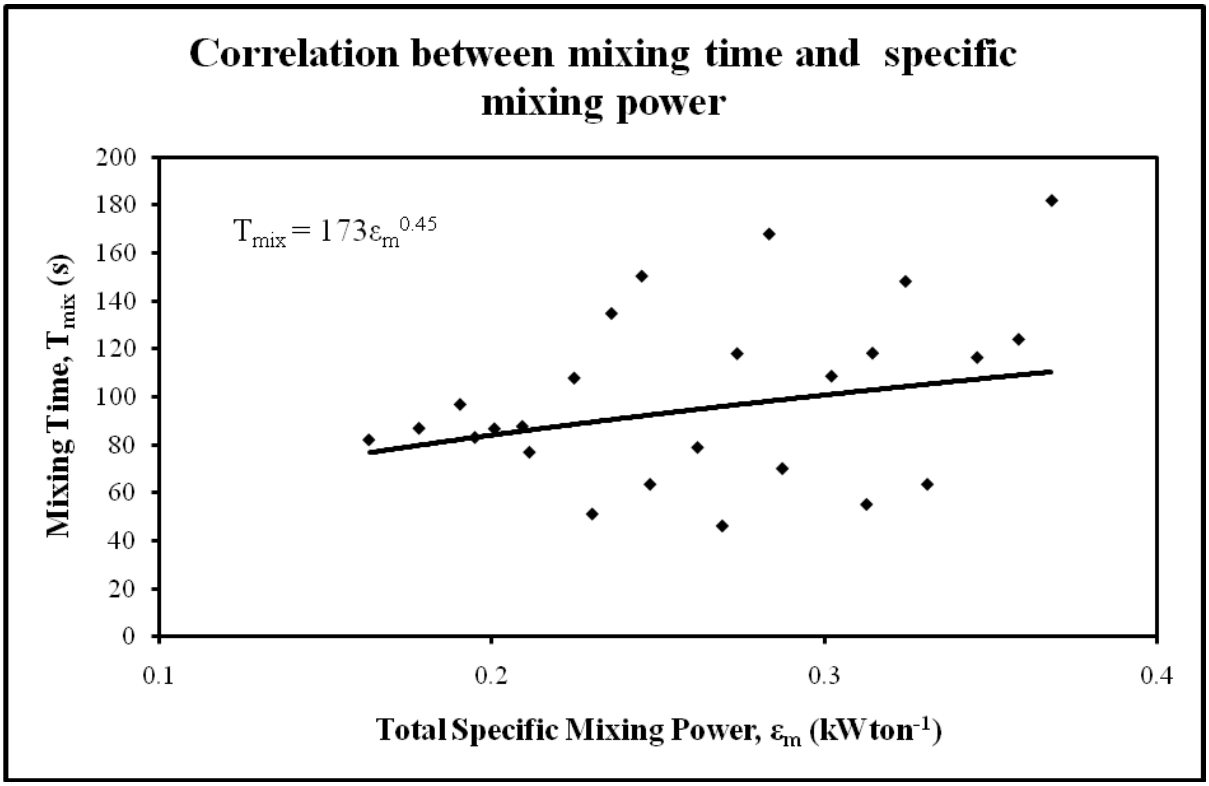

Figure 32: Effect of specific mixing power on mixing time

The above analysis provided the relationship: $T_{mix} = 173\varepsilon_m^{0.45}$ for estimating mixing time in the PSC model.

$$T_{mix} = 173\varepsilon_m^{0.45} \qquad \textbf{Equation 55}$$

The average value for the ratio of specific power due to gas kinetic energy to specific power due to buoyancy $\left(\frac{\varepsilon_k}{\varepsilon_b}\right)$ was calculated to be:

$$\frac{\varepsilon_k}{\varepsilon_b} = 0.21$$ **Equation 56**

Hence it follows from **eq. (32)** that,

$$\varepsilon_m = 5.76\varepsilon_k$$ **Equation 57**

Since $\varepsilon_k = \frac{\rho_g Q^3}{2WA^2}$ from **eq. (31)**, the mixing time correlation **eq. (55)** may be expressed as:

$$T_{mix} = 173\left(5.76\frac{\rho_g Q^3}{2WA^2}\right)^{0.45}$$ **Equation 58**

In the current study, bath weight, W in kg was a summation of simulated matte and simulated slag with simulated matte weight kept constant at 135kg in the model. Regression analysis of the simulated slag thickness, SS_t and the total bath weight, W associated with the quantity of simulated slag yielded results shown in **Figure 33**.

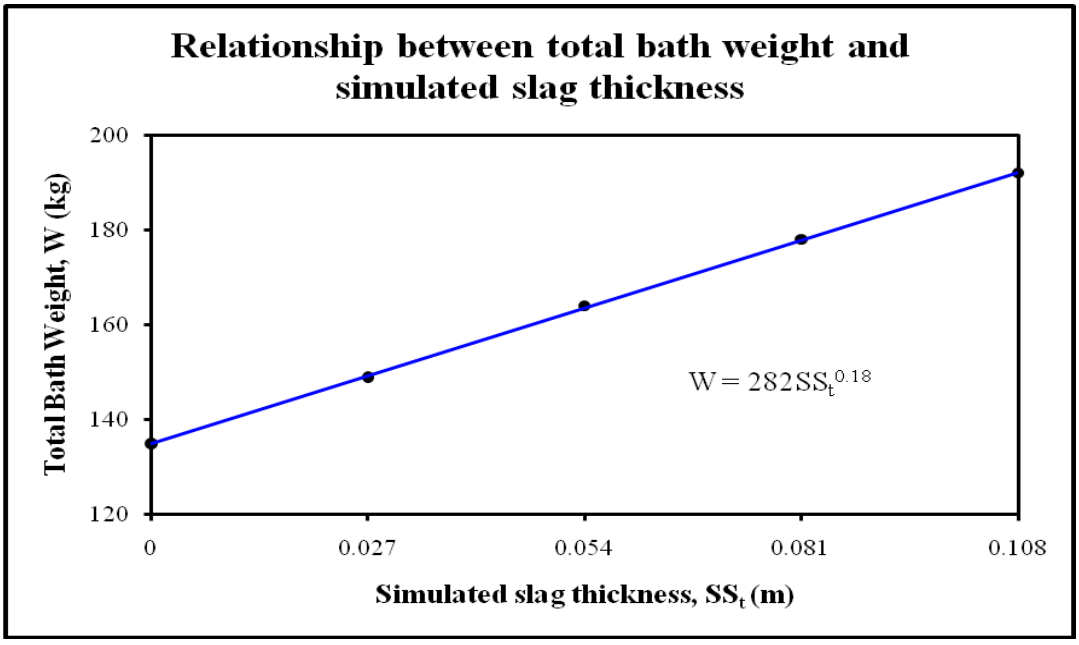

Figure 33: Relationship between total bath weight and simulated slag thickness

$$W = 282SS_t^{0.18}$$ **Equation 59**

Substituting **eq. (59)** into **eq. (58)** yields an application oriented correlation for mixing time estimation in the PSC model:

$$T_{mix} = 30722Q^{1.35}SS_t^{-0.08}$$ **Equation 60**

Where Q (Nm^3s^{-1}) is air flow rate and SS_t (m) is simulated slag thickness in the model.

4.1.4 Numerical Mixing Time Simulations

Mixing time simulations were done to verify the accuracy of physical mixing time experiments. In this work, mixing times at nominal air volumetric flow rate of $0.01125Nm^3s^{-1}$ were carried out at three simulated slag thickness of 54mm, 81mm and 108mm.

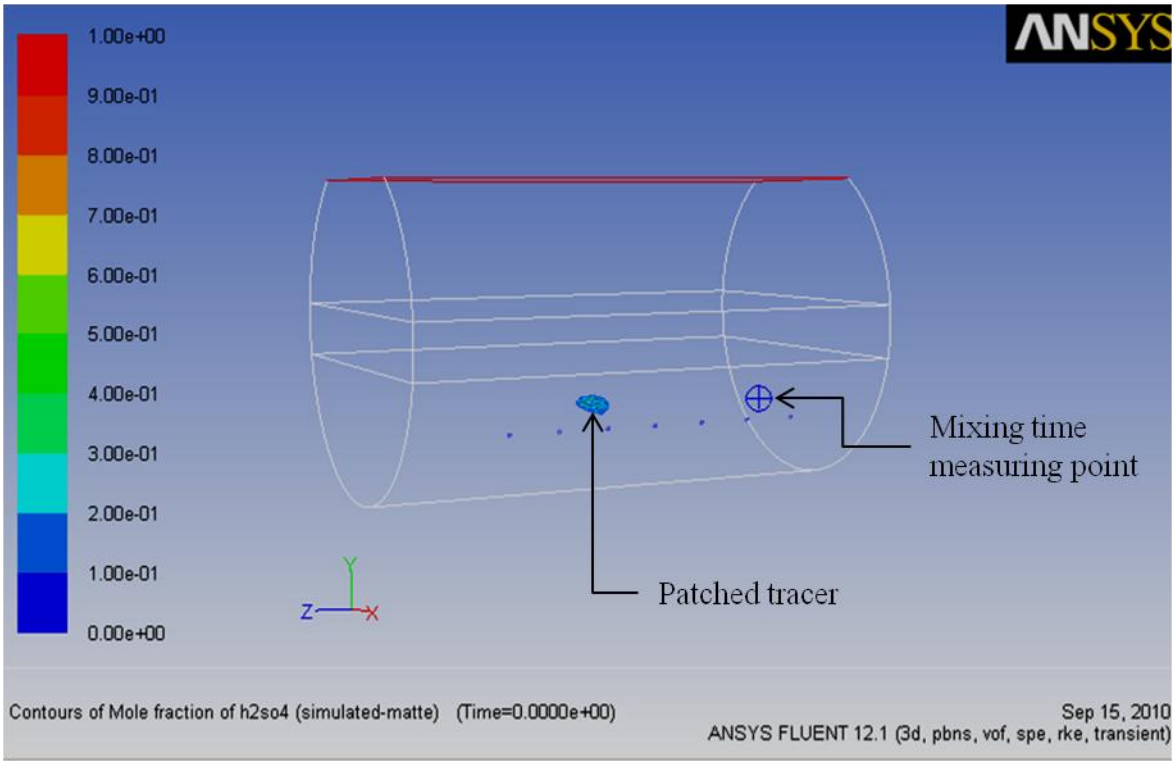

Figure 34: Numerical simulation mixing time tracer injection and dispersion measurement point

A spherical region was marked at the location exactly positioned as the concentrated sulphuric acid addition point in physical mixing time experimental set up as shown in **Figure 34**. Sulpuric acid was patched in this region and at mixing time measurement point, where the pH meter was positioned in the physical mixing time measurement experiments, a surface point was marked where mole fraction of sulphuric acid was measured by means of custom field function.

Figure 35 shows tracer dispersion graph of mixing time measurement for simulated slag thickness of 108mm at air volumetric flow rate of $0.01125Nm^3s^{-1}$.

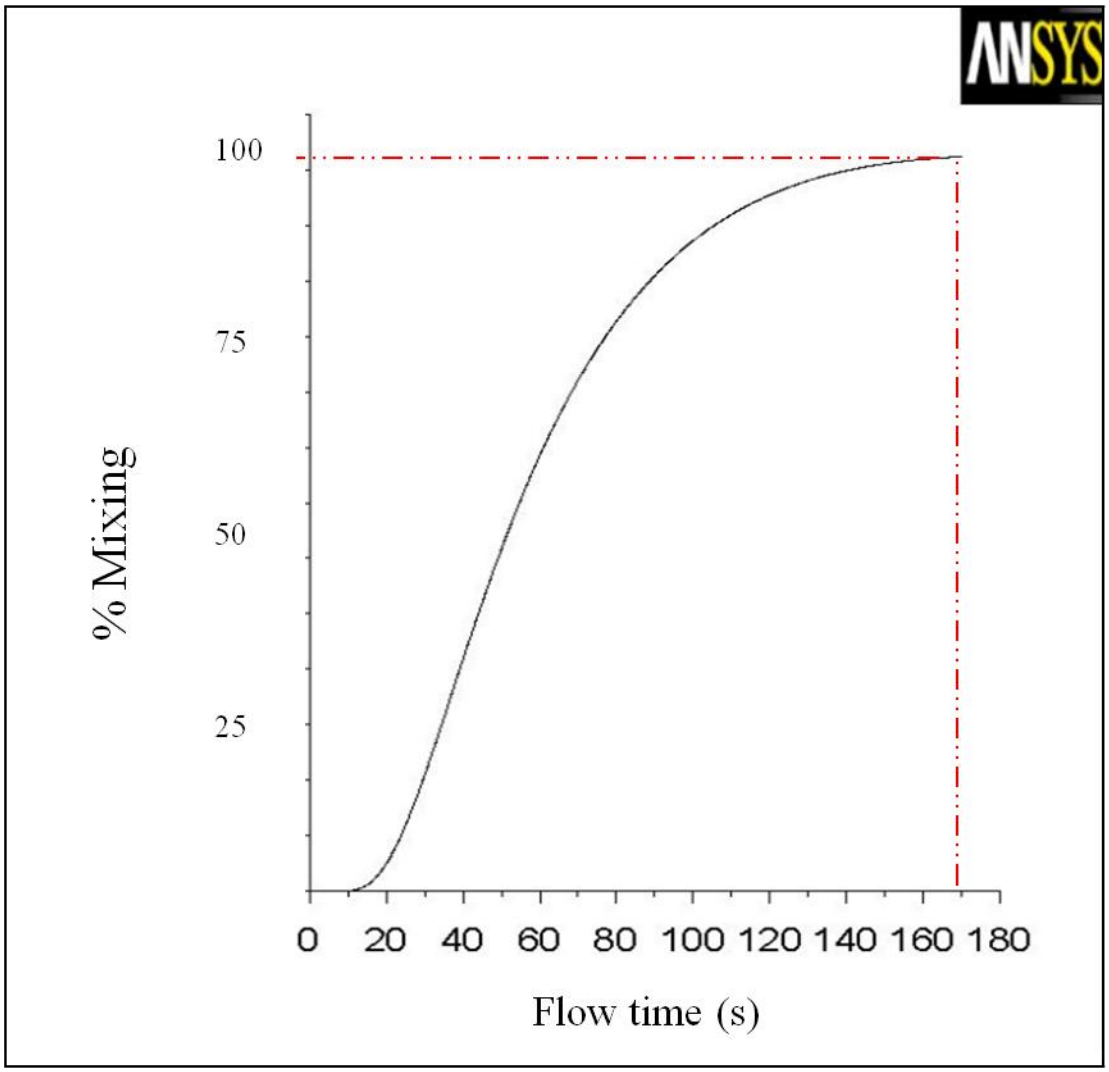

Figure 35: Numerical mixing time graph for 108mm simulated slag thickness at air volumetric flow rate of 0.01125Nm^3s^{-1}

Analysis of **Figure 35** shows that there are possible different transport mechanisms in the initial and final stages of mixing. The initial stages of mixing are likely to be more mass transport related whereas the last stages are characterized by diffusion and convective mechanisms through analysis of the tracer dispersion curve in **Figure 35** which shows that more than 75% of mixing occurs within 40% of total flow time for 99% mixing.

For the three cases considered, the standard deviation of the physical and numerical simulations done was within +/-10% and results are presented in **Figure 36**.

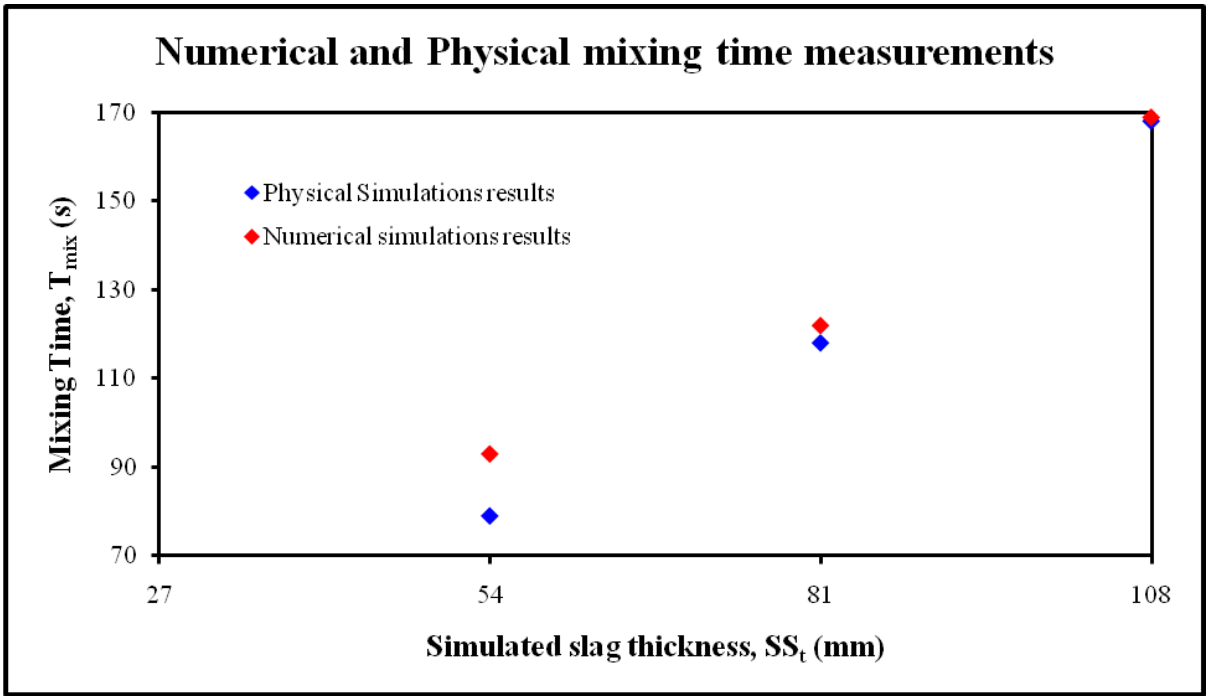

Figure 36: Comparison of numerical and physical mixing time measurements

Figure 36 depicts the numerical and physical simulation results for mixing. As can be seen, both numerical and physical simulation shows a great deal of agreement between them. Results for numerical tracer dispersion curves for 54mm and 81mm simulated slag thicknesses are given in **Appendix A5** in **Graph A1** and **Graph A2** respectively.

From **Figure 37**, recirculation velocity and turbulence kinetic energy, which are the drivers of mixing in this converter, are somewhat depicted to be poorly distributed with high dead zones on the circular side walls as well as the locations opposite the injection points. However, despite that flow parameters are concentrated in the tuyere line region, there must exist a mechanism of flow to redistribute the quantities evenly inside the vessel as PSC are industrially considered well mixed (Vaarno et al. 1998).

Results obtained from mass transfer experiments in this work have also revealed that the flow in the converter is stratified. The streamlines develop from the plume, traversing to the opposite side wall with highest recirculation velocity and turbulence kinetic energy being experienced near the bath surface. This subject will be discussed in the mass transfer experimental results discussion.

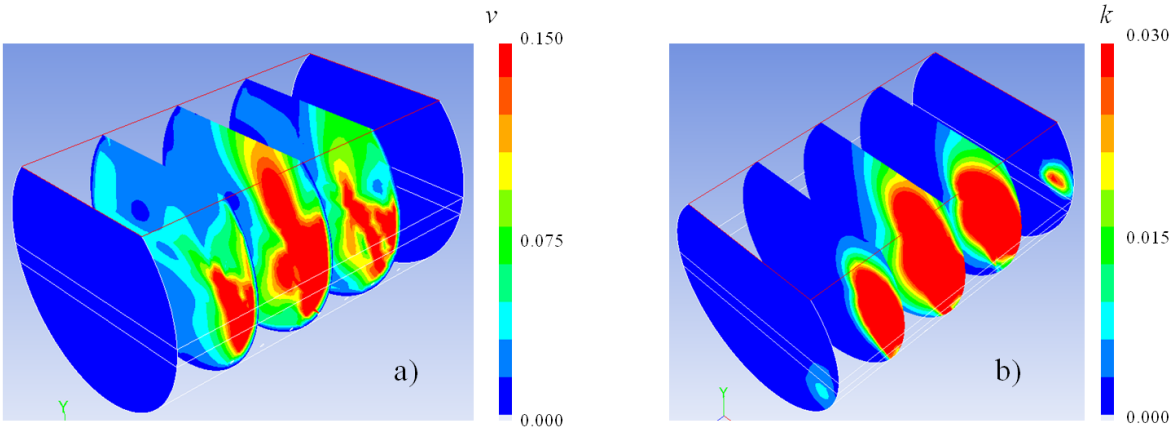

Figure 37: Contours of simulated a) bulk velocity b) turbulence kinetic energy after 5sec of simulation (Air flow rate = 0.01125Nm^3s^{-1}, simulated slag =108mm)

4.2 Solid-liquid Mass Transfer Measurements

Solid-liquid mass transfer rates were investigated as discussed in **section 3.1.3.3**. A weight loss measurement technique was used to assess the rates of dissolution of sintered benzoic acid compacts submerged in the model of the converter. The spatial locations of the cylinders in the model were as given in **section 3.1.3.3.1**. Through varying air flow rate and simulated slag thickness, the behavior of dissolution of the compacts was determined. Mass transfer model of Mazumdar et al. (1990) was used to determine and interpret the results in terms of localized mass transfer coefficients and turbulent parameters.

4.2.1 Effects of Air Volumetric Flow Rate on Mass Transfer

In the spatial distribution of the sintered benzoic acid compacts, the rates of dissolution were observed to be a function of location and depth in the simulated matte bath. **Figure 38**, **Figure 39** and **Figure 40** shows the rates of sample decay at constant simulated slag thickness of 54mm and variable air volumetric flow rates. Sample 2 and Sample 6 have shown to have higher mass transfer rates in all considered air volumetric flow rates. Sample 3 is located at the same position with sample 2, with differing depth. Mass transfer rates for sample 6 which is far off the plume were much higher than sample 3 which is close to the plume.

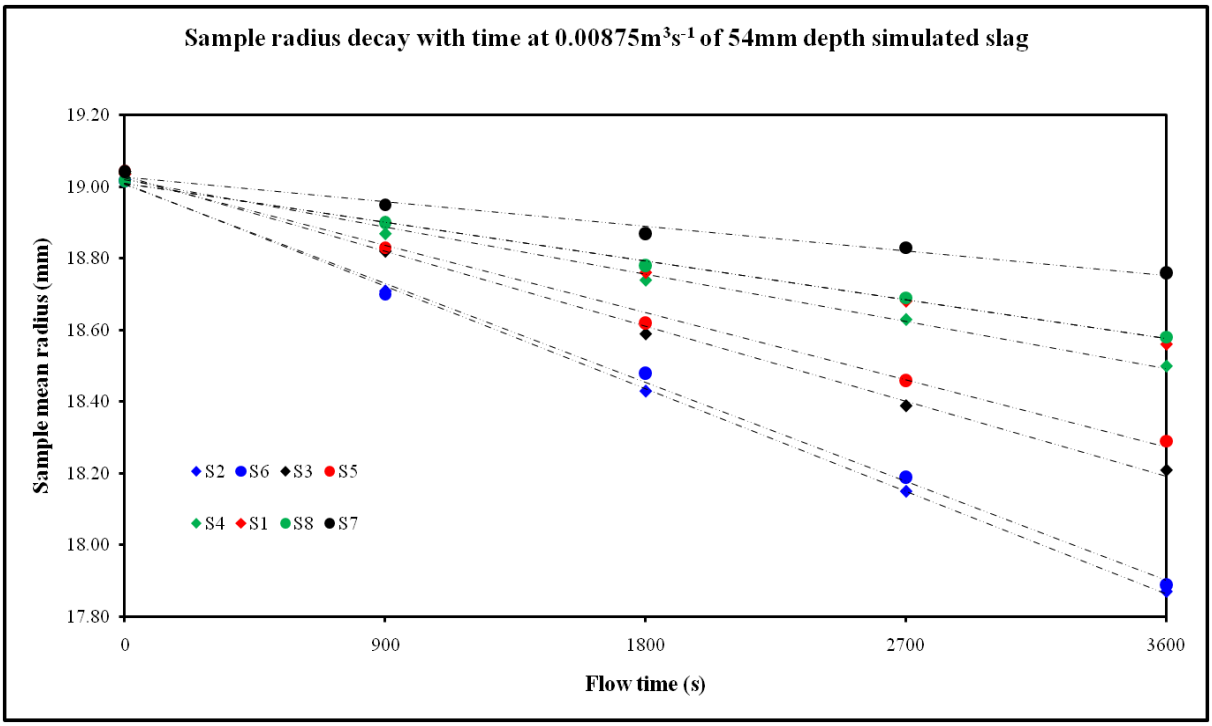

Figure 38: Sample radius decay with time at 0.00875Nm^{3}s^{-1} with 54mm simulated slag thickness

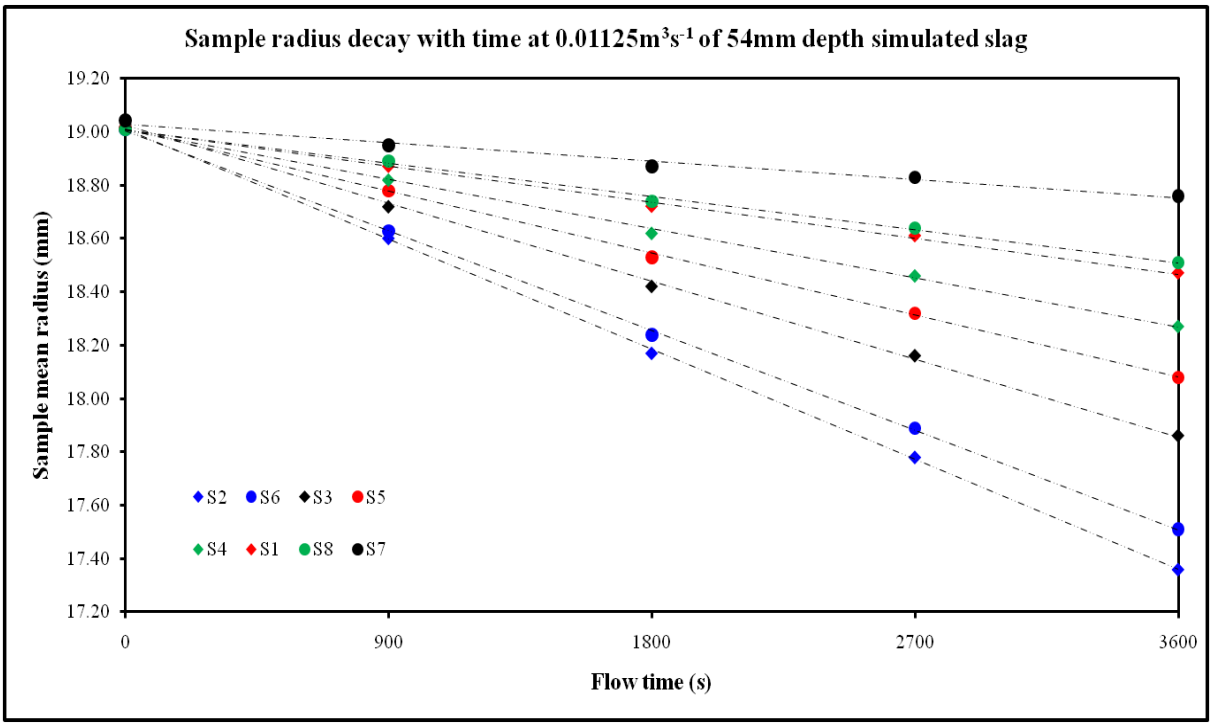

Figure 39: Sample radius decay with time at 0.01125Nm^{3}s^{-1} with 54mm simulated slag thickness

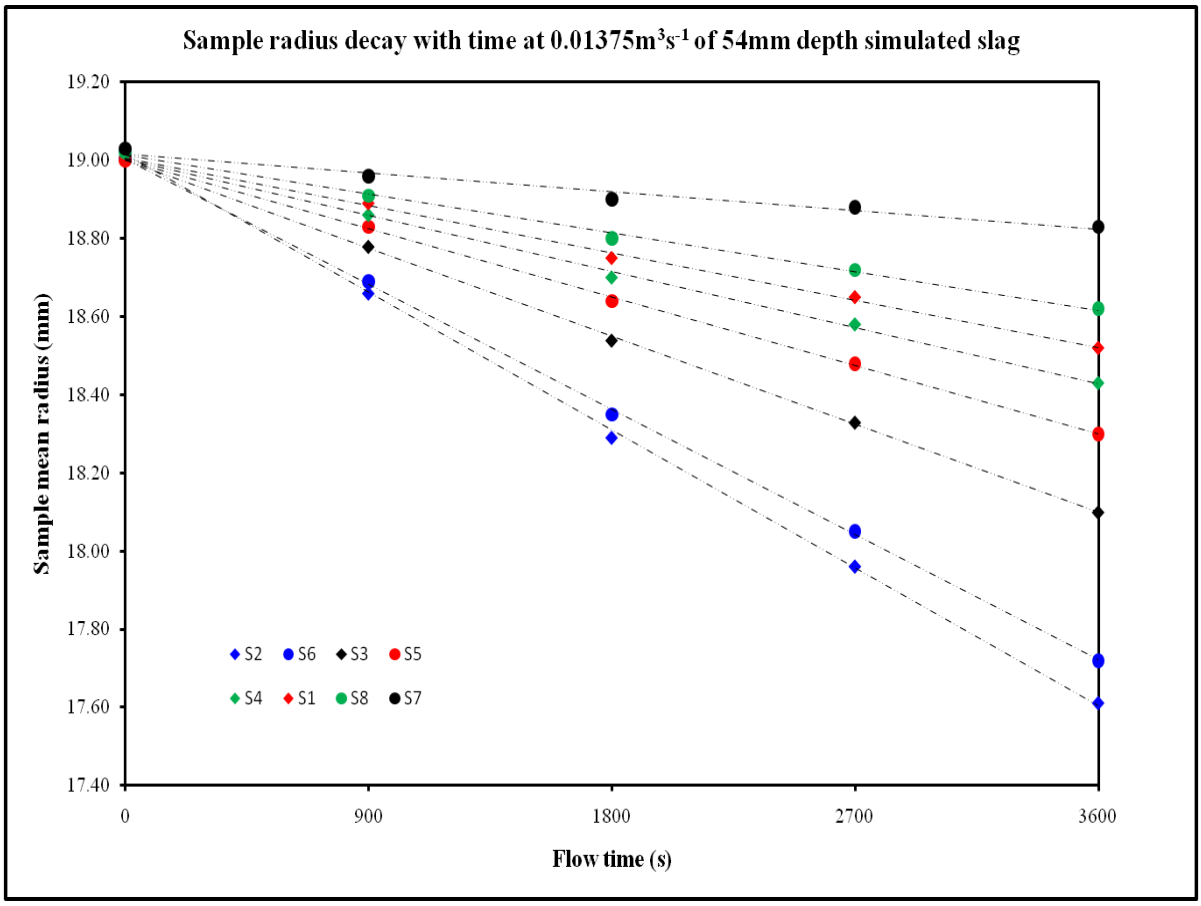

Figure 40: Sample radius decay with time at 0.01375Nm^{3}s^{-1} with 54mm simulated slag thickness

This observation serves to illustrate that the flow in the converter is highly stratified with high velocities being experience near bath surface. Numerical simulation revealed the same behaviour as shown by the contours of velocity magnitude plots in **Figure 41**, **Figure 42** and **Figure 43** showing velocity magnitudes in different planes. High velocity is concentrated in the plume region with residual velocity being experienced on the areas in close proximity. Sample 7 and sample 8 experienced the least dissolution as they are placed in the dead zone of the converter.

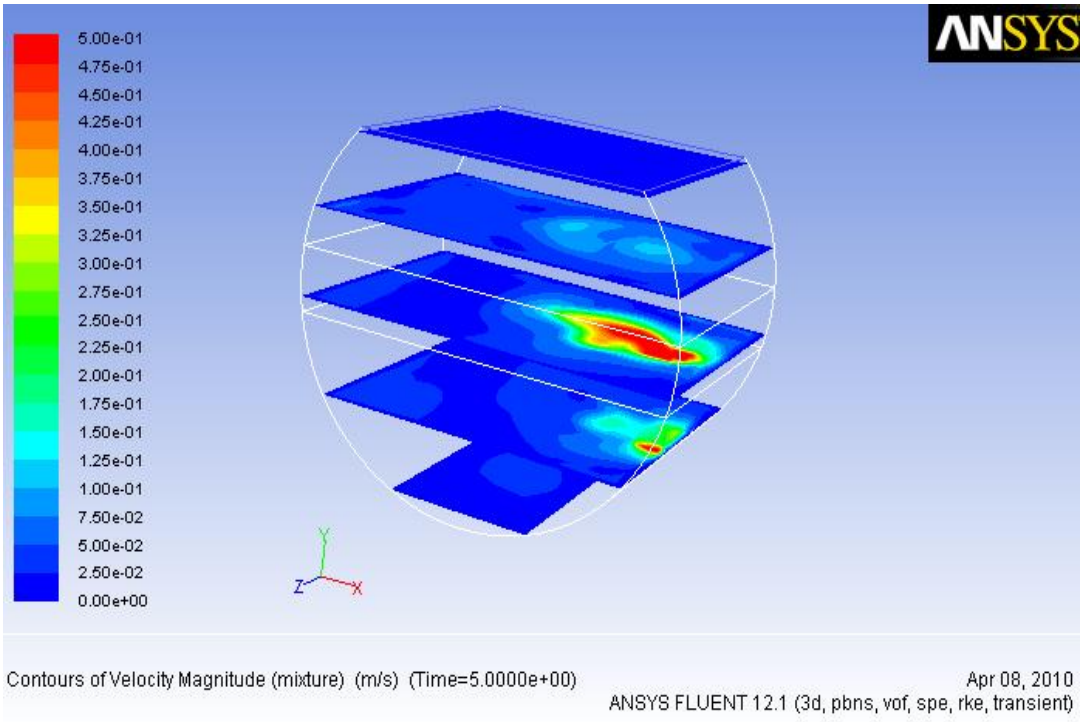

Figure 41: 3-D view for contours of velocity magnitude at 54mm simulated slag thickness (y-direction)

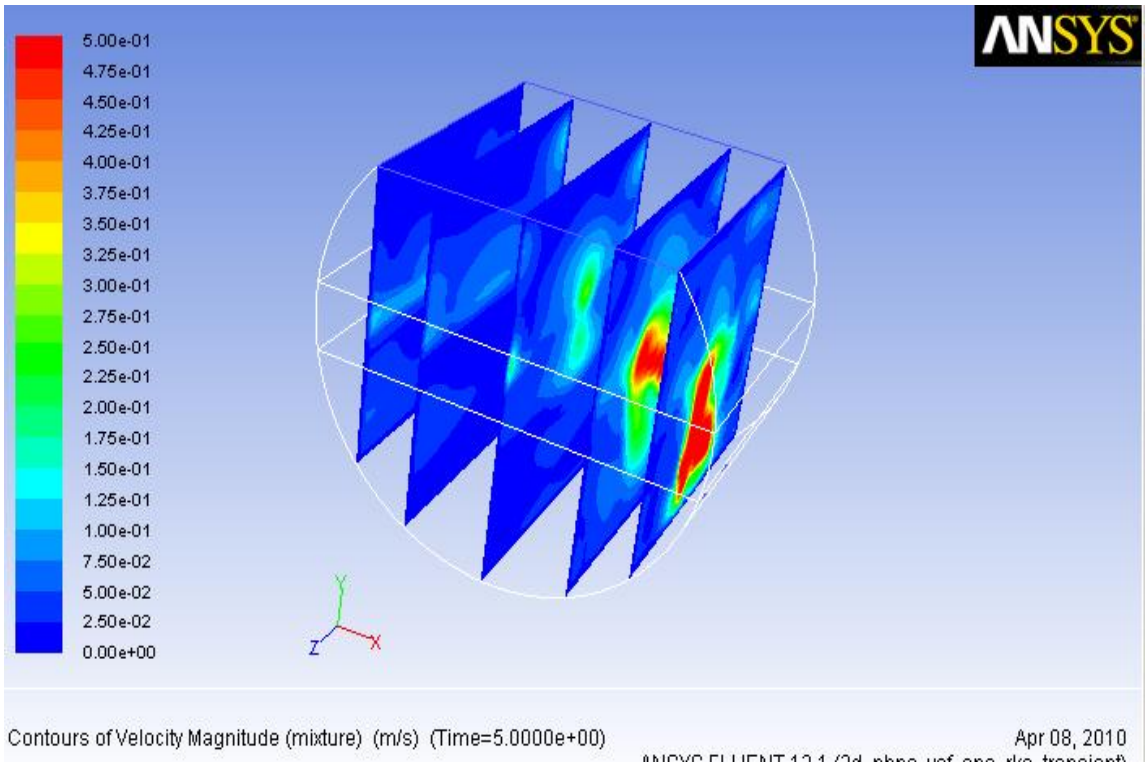

Figure 42: 3-D view for contours of velocity magnitude at 54mm simulated slag thickness (x-direction)

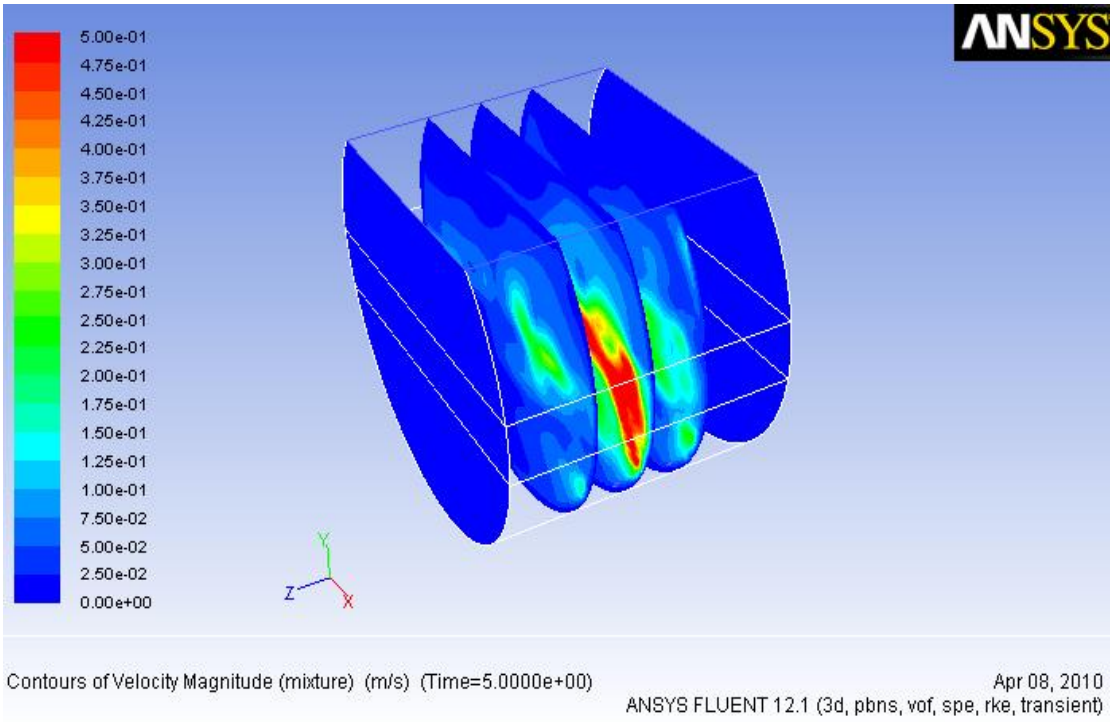

Figure 43: 3-D view for contours of velocity magnitude at 54mm simulated slag thickness (z-direction)

Figure 44 shows the physical simulations calculated mass transfer coefficients with 54mm simulated slag thickness as a function of air volumetric flow rate. As air volumetric flow rate increases, mass transfer coefficients increased on all samples, in agreement with increase in mixing efficiency discussed in **section 4.1.1**.

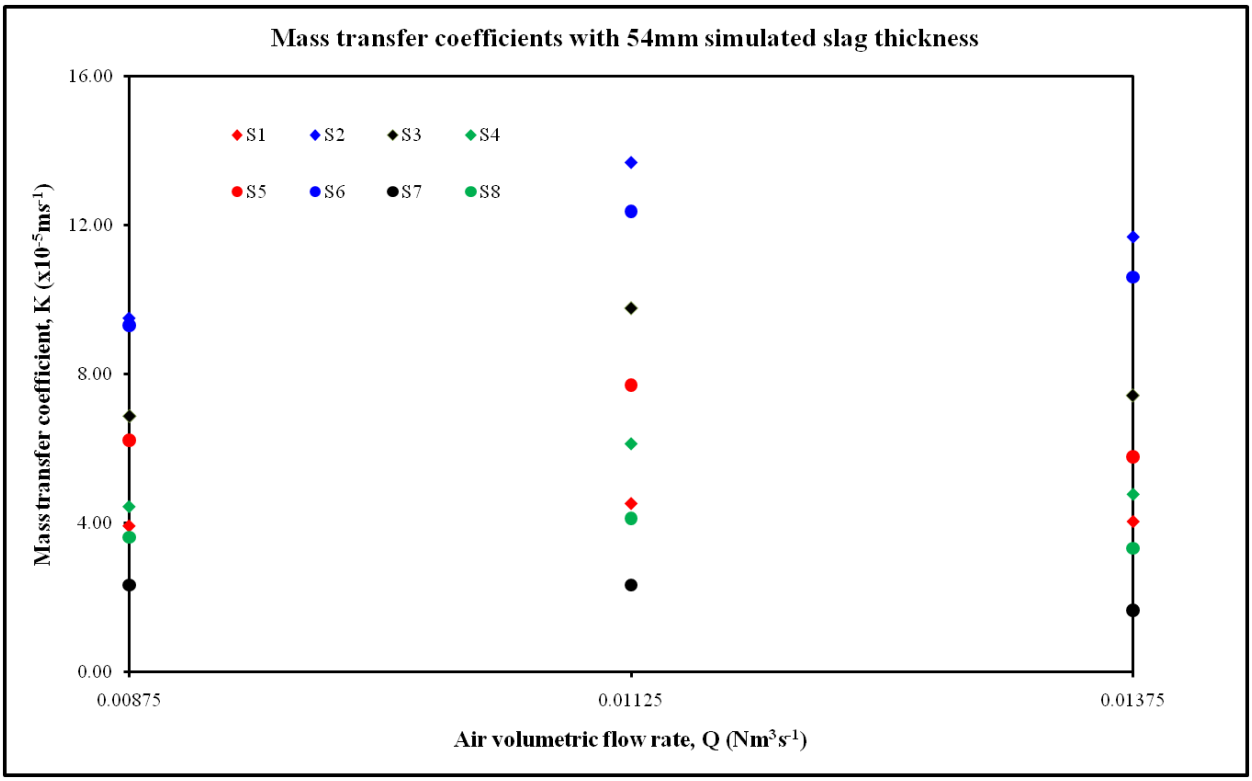

Figure 44: Mass transfer coefficients with 54mm simulated slag thickness

However beyond air volumetric flow rate of 0.01125Nm^3s^{-1}, mass transfer coefficients decreased depicting under-utilization of air flow rate which is attributed to channeling effects as discussed in **section 4.1.2**. Mass transfer results for no simulated slag and 108mm simulated slag scenario are given in **Appendix A6** in **Figure A6 (a)** – **Figure A6 (h)**. It is interesting to observe that **Figure A6 (h)** show a decrease in mass transfer coefficient with increase in air flow rate up to 0.01125Nm^3s^{-1}. This is in consistent with the observed decrease in recirculation velocity and turbulence kinetic energy observed at this condition in mixing time experiments as shown in **Figure 31**.

In light of the above findings, it seems that there exists an optimal condition for air flow rate in the vicinity of 0.01125Nm^3s^{-1}, beyond which further increase in air flow results in under utilization of the gas.

4.2.2 Effects of Simulated Slag on Mass Transfer

As simulated slag thickness increases, turbulence parameters and mass transfer rates were observed decreasing. This is due to the effects of complex phase interactions and phase friction experienced at high slag volumes. However, simulated slag thickness of 54mm was observed to be beneficial as it is at this simulated slag volume that maximum mass transfer

coefficients were obtained as seen in **Figure 45**. The reason for such an observation is temporal effective momentum energy transfer between the bubbles and the bulk liquid due to increase vertical submergence of the tuyeres coupled with minimal phase interaction effects.

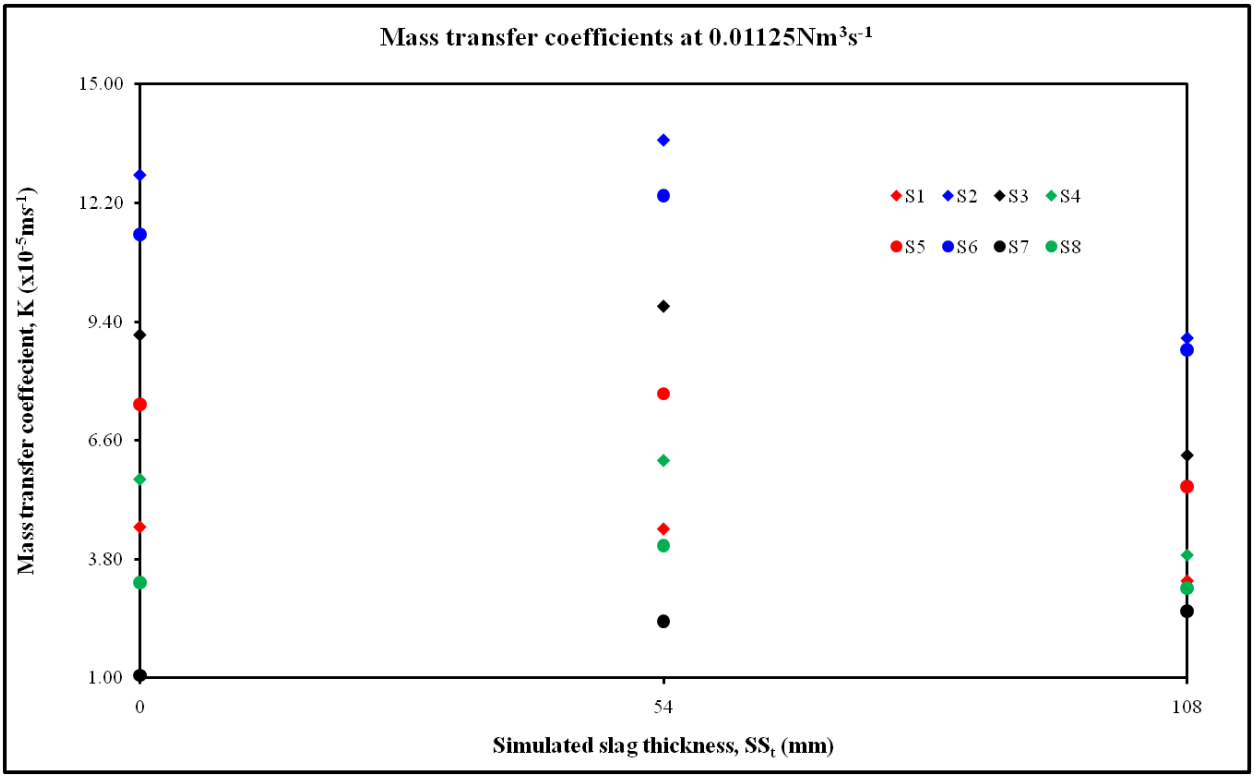

Figure 45: Mass transfer coefficients at 0.01125Nm^{3}s^{-1} as a function of simulated slag thickness

Results for air volumetric flow rates 0.00875Nm^{3}s^{-1} and 0.01125Nm^{3}s^{-1} are shown in **Appendix A6** in **Figure A6 (i)** and **Figure A6 (j)** respectively. It is instructive to note that, although the minimum air flow rate considered in this study is 22% less the nominal air flow rate of 0.01125Nm^{3}s^{-1}, the large bubbles produced from the tuyere inlets at low air flow rates effectively transfers momentum to the bath. This observation is in consistent with Zhao & Irons (1990) and Vaarno et al. (1998) who concluded that large bubbles increase the turbulence in submerged molten metal processing operations in their respective studies. However operation at such low flow rates increases tuyere blockage as well as reduction in oxygenation of the process which is detrimental to the process.

4.3 A Comparison of Mixing and Mass Transfer Rates

In this work, sample 4 used in the mass transfer experiments was positioned at 90mm off-the pH meter measuring point in the radial direction. However it will be assumed that such deviation would not caused much difference to the behavior and response to fluid dynamics in that region. Therefore quantitative comparisons of turbulence characteristic values for this sample with mixing time measured at different air flow rate and simulated slag thickness were carried out.

It has been found out that in all simulated cases, as the turbulent characteristic increases, mixing efficiency increases as a result mixing time decreases. A decrease in turbulence characteristic after air volumetric flow rate of $0.01125 Nm^3s^{-1}$ observed in **Figure 46** is attributable to channeling effects coupled with strong interphase resistances. Such an observation serves to confirm the existence of a correlation between the bulk turbulence and overall process state in terms of mixing efficiency. Results for no slag simulated and 108mm simulated slag thickness are shown in **Appendix A7** in **Figure A7 (a)** and **Figure A7 (b)** respectively. The results exhibited the same characteristics.

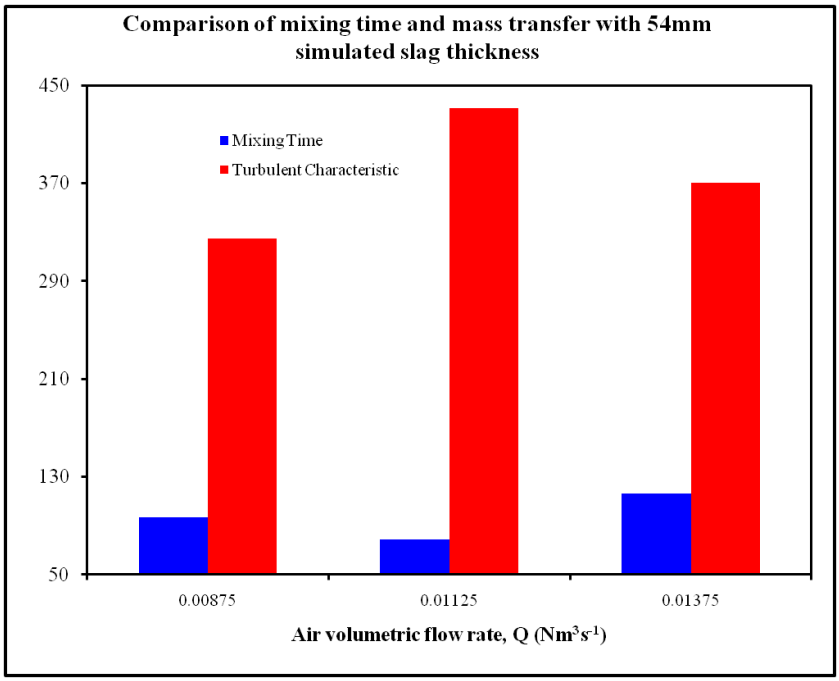

Figure 46: Mixing time and mass transfer comparison with 54mm simulated slag thickness

4.4 Summary of study

Pertinent information about the flow dynamics in the Peirce-Smith converter has been revealed through numerical simulations and physical work done. Mixing time measurements showed that both simulated slag and air volumetric flow rates affect the process turnaround time. The current converter blowing rates have been proved to be optimal blowing conditions at air flow rate of $0.01125 Nm^3 s^{-1}$. Also optimum simulated slag thickness on top of the matte phase was found to be equivalent to 20% of matte depth. These conditions were argued to be beneficial for generation of buoyancy thereby improved bubble-matte power transfer efficiency.

Through observations of mass transfer coefficients at spatial sample arrangements in the model, mapping of the converter was made possible. From these experiments, flow in the converter has been found to be stratified with high velocities achieved at the areas near to the bath surface. Active zones are localized on bath surface and the plume region. However the bulk of the converter assumes low turbulence and recirculation flow field. This behavior is especially pronounced at the circular walls of the converter.

CHAPTER 5

CONCLUSIONS

In this study, we have experimentally and numerically investigated the influence of simulated slag layer on mixing characteristics and behavior in industrial Peirce Smith converter (PSC) via cold model simulations as well as using computational fluid dynamics (CFD).

The 2-D and 3-D simulations of the three phase system were carried out using volume of fluid (VOF) and realizable $k-\varepsilon$ turbulence model to account for the multiphase and turbulence nature of the flow respectively. Experimental results were in good agreement with numerical simulation results in the domain of experimental set-up.

On the basis of the above results and discussions, the main conclusions of this study could be listed as:

- The simulated slag layer as well as air flow rates has a great influence on the bulk recirculation velocity and thus affecting mixing efficiency in the Peirce-Smith converter as suggested by the proposed mixing time correlation:

  $T_{mix} = 30722 Q^{1.35} SS_t^{-0.08}$
- There exists a critical simulated slag thickness in the Peirce-Smith converter model, above which, increasing air flow rate results in extended mixing times due to a combination of channelling and secondary recirculation in the simulated slag. Secondary recirculation results in dissipation of energy resulting in reduced bulk fluid flow recirculation velocity and turbulence kinetic energy.
- Effects of channelling are more pronounced at higher air flow rates above $0.01125 Nm^3 s^{-1}$.
- Increased matte fraction in slag and matte systems increases mixing efficiencies possibly due to high bubble retention.
- Flow streamlines in a Peirce-Smith converter are stratified with higher flow variables experienced in the areas nearer to the bath surface.

- The mixing time and mass transfer results indicated that there exists a correlation between specific mixing power and flow variables characteristics namely; air flow rate, presence of slag and turbulence characteristics.
- High slag volumes are detrimental to the process efficiency as they results in dissipation of potential energy in the converter.
- Numerical modelling can be successfully used to validate and explain physical modelling results.
- Integral flow quantities of the system have suggested a unique liquid transport mechanism that takes place in the converter for it to be homogeneously mixed as there appear to be extended dead volumes in the converter.

CHAPTER 6

RECOMMENDATIONS

The current study has provided an insight into the flow dynamics in a Peirce-Smith converter with cold modelling. It is highly recommended that:

- Full scale mathematical simulation of an operational converter is done with a view to establish potential characterization of the process.
- Simulations be conducted using various simulated slag density to understand the effect of slag compositional differences on flow characteristics.
- Work is done to extend the modelling results (scale-up) of this work and establish a credible scale up criterion to the industrial application.

CHAPTER 7

REFERENCES

1. AKDOGAN, G. and ERIC, R.H., 1999. Model study on mixing and mass transfer in ferroalloy refining processes. *Metallurgical and Materials Transactions B*, **30**(2), pp. 231-239.

2. ANSYS, I., 2008. User's Guide. *Fluent 6.3*

3. ARTERS, D.C. and FAN, L.S., 1986. Solid-liquid mass transfer in a gas-liquid-solid fluidized bed. *Chemical Engineering Science*, **41**(1), pp. 107-115.

4. ASHMAN, D.W., MCKELLIGET, J.W. and BRIMACOMBE, J.K., 1981. Mathematical model of bubble formation at tuyeres of copper converter. *Canadian Metallurgical Quarterly*, **20**, pp. 387-395.

5. BAXAMUSA, B.N., Available: http://www.buzzle.com/articles/copper-uses-of-copper.html [February 2010]

6. BEZUIDENHOUT, J.J., 2008. *Computational fluid dynamic modelling of an electric smelting furnace in platinum recovery process*, University of Stellenbosch.

7. CAMEO CHEMICALS, Dec 1999, 1999-last update, Kerosene [Homepage of Cameo Chemicals], [Online]. Available: http://cameochemicals.noaa.gov/chris/KRS.pdf [February 2010]

8. CASTILLEJOS, A.H. and BRIMACOMBE, J.K., 1987. Measurement of physical characteristics of bubbles in gas-liquid plumes: Part II. Local properties of turbulent air-water plumes in vertically injected jets. *Metallurgical and Materials Transactions B*, **18**(4), pp. 659-671.

9. CLOETE, S., OLSEN, J.E. and SKJETNE, P., 2009. CFD modeling of plume and free surface behavior resulting from a sub-sea gas release. *Applied Ocean Research*, **31**(3), pp. 220-225.

10. DAVENPORT, W.G., KING, M., BISWAS, A.K. and SCHLESINGER, M., 2002. *Extractive metallurgy of copper*. 4th edn. Pergamon Pr.

11. DENSITY OF AIR, , Wikipedia [Homepage of Wikimedia], [Online]. Available: http://en.wikipedia.org/wiki/Density_of_air [August 2010].

12. FABRITIUS, T., KUPARI, P. and HÄRKKI, J., 2002. Physical modelling of a sidewall-blowing converter. *Scandinavian Journal of Metallurgy*, **30**(2), pp. 57-64.

13. FRANKEL, M.L. and FRANKEL, M., 2009. *Facility Piping Systems Handbook: For Industrial, Commercial, and Healthcare Facilities*. McGraw-Hill Professional.

14. GONZALEZ, J., REAL, C., PALOMAR-PARDAVE, M., HOYOS, L., GUTIERREZ, M. and MIRANDA, R., 2008. CFD simulation gas-liquid flow in a copper converter with bottom air injection. *International Journal of Chemical Reactor Engineering*, **6**(6), pp. 54.

15. GRAY, N.B., NILMANI, M. and FOUNTAIN, C.R., 1984. Investigation and modelling of gas injection and mixing in molten liquid processes. *The Aus.I.M.M Melbourne branch, Symposium on Extractive Metallurgy*, , pp. 269-277.

16. HAIDA, O. and BRIMACOMBE, J.K., 1985. Physical-Model Study of the Effect of Gas Kinetic Energy in Injection Refining Processes. *Trans.Iron Steel Inst.Jpn.*, **25**(1), pp. 14-20.

17. HAN, J.W., HEO, S.H., KAM, D.H., YOU, B.D., PAK, J.J. and SONG, H.S., 2001. Transient fluid flow phenomena in a gas stirred liquid bath with top oil layer—Approach by numerical simulation and water model Experiments. *ISIJ International*, **41**(10), pp. 1165-1172.

18. HOEFELE, E.O. and BRIMACOMBE, J.K., 1979. Flow regimes in submerged gas injection. *Metallurgical and Materials Transactions B*, **10**(4), pp. 631-648.

19. IMRIS, I., SANCHEZ, M. and ACHURRA, G., 2005. Copper losses to slags obtained from the El Teniente process. *Mineral Processing and Extractive Metallurgy*, **114**(3), pp. 135-140.

20. JOHANSEN, E.M., 1924. The Interfacial Tension between Petroleum Products and Water. *Industrial & Engineering Chemistry,* **16**(2), pp. 132-135.

21. KIM, S.H. and FRUEHAN, R.J., 1987. Physical modeling of liquid/liquid mass transfer in gas stirred ladles. *Metallurgical and Materials Transactions B,* **18**(2), pp. 381-390.

22. KOMAROV, S., DIAZ, M. and SANO, M., 1996. Gas injection through immersed rotary lances, *The Howard Worner International Symposium on Injection in Pyrometallurgy*, 1996, , pp. 267-274.

23. KOOHI, A.H.L., HALALI, M., ASKARI, M. and MANZARI, M.T., 2008. Investigation and Modeling of Splashing in the Peirce-Smith converter. *Chemical Product and Process Modeling*, **3**(1), pp. 2.

24. KORIA, S.C., 1988. Liquid-Solid mass transfer measurements in gas stirred metallurgical vessels. *Steel Research International*, **59**(3), pp. 484-491.

25. YLLO, A.K. and RICHARDS, G.G., 1998a. A kinetic model of Peirce-Smith converter: Part I. Model formulation and validation. *Metallurgical Transactions B,* **29B**, pp. 239-250.

26. KYLLO, A.K. and RICHARDS, G.G., 1998b. A kinetic model of Peirce-Smith converter: Part II. Model application and discussion. *Metallurgical Transactions B,* **29B**, pp. 251-259.

27. LIOW, J.L. and GRAY, N.B., 1990a. Slopping resulting from gas injection in a Peirce-Smith converter: The period of the standing wave. *Metallurgical and Materials Transactions B,* **21**(4), pp. 657-664.

28. LIOW, J.L. and GRAY, N.B., 1990b. Slopping resulting from gas injection in a Pierce-Smith converter: Water model. *Metallurgical and Materials Transactions B,* **21**(6), pp. 987-996.

29. MAZUMDAR, D., 1990. Dynamic similarity considerations in gas-stirred ladle systems. *Metallurgical and Materials Transactions B,* **21**(5), pp. 925-928.

30. MAZUMDAR, D. and EVANS, J.W., 2004. Macroscopic models for gas stirred ladles. *ISIJ International,* **44**(3), pp. 447-461.

31. MAZUMDAR, D. and GUTHRIE, R.I.L., 1986. Mixing models for gas stirred metallurgical reactors. *Metallurgical and Materials Transactions B,* **17**(4), pp. 725-733.

32. MAZUMDAR, D., KAJANI, S.K. and GHOSH, A., 1990. Mass transfer between solid and liquid in vessels agitated by bubble plume. *Process Metallurgy steel research,* **61**(8), pp. 339-346.

33. MAZUMDAR, D., NAKAJIMA, H. and GUTHRIE, R.I.L., 1988. Possible roles of upper slag phases on the fluid dynamics of gas stirred ladles. *Metallurgical and Materials Transactions B,* **19**(3), pp. 507-511.

34. MERLE, C.P. and DAVID, C.W., 1997. *Mechanics of fluids.* Third edn. United States of America: Prentice Hall, Upper Saddle River, NJ.

35. NAKANISHI, K., FUJII, T. and SZEKELY, J., 1975. Possible relationship between energy dissipation and agitation in steel processing operations. *Ironmaking Steelmaking,* **3**(2), pp. 193-197.

36. NIKOV, I. and DELMAS, H., 1987. Solid-liquid mass transfer in three-phase fixed and fluidized beds. *Chemical Engineering Science,* **42**(5), pp. 1089-1093.

37. NYOKA, M., AKDOGAN, G., ERIC, R.H. and SUTCLIFFE, N., 2003. Mixing and solid-liquid mass transfer rates in a Creusot Loire Uddeholm vessel: A water model case study. *Metallurgical and Materials Transactions B,* **34**(6), pp. 833-842.

38. PANTON, R.L., 1984. Incompressible flow.

39. PRAKASH, A., BRIENS, C.L. and BERGOUGNOU, M.A., 1987. Mass transfer between solid particles and liquid in a three phase fluidized bed. *The Canadian Journal of Chemical Engineering,* **65**(2), pp. 228-236.

40. RAMIREZ-ARGAEZ, M.A., 2008. Numerical simulation of fluid flow and mixing in gas-stirred ladles. *Materials and Manufacturing Processes,* **23**(1), pp. 59-68.

41. REAL, C., HOYOS, L., CERVANTES, F., MIRANDA, R., PALOMAR-PARDAVE, M., BARRON, M. and GONZALEZ, J., 2007. Fluid characterization of copper converters. *Mecánica Computacional,* **26**, pp. 1311-1323.

42. ROSALES, M., FUENTES, R., RUZ, P. and GODOY, J., 1999. A fluid dynamic simulation of a Teniente Converter. *Copper 99- Cobre 99,* , pp. 107-121.

43. ROSALES, M., VALENCIA, A. and FUENTES, R., 2009. A Methodology for Controlling Slopping in Copper Converters by Using Lateral and Bottom Gas Injection. *International Journal of Chemical Reactor Engineering,* **7**(1), pp. 1868.

44. SAHAI, Y. and GUTHRIE, R.I.L., 1982. Hydrodynamics of gas stirred melts: Part I. Gas/liquid coupling. *Metallurgical and Materials Transactions B,* **13**(2), pp. 193-202.

45. SALAS, M.D., HEFNER, J.N. and SAKELL, L., 1999. *Modeling complex turbulent flows.* Kluwer Academic Publishers.

46. SCHWARZ, M.P., 1996. Simulation of gas injection into liquid melts. *Applied Mathematical Modelling,* **20**(1), pp. 41-51.

47. SHELL, B.P., Shell Illuminating paraffin.

Available: http://www.shell.com/home/content/zaf/products_services/ [August 2009]

48. SHIH, T.H., LIOU, W.W., SHABBIR, A., YANG, Z. and ZHU, J., 1995. A new k-[epsilon] eddy viscosity model for high reynolds number turbulent flows. *Computers & Fluids,* **24**(3), pp. 227-238.

49. SINGH, A.K. and MAZUMDAR, D., 1997. Mass transfer between solid and liquid in a gas-stirred vessel. *Metallurgical and Materials Transactions B,* **28**(1), pp. 95-102.

50. SINGH, R.P. and MCNALLAN, M.J., 1983. Fluid dynamics and mass transfer in submerged gas-particle jets. *Metallurgical and Materials Transactions B,* **14**(3), pp. 425-434.

51. SINHA, U.P. and MCNALLAN, M.J., 1985. Mixing in ladles by vertical injection of gas and gas-particle jets—A water model study. *Metallurgical and Materials Transactions B,* **16**(4), pp. 850-853.

52. SNYDERS, C.A., 2008. *Modelling the thermal, electrical and flow profiles in a 6-In-Line matte smelting furnace*, University of Stellenbosch.

53. STAPUREWICZ, T. and THEMELIS, N.J., 1987. Mixing and Mass Transfer Phenomena in Bottom-Injected Gas--Liquid Reactors. *Can.Metall.Q.,* **26**(2), pp. 123-128.

54. SULLIVAN, T.J., 2008. *Sulphuric Acid Handbook.* 6th edn. USA: Bibliobazaar.

55. SULPHURIC ACID, The free encyclopedia [Homepage of Wikimedia], [Online]. Available: http://en.wikipedia.org/wiki/Sulfuric_acid [February 2010].

56. SYAMUJULU, M., 2005. A technical and operational audit of the First ten years of the Teniente converter operations at Nkana smelter. JOURNAL - SOUTH AFRICAN INSTITUTE OF MINING AND METALLURGY, **105**(9), 627 - 640

57. SZEKELY, J., DILAWARI, A.H. and METZ, R., 1979. The mathematical and physical modeling of turbulent recirculating flows. *Metallurgical and Materials Transactions B,* **10**(1), pp. 33-41.

58. SZEKELY, J., EVANS, J.W. and BRIMACOMBE, J.K., 1988. The development of rigorous physical models. *The mathematical and physical modeling of primary metals processing operations.* USA: John Wiley & Sons, Inc, pp. 69-99.

59. SZEKELY, J., LEHNER, T. and CHANG, C.W., 1979. Flow Phenomena, Mixing, and Mass Transfer in Argon-Stirred Ladles. *Ironmaking Steelmaking,* **6**(6), pp. 285-293.

60. THE ENGINEERING TOOLBOX, , The Engineering ToolBox [Homepage of Google], [Online]. Available: http://www.engineeringtoolbox.com/water-surface-tension-d_597.html [June 09, 2010].

61. TURKOGLU, H. and FAROUK, B., 1991. Mixing time and liquid circulation rate in steelmaking ladles with vertical gas injection. *ISIJ International,* **31**(12), pp. 1371-1380.

62. VAARNO, J., PITKÄLÄ, J., AHOKAINEN, T. and JOKILAAKSO, A., 1998. Modelling gas injection of a Peirce-Smith-converter. *Applied Mathematical Modelling,* **22**(11), pp. 907-920.

63. VAISBURD, S., BRANDON, D.G., KOZHAKHMETOV, S. and KENZHALIYEV, E., 2002. Physicochemical properties of matte-slag melts taken from Vanyukov's furnace for copper extraction. *Metallurgical and Materials Transactions B,* **33**(4), pp. 561-564.

64. VALENCIA, A., CORDOVA, M. and ORTEGA, J., 2002. Numerical simulation of gas bubbles formation at a submerged orifice in a liquid. *International Communications in Heat and Mass Transfer,* **29**(6), pp. 821-830.

65. VALENCIA, A., PAREDES, R., ROSALES, M., GODOY, E. and ORTEGA, J., 2004. Fluid dynamics of submerged gas injection into liquid in a model of copper converter. *International Communications in Heat and Mass Transfer,* **31**(1), pp. 21-30.

66. VALENCIA, A., ROSALES, M., PAREDES, R., LEON, C. and MOYANO, A., 2006. Numerical and experimental investigation of the fluid dynamics in a Teniente type copper converter. *International Communications in Heat and Mass Transfer,* **33**(3), pp. 302-310.

67. VERSTEEG, H.K. and MALALASEKERA, W., 2007. *An introduction to computational fluid dynamics: the finite volume method.* Second edn. England: Prentice Hall.

68. WEI, J.H., 2002. Physical and mathematical modeling of the argon-oxygen decarburization refining process of stainless steel. *Journal of Shanghai University (English Edition),* **6**(1), pp. 1-23.

69. WILCOX, D.C., 1994. *Turbulence modeling for CFD.* Second edn. United States of America: DCW Industries, Inc.

70. ZHAO, Y.F. and IRONS, G.A., 1990. The breakup of bubbles into jets during submerged gas injection. *Metallurgical and Materials Transactions B,* **21**(6), pp. 997-1003.

71. ZHU, M.Y., SAWADA, I., YAMASAKI, N. and HSIAO, T.C., 1996. Numerical simulation of three-dimensional fluid flow and mixing process in gas-stirred ladles. *ISIJ International,* **36**(5), pp. 503-511.

72. ŽIVKOVIĆ, Ž., MITEVSKA, N., MIHAJLOVIĆ, I. and NIKOLIĆ, Đ., 2009. The influence of the silicate slag composition on copper losses during smelting of the sulfide concentrates. *Journal of Mining and Metallurgy B: Metallurgy,* **45**(1), pp. 23-34.

CHAPTER 8

APPENDICES

Appendix A 1: Blowing parameters derived with temperature correction

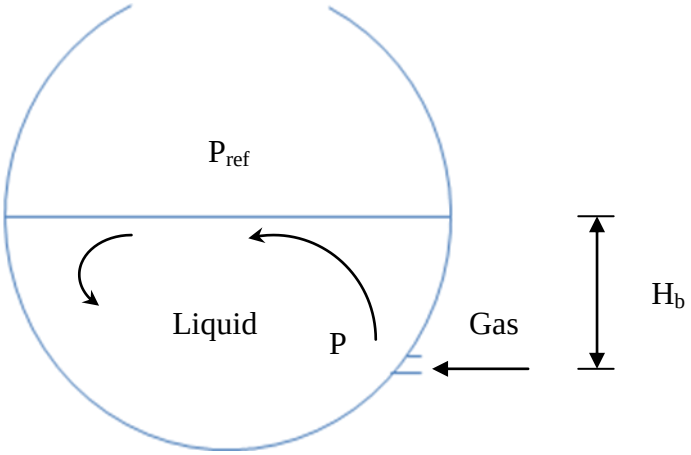

Figure 2: Pressure distribution in a converter

The actual blow rate at operating conditions is given by:

$$Q_{Act,ptype} = \left(\frac{T}{P}\right) \cdot \left(\frac{P_{ref}}{T_{ref}}\right) \cdot Q_{Nor,ptype} \quad [1]$$

Tuyere static pressure, P = 115 289 therefore actual blowing volumetric flow rate is:

$$Q_{Act,ptype} = \left(\frac{1493}{115289}\right) \cdot \left(\frac{101325}{273}\right) \cdot Q_{Nor,ptype} = 4.806 Q_{Nor,ptype} \quad [2]$$

Assuming that there is an instantaneous transfer of heat from the liquid to injected gas to the liquid temperature, then the density of gas in prototype is given by:

$$\rho_g = 1.205\left(\frac{P}{T}\right)\cdot\left(\frac{T_{ref}}{P_{ref}}\right) = 1.205\left(\frac{115289}{1493}\right)\cdot\left(\frac{273}{101325}\right) = 0.25 kgm^{-3} \quad [3]$$

Likewise, the density of gas in the model is given by:

$$\rho_g = 1.205\left(\frac{P}{T}\right)\cdot\left(\frac{T_{ref}}{P_{ref}}\right) = 1.205\left(\frac{102402}{292}\right)\cdot\left(\frac{273}{101325}\right) = 1.13 kgm^{-3} \quad [4]$$

Due to reduced model length from 1.8m to 1m, the volume of liquid to be blown have been reduced by a factor of 0.52 hence for the model, temperature correction factor of equation [1] is equal to 0.52*x*4.806 = 2.49

Considering equation [5], the blowing parameters under operational condition is given by:

$$Q_{model} = 2.49\cdot\sqrt{\left(\frac{\rho_l - \rho_g}{\rho_g}\right)_{model}}\cdot\sqrt{\left(\frac{\rho_g}{\rho_l - \rho_g}\right)_{ptype}}\cdot\sqrt[5]{\left(\frac{d_{model}}{d_{ptype}}\right)}\cdot Q_{ptype}$$

$$Q_{model} = 2.49\cdot\sqrt{\left(\frac{998-1.13}{1.13}\right)_{model}}\cdot\sqrt{\left(\frac{0.25}{4600-0.25}\right)_{ptype}}\cdot\sqrt[5]{\left(\frac{0.008}{0.041}\right)}\cdot Q_{ptype}$$

The above equation simplifies to:

$$Q_{model} = 0.0091_{Qptype}$$

Appendix A 2: Mixing time results-Physical modelling

Simulated Slag thickness (m)	Exp 1 T_{mix} (s)	Exp 2 T_{mix} (s)	Exp 3 T_{mix} (s)	Exp 4 T_{mix} (s)	Exp 5 T_{mix} (s)	Ave T_{mix} (s)	Std Dev
Air volumetric flow rate = 0.00875Nm^{3}s^{-1}							
0	87	77	80	79	87	82	4.69
0.027	81	89	97	88	79	87	7.16
0.054	95	101	96	99	93	97	3.19
0.081	89	87	85	93	79	87	5.18
0.108	79	102	83	81	93	88	9.69
Air volumetric flow rate = 0.0100Nm^{3}s^{-1}							
0	91	83	91	79	71	83	8.49
0.027	75	81	72	83	73	77	4.92
0.054	104	111	144	91	89	108	22.2
0.081	131	126	142	136	139	135	6.38
0.108	153	169	141	157	132	150	14.3
Air volumetric flow rate = 0.01125Nm^{3}s^{-1}							
0	58	47	51	56	43	51	6.20
0.027	68	61	54	63	71	63	6.58
0.054	74	77	83	78	82	79	3.70
0.081	123	107	112	129	119	118	8.72
0.108	167	171	162	177	163	168	6.16
Air volumetric flow rate = 0.01250Nm^{3}s^{-1}							
0	47	51	44	48	41	46	3.83
0.027	67	69	78	64	72	70	5.34
0.054	99	111	103	109	121	109	8.41
0.081	115	107	121	119	129	118	8.07
0.108	148	153	143	157	140	148	6.98
Air volumetric flow rate = 0.02375Nm^{3}s^{-1}							
0	52	55	61	59	48	55	5.24
0.027	68	61	54	63	71	63	6.58
0.054	113	107	119	127	116	116	7.40
0.081	124	127	131	117	121	124	5.39
0.108	173	179	201	184	173	182	11.57

Appendix A 3: Mixing efficiency calculated at different air volumetric flow rates and simulated slag thickness-Physical modelling

Air volumetric flow rate Q	Effective		Buoyancy specific power	Kinetic energy specific power	Mixing power ratio	Specific mixing power	Mixing time
	Tuyere submergence	Bath weight					
		W	ε_b	ε_k		ε_m	T_{mix}
Nm^3s^{-1}	m	kg	$kWton^{-1}$	$kWton^{-1}$	$\varepsilon_k/\varepsilon_b$	$kWton^{-1}$	S
Simulated slag thickness = 0mm							
0.00875	0.1100	135	0.139	0.024	0.18	0.163	82
0.01000	0.1100	135	0.159	0.036	0.23	0.195	83
0.01125	0.1100	135	0.179	0.052	0.29	0.230	51
0.01250	0.1100	135	0.198	0.071	0.36	0.269	46
0.01375	0.1100	135	0.218	0.094	0.43	0.313	55
Simulated slag thickness = 27mm							
0.00875	0.1370	149	0.156	0.022	0.14	0.178	87
0.01000	0.1370	149	0.179	0.033	0.18	0.211	77
0.01125	0.1370	149	0.201	0.047	0.23	0.248	63
0.01250	0.1370	149	0.223	0.064	0.29	0.287	70
0.01375	0.1370	149	0.245	0.085	0.35	0.331	63
Simulated slag thickness = 54mm							
0.00875	0.1640	164	0.170	0.020	0.12	0.191	97
0.01000	0.1640	164	0.195	0.030	0.15	0.225	108
0.01125	0.1640	164	0.219	0.043	0.19	0.262	79
0.01250	0.1640	164	0.244	0.059	0.24	0.302	109
0.01375	0.1640	164	0.268	0.078	0.29	0.346	116
Simulated slag thickness = 81mm							
0.00875	0.1910	178	0.182	0.018	0.10	0.201	87
0.01000	0.1910	178	0.208	0.028	0.13	0.236	135
0.01125	0.1910	178	0.234	0.039	0.17	0.274	118
0.01250	0.1910	178	0.261	0.054	0.21	0.314	118
0.01375	0.1910	178	0.287	0.072	0.25	0.358	124
Simulated slag thickness = 108mm							
0.00875	0.2180	192	0.192	0.017	0.09	0.209	88
0.01000	0.2180	192	0.220	0.025	0.12	0.245	150
0.01125	0.2180	192	0.247	0.036	0.15	0.283	168
0.01250	0.2180	192	0.275	0.050	0.18	0.324	148
0.01375	0.2180	192	0.302	0.066	0.22	0.368	182

Appendix A 4: Mass transfer results-Physical modelling

Sample 1 at simulated slag thickness, SS_t = 0mm								
Time	**Test 1**		**Test 2**		**Average Radius**	**Mass transfer coefficient**	**Sherwood number**	**Turbulent Characteristic**
	Weight	**Radius**	**Weight**	**Radius**				
s	**g**	**mm**	**g**	**mm**	**mm**	**($x10^{-5}ms^{-1}$)**		
Air volumetric flow rate = 0.00875Nm^3s^{-1}								
0	109.0078	19.05	108.7634	19.03	19.04	2.16	412	73
900	108.8734	19.04	106.7250	18.86	18.95			
1800	106.1239	18.81	106.6826	18.85	18.83			
2700	106.1789	18.81	106.1640	18.81	18.81			
3600	105.9287	18.79	105.9819	18.79	18.79			
Air volumetric flow rate = 0.01125Nm^3s^{-1}								
0	109.1298	19.06	108.6371	19.02	19.04	4.75	905	159
900	107.2893	18.91	107.6094	18.93	18.92			
1800	105.4357	18.75	104.1360	18.63	18.69			
2700	104.9814	18.71	104.1302	18.63	18.67			
3600	102.3218	18.47	102.6707	18.51	18.49			
Air volumetric flow rate = 0.01375Nm^3s^{-1}								
0	108.1892	18.98	108.2659	18.99	18.99	3.24	615	108
900	107.1986	18.90	107.4672	18.92	18.91			
1800	106.7842	18.86	107.4160	18.92	18.89			
2700	105.4519	18.75	105.9653	18.79	18.77			
3600	103.9912	18.62	103.7429	18.60	18.61			

Appendix A4: Mass transfer results-Physical modelling (Cont.)

Sample 1 at simulated slag thickness, SS_t =54mm								
Time	**Test 1**		**Test 2**		**Average Radius**	**Mass transfer coefficient**	**Sherwood number**	**Turbulent Characteristic**
	Weight	**Radius**	**Weight**	**Radius**				
s	**g**	**mm**	**g**	**mm**	**mm**	**($x10^{-5}ms^{-1}$)**		
Air volumetric flow rate = 0.00875Nm^3s^{-1}								
0	109.0125	19.05	108.5544	19.01	19.03	4.08	776	137
900	108.1387	18.98	106.2942	18.82	18.90			
1800	106.0548	18.80	105.1313	18.72	18.76			
2700	104.1739	18.64	105.1677	18.72	18.68			
3600	103.1964	18.55	103.3932	18.57	18.56			
Air volumetric flow rate = 0.01125Nm^3s^{-1}								
0	108.6719	19.02	108.4949	19.01	19.02	4.70	895	158
900	106.5475	18.84	107.1876	18.90	18.87			
1800	105.3387	18.74	104.9241	18.70	18.72			
2700	103.6518	18.59	104.0823	18.63	18.61			
3600	102.1396	18.46	102.3977	18.48	18.47			
Air volumetric flow rate = 0.01375Nm^3s^{-1}								
0	108.4154	19.00	108.5515	19.01	19.01	4.20	799	141
900	107.0168	18.88	107.1834	18.90	18.89			
1800	105.7417	18.77	105.2134	18.73	18.75			
2700	104.2372	18.64	104.4147	18.66	18.65			
3600	102.3891	18.48	103.2871	18.56	18.52			

Appendix A4: Mass transfer results-Physical modelling (Cont.)

Sample 1 at simulated slag thickness, SS_t =108mm								
Time	**Test 1**		**Test 2**		**Average Radius**	**Mass transfer coefficient**	**Sherwood number**	**Turbulent Characteristic**
	Weight	**Radius**	**Weight**	**Radius**				
s	**g**	**mm**	**g**	**mm**	**mm**	**($x10^{-5}ms^{-1}$)**		
Air volumetric flow rate = 0.00875Nm^3s^{-1}								
0	108.3067	18.99	108.7601	19.03	19.01	4.50	855	151
900	106.6868	18.85	107.0483	18.89	18.87			
1800	105.7489	18.77	105.2062	18.73	18.75			
2700	103.8926	18.61	104.0708	18.63	18.62			
3600	102.9463	18.53	102.0462	18.45	18.49			
Air volumetric flow rate = 0.01125Nm^3s^{-1}								
0	108.3111	18.99	108.6557	19.02	19.01	3.43	651	115
900	107.3128	18.91	107.3529	18.91	18.91			
1800	105.4967	18.75	106.3831	18.83	18.79			
2700	105.1016	18.72	104.9307	18.70	18.71			
3600	103.6871	18.59	104.0470	18.63	18.61			
Air volumetric flow rate = 0.01375Nm^3s^{-1}								
0	108.6111	19.02	108.6558	19.02	19.02	4.05	771	136
900	107.1246	18.89	107.3083	18.91	18.90			
1800	105.9503	18.79	105.2358	18.73	18.76			
2700	104.8555	18.70	104.2561	18.64	18.67			
3600	103.815	18.61	102.5461	18.49	18.55			

Appendix A4: Mass transfer results-Physical modelling (Cont.)

Sample 2 at simulated slag thickness, SS_t =0mm								
Time	**Test 1**		**Test 2**		**Average Radius**	**Mass transfer coefficient**	**Sherwood number**	**Turbulent Characteristic**
	Weight	**Radius**	**Weight**	**Radius**				
s	**g**	**mm**	**g**	**mm**	**mm**	**($x10^{-5}ms^{-1}$)**		
Air volumetric flow rate = 0.00875Nm^3s^{-1}								
0	108.2345	18.99	108.0451	18.97	18.98	7.65	1451	256
900	104.7654	18.69	104.5762	18.67	18.68			
1800	102.9234	18.53	102.9810	18.53	18.53			
2700	99.4432	18.22	99.4456	18.22	18.22			
3600	97.3453	18.03	98.6367	18.15	18.09			
Air volumetric flow rate = 0.01125Nm^3s^{-1}								
0	108.6729	19.02	107.5612	18.93	18.98	13.39	2541	448
900	105.7657	18.77	102.4271	18.48	18.63			
1800	99.0168	18.18	98.5278	18.14	18.16			
2700	96.1953	17.93	95.1350	17.83	17.88			
3600	89.9818	17.36	91.3488	17.48	17.42			
Air volumetric flow rate = 0.01375Nm^3s^{-1}								
0	108.1378	18.98	108.9819	19.05	19.02	11.40	2167	382
900	105.3789	18.74	104.6535	18.68	18.71			
1800	101.2348	18.38	102.1667	18.46	18.42			
2700	97.3219	18.03	98.6601	18.15	18.09			
3600	93.1237	17.65	94.0447	17.73	17.69			

Appendix A4: Mass transfer results-Physical modelling (Cont.)

Sample 2 at simulated slag thickness, SS_t =54mm								
Time	**Test 1**		**Test 2**		**Average Radius**	**Mass transfer coefficient**	**Sherwood number**	**Turbulent Characteristic**
	Weight	**Radius**	**Weight**	**Radius**				
s	**g**	**mm**	**g**	**mm**	**mm**	**($x10^{-5}ms^{-1}$)**		
Air volumetric flow rate = 0.00875Nm^3s^{-1}								
0	108.4187	19.00	108.8481	19.04	19.02	9.90	1883	332
900	105.1568	18.72	104.8755	18.70	18.71			
1800	101.8341	18.43	101.7943	18.43	18.43			
2700	98.9872	18.18	98.3337	18.12	18.15			
3600	96.2674	17.93	94.8427	17.81	17.87			
Air volumetric flow rate = 0.01125Nm^3s^{-1}								
0	108.3812	19.00	108.7856	19.03	19.02	14.25	2710	477
900	104.1874	18.64	103.3176	18.56	18.60			
1800	100.2658	18.29	97.5025	18.05	18.17			
2700	93.9237	17.72	95.2105	17.84	17.78			
3600	91.0154	17.45	89.0301	17.27	17.36			
Air volumetric flow rate = 0.01375Nm^3s^{-1}								
0	108.4168	19.00	108.9500	19.05	19.03	12.17	2316	408
900	104.1769	18.64	104.7048	18.68	18.66			
1800	100.1142	18.28	100.3484	18.30	18.29			
2700	96.5176	17.96	96.5783	17.96	17.96			
3600	92.7258	17.61	92.7035	17.61	17.61			

Appendix A4: Mass transfer results-Physical modelling (Cont.)

Sample 2 at simulated slag thickness, SS_t =108mm								
Time	**Test 1**		**Test 2**		**Average Radius**	**Mass transfer coefficient**	**Sherwood number**	**Turbulent Characteristic**
	Weight	**Radius**	**Weight**	**Radius**				
s	**g**	**mm**	**g**	**mm**	**mm**	**($x10^{-5}ms^{-1}$)**		
Air volumetric flow rate = 0.00875Nm^3s^{-1}								
0	108.3117	18.99	108.6551	19.02	19.01	10.31	1959	345
900	105.1096	18.72	104.9227	18.70	18.71			
1800	101.6351	18.41	101.0863	18.37	18.39			
2700	98.2355	18.11	98.4154	18.13	18.12			
3600	94.9895	17.82	94.8022	17.80	17.81			
Air volumetric flow rate = 0.01125Nm^3s^{-1}								
0	108.7612	19.03	108.5056	19.01	19.02	9.39	1785	314
900	105.6347	18.76	105.0895	18.72	18.74			
1800	102.6239	18.50	101.9134	18.44	18.47			
2700	99.2431	18.20	99.1971	18.20	18.20			
3600	96.1246	17.92	96.3082	17.94	17.93			
Air volumetric flow rate = 0.01375Nm^3s^{-1}-								
0	108.4412	19.00	108.6256	19.02	19.01	9.74	1852	326
900	105.4276	18.75	105.0659	18.71	18.73			
1800	101.1824	18.37	102.4460	18.49	18.43			
2700	98.8814	18.17	98.8869	18.17	18.17			
3600	95.7615	17.89	95.5687	17.87	17.88			

Appendix A4: Mass transfer results-Physical modelling (Cont.)

Sample 3 at simulated slag thickness, SS_t =0mm								
Time	**Test 1**		**Test 2**		**Average Radius**	**Mass transfer coefficient**	**Sherwood number**	**Turbulent Characteristic**
	Weight	**Radius**	**Weight**	**Radius**				
s	**g**	**mm**	**g**	**mm**	**mm**	**($x10^{-5}ms^{-1}$)**		
Air volumetric flow rate = 0.00875Nm^3s^{-1}								
0	109.1239	19.06	107.9169	18.96	19.01	5.09	967	170
900	105.4583	18.75	107.3482	18.91	18.83			
1800	104.1578	18.64	105.4139	18.74	18.69			
2700	103.1097	18.54	104.6245	18.68	18.61			
3600	100.9963	18.36	102.4052	18.48	18.42			
Air volumetric flow rate = 0.01125Nm^3s^{-1}								
0	109.5623	19.10	107.7046	18.94	19.02	9.47	1801	317
900	104.1908	18.64	105.1508	18.72	18.68			
1800	101.9056	18.44	103.5427	18.58	18.51			
2700	99.0178	18.18	100.0954	18.28	18.23			
3600	96.7845	17.98	95.4276	17.86	17.92			
Air volumetric flow rate = 0.01375Nm^3s^{-1}								
0	108.4761	19.01	108.0159	18.97	18.99	6.87	1304	230
900	106.1234	18.81	106.6831	18.85	18.83			
1800	103.8923	18.61	104.5300	18.67	18.64			
2700	101.9819	18.44	100.5131	18.32	18.38			
3600	98.2793	18.12	99.9368	18.26	18.19			

Appendix A4: Mass transfer results-Physical modelling (Cont.)

Sample 3 at simulated slag thickness, SS_t =54mm								
Time	**Test 1**		**Test 2**		**Average Radius**	**Mass transfer coefficient**	**Sherwood number**	**Turbulent Characteristic**
	Weight	**Radius**	**Weight**	**Radius**				
s	**g**	**mm**	**g**	**mm**	**mm**	**($x10^{-5}ms^{-1}$)**		
Air volumetric flow rate = 0.00875Nm^3s^{-1}								
0	108.9967	19.05	108.7701	19.03	19.04	7.16	1364	240
900	105.7845	18.78	106.7901	18.86	18.82			
1800	105.0147	18.71	102.2612	18.47	18.59			
2700	103.2759	18.56	99.4455	18.22	18.39			
3600	100.3489	18.30	98.3155	18.12	18.21			
Air volumetric flow rate = 0.01125Nm^3s^{-1}								
0	109.1671	19.07	108.5997	19.02	19.04	10.17	1937	341
900	108.0925	18.98	102.1703	18.46	18.72			
1800	103.4387	18.57	99.9627	18.27	18.42			
2700	100.5629	18.32	96.9816	18.00	18.16			
3600	94.0216	17.73	96.8684	17.99	17.86			
Air volumetric flow rate = 0.01375Nm^3s^{-1}								
0	107.9992	18.97	108.7677	19.03	19.00	7.74	1470	259
900	105.6715	18.77	105.9770	18.79	18.78			
1800	103.1672	18.55	102.9655	18.53	18.54			
2700	100.5619	18.32	100.8028	18.34	18.33			
3600	98.0156	18.09	98.1892	18.11	18.10			

Appendix A4: Mass transfer results-Physical modelling (Cont.)

Sample 3 at simulated slag thickness, SS_t =108mm								
Time	**Test 1**		**Test 2**		**Average Radius**	**Mass transfer coefficient**	**Sherwood number**	**Turbulent Characteristic**
	Weight	**Radius**	**Weight**	**Radius**				
s	**g**	**mm**	**g**	**mm**	**mm**	**($x10^{-5}ms^{-1}$)**		
Air volumetric flow rate = 0.00875Nm^3s^{-1}								
0	109.0012	19.05	108.7656	19.03	19.04	7.76	1478	260
900	105.4953	18.75	106.3845	18.83	18.79			
1800	103.9259	18.62	102.6637	18.50	18.56			
2700	101.2191	18.38	100.8233	18.34	18.36			
3600	98.4578	18.13	98.6396	18.15	18.14			
Air volumetric flow rate = 0.01125Nm^3s^{-1}								
0	108.5418	19.01	108.6251	19.02	19.02	6.51	1238	218
900	106.8275	18.87	105.7471	18.77	18.82			
1800	103.8952	18.61	104.0682	18.63	18.62			
2700	102.4019	18.48	101.6807	18.42	18.45			
3600	99.9873	18.27	99.8000	18.25	18.26			
Air volumetric flow rate = 0.01375Nm^3s^{-1}								
0	109.0012	19.05	107.7657	18.95	19.00	6.88	1307	230
900	106.7138	18.86	105.6291	18.76	18.81			
1800	103.4669	18.58	103.8091	18.60	18.59			
2700	101.9514	18.44	101.2233	18.38	18.41			
3600	99.3217	18.21	99.1185	18.19	18.20			

Appendix A4: Mass transfer results-Physical modelling (Cont.)

Sample 4 at simulated slag thickness, SS_t =0mm								
Time	**Test 1**		**Test 2**		**Average Radius**	**Mass transfer coefficient**	**Sherwood number**	**Turbulent Characteristic**
	Weight	**Radius**	**Weight**	**Radius**				
s	**g**	**mm**	**g**	**mm**	**mm**	**($x10^{-5}ms^{-1}$)**		
Air volumetric flow rate = 0.00875Nm^3s^{-1}								
0	109.0126	19.05	108.7543	19.03	19.04	2.60	496	87
900	108.7653	19.03	105.6676	18.77	18.90			
1800	106.9801	18.88	105.8264	18.78	18.83			
2700	106.5671	18.84	105.7758	18.78	18.81			
3600	105.4524	18.75	105.2718	18.73	18.74			
Air volumetric flow rate = 0.01125Nm^3s^{-1}								
0	108.0134	18.97	109.1923	19.07	19.02	5.92	1126	198
900	106.5672	18.84	107.6330	18.94	18.89			
1800	103.0156	18.54	104.7186	18.68	18.61			
2700	102.6781	18.51	103.4546	18.57	18.54			
3600	100.0672	18.28	101.2975	18.38	18.33			
Air volumetric flow rate = 0.01375Nm^3s^{-1}								
0	108.1675	18.98	108.2341	18.99	18.98	3.99	758	134
900	107.1091	18.89	106.8585	18.87	18.88			
1800	107.0178	18.88	106.4561	18.83	18.86			
2700	104.3129	18.65	105.2589	18.73	18.69			
3600	102.1234	18.46	103.5529	18.58	18.52			

Appendix A4: Mass transfer results-Physical modelling (Cont.)

Sample 4 at simulated slag thickness, SS_t =54mm								
Time	**Test 1**		**Test 2**		**Average Radius**	**Mass transfer coefficient**	**Sherwood number**	**Turbulent Characteristic**
	Weight	**Radius**	**Weight**	**Radius**				
s	**g**	**mm**	**g**	**mm**	**mm**	**($x10^{-5}ms^{-1}$)**		
Air volumetric flow rate = 0.00875Nm^3s^{-1}								
0	108.8878	19.04	108.7790	19.03	19.04	4.63	882	155
900	105.2349	18.73	108.5002	19.01	18.87			
1800	104.9812	18.71	105.7430	18.77	18.74			
2700	104.0273	18.62	104.1655	18.64	18.63			
3600	103.1276	18.55	102.0927	18.45	18.50			
Air volumetric flow rate = 0.01125Nm^3s^{-1}								
0	108.4106	19.00	108.6562	19.02	19.01	6.39	1215	214
900	106.4371	18.83	106.1375	18.81	18.82			
1800	103.4519	18.57	104.5115	18.67	18.62			
2700	102.7619	18.51	101.5480	18.41	18.46			
3600	99.9474	18.26	100.0649	18.28	18.27			
Air volumetric flow rate = 0.01375Nm^3s^{-1}								
0	108.3116	18.99	108.6552	19.02	19.01	4.98	946	167
900	106.5721	18.84	106.9307	18.88	18.86			
1800	104.8925	18.70	104.9095	18.70	18.70			
2700	103.2587	18.56	103.7883	18.60	18.58			
3600	101.1876	18.37	102.4408	18.49	18.43			

Appendix A4: Mass transfer results-Physical modelling (Cont.)

Sample 4 at simulated slag thickness, SS_t =108mm								
Time	**Test 1**		**Test 2**		**Average Radius**	**Mass transfer coefficient**	**Sherwood number**	**Turbulent Characteristic**
	Weight	**Radius**	**Weight**	**Radius**				
s	**g**	**mm**	**g**	**mm**	**mm**	**($x10^{-5}ms^{-1}$)**		
Air volumetric flow rate = 0.00875Nm^3s^{-1}								
0	109.0001	19.05	108.8667	19.04	19.05	5.31	1011	178
900	106.5713	18.84	106.9315	18.88	18.86			
1800	105.1056	18.72	104.9267	18.70	18.71			
2700	103.2538	18.56	103.7932	18.60	18.58			
3600	101.1852	18.37	102.4432	18.49	18.43			
Air volumetric flow rate = 0.01125Nm^3s^{-1}								
0	108.6614	19.02	108.6054	19.02	19.02	4.05	771	136
900	107.0916	18.89	107.1086	18.89	18.89			
1800	105.9573	18.79	105.2288	18.73	18.76			
2700	104.6616	18.68	104.4500	18.66	18.67			
3600	103.8191	18.61	102.5420	18.49	18.55			
Air volumetric flow rate = 0.01375Nm^3s^{-1}								
0	108.4981	19.01	108.7687	19.03	19.02	4.57	869	153
900	106.8927	18.87	107.0749	18.89	18.88			
1800	105.6349	18.76	105.0893	18.72	18.74			
2700	103.8952	18.61	104.0682	18.63	18.62			
3600	102.4517	18.49	102.5408	18.49	18.49			

Appendix A4: Mass transfer results-Physical modelling (Cont.)

Sample 5 at simulated slag thickness, SS_t =0mm								
Time	**Test 1**		**Test 2**		**Average Radius**	**Mass transfer coefficient**	**Sherwood number**	**Turbulent Characteristic**
	Weight	**Radius**	**Weight**	**Radius**				
s	**g**	**mm**	**g**	**mm**	**mm**	**($x10^{-5}ms^{-1}$)**		
Air volumetric flow rate = 0.00875Nm^3s^{-1}								
0	107.9673	18.96	108.1996	18.98	18.97	3.99	758	133
900	107.0978	18.89	107.1024	18.89	18.89			
1800	105.6791	18.77	104.3532	18.65	18.71			
2700	103.6793	18.59	104.2841	18.65	18.62			
3600	102.2378	18.47	103.2104	18.55	18.51			
Air volumetric flow rate = 0.01125Nm^3s^{-1}								
0	108.9807	19.05	108.7867	19.03	19.04	7.76	1478	260
900	106.0138	18.80	107.0247	18.88	18.84			
1800	102.1298	18.46	103.5465	18.58	18.52			
2700	101.0167	18.36	102.1580	18.46	18.41			
3600	98.9812	18.18	98.1163	18.10	18.14			
Air volumetric flow rate = 0.01375Nm^3s^{-1}								
0	106.9816	18.88	108.7613	19.03	18.96	4.87	923	162
900	106.7829	18.86	107.4173	18.92	18.89			
1800	105.3487	18.74	104.9142	18.70	18.72			
2700	102.6798	18.51	103.6813	18.59	18.55			
3600	101.0896	18.37	101.6318	18.41	18.39			

Appendix A4: Mass transfer results-Physical modelling (Cont.)

Sample 5 at simulated slag thickness, SS_t =54mm								
Time	**Test 1**		**Test 2**		**Average Radius**	**Mass transfer coefficient**	**Sherwood number**	**Turbulent Characteristic**
	Weight	**Radius**	**Weight**	**Radius**				
s	**g**	**mm**	**g**	**mm**	**mm**	**($x10^{-5}ms^{-1}$)**		
Air volumetric flow rate = 0.00875Nm^3s^{-1}								
0	108.4523	19.01	109.3142	19.08	19.04	6.47	1233	217
900	106.0094	18.80	106.7971	18.86	18.83			
1800	104.2387	18.64	103.7247	18.60	18.62			
2700	101.5409	18.41	102.7690	18.51	18.46			
3600	99.2653	18.20	101.1973	18.38	18.29			
Air volumetric flow rate = 0.01125Nm^3s^{-1}								
0	108.4287	19.00	108.6381	19.02	19.01	8.02	1525	269
900	106.6739	18.85	104.9745	18.71	18.78			
1800	101.4514	18.40	104.4530	18.66	18.53			
2700	100.8761	18.35	100.2628	18.29	18.32			
3600	97.1872	18.02	98.5720	18.14	18.08			
Air volumetric flow rate = 0.01375Nm^3s^{-1}								
0	108.0137	18.97	108.7532	19.03	19.00	6.02	1144	201
900	106.4519	18.83	106.3546	18.83	18.83			
1800	104.2271	18.64	104.1952	18.64	18.64			
2700	102.8325	18.52	101.9324	18.44	18.48			
3600	100.4379	18.31	100.2500	18.29	18.30			

Appendix A4: Mass transfer results-Physical modelling (Cont.)

Sample 5 at simulated slag thickness, SS_t =108mm								
Time	**Test 1**		**Test 2**		**Average Radius**	**Mass transfer coefficient**	**Sherwood number**	**Turbulent Characteristic**
	Weight	**Radius**	**Weight**	**Radius**				
s	**g**	**mm**	**g**	**mm**	**mm**	**($x10^{-5}ms^{-1}$)**		
Air volumetric flow rate = 0.00875Nm^3s^{-1}								
0	108.3213	18.99	108.6455	19.02	19.01	6.78	1289	227
900	106.1671	18.81	106.1758	18.81	18.81			
1800	103.5783	18.58	103.9267	18.62	18.60			
2700	101.0719	18.36	102.3295	18.48	18.42			
3600	99.5417	18.23	99.3470	18.21	18.22			
Air volumetric flow rate = 0.01125Nm^3s^{-1}								
0	108.5981	19.02	108.3687	19.00	19.01	5.75	1093	192
900	106.1559	18.81	106.8825	18.87	18.84			
1800	104.4481	18.66	104.4336	18.66	18.66			
2700	102.2784	18.47	103.1698	18.55	18.51			
3600	100.9725	18.36	100.6179	18.32	18.34			
Air volumetric flow rate = 0.01375Nm^3s^{-1}								
0	108.5321	19.01	108.2348	18.99	19.00	6.19	1176	207
900	106.4517	18.83	106.3548	18.83	18.83			
1800	104.1652	18.64	104.0276	18.62	18.63			
2700	102.7259	18.51	101.8114	18.43	18.47			
3600	100.2147	18.29	100.0227	18.27	18.28			

Appendix A4: Mass transfer results-Physical modelling (Cont.)

Sample 6 at simulated slag thickness, SS_t =0mm								
Time	**Test 1**		**Test 2**		**Average Radius**	**Mass transfer coefficient**	**Sherwood number**	**Turbulent Characteristic**
	Weight	**Radius**	**Weight**	**Radius**				
s	**g**	**mm**	**g**	**mm**	**mm**	**($x10^{-5}ms^{-1}$)**		
Air volumetric flow rate = 0.00875Nm^3s^{-1}								
0	108.5678	19.02	108.8991	19.04	19.03	7.82	1489	262
900	105.1908	18.73	104.3810	18.65	18.69			
1800	103.1769	18.55	102.2713	18.47	18.51			
2700	102.9804	18.53	100.8750	18.35	18.44			
3600	97.9871	18.09	98.6638	18.15	18.12			
Air volumetric flow rate = 0.01125Nm^3s^{-1}								
0	107.7451	18.95	108.0218	18.97	18.96	11.93	2262	398
900	106.0167	18.80	104.0157	18.62	18.71			
1800	98.7892	18.16	102.5755	18.50	18.33			
2700	95.3479	17.85	97.7480	18.07	17.96			
3600	91.6458	17.51	92.9170	17.63	17.57			
Air volumetric flow rate = 0.01375Nm^3s^{-1}								
0	107.9548	18.96	107.9562	18.96	18.96	9.92	1881	331
900	105.1298	18.72	106.2874	18.82	18.77			
1800	102.8921	18.52	101.8728	18.44	18.48			
2700	99.6792	18.24	98.5369	18.14	18.19			
3600	94.1873	17.75	95.6045	17.87	17.81			

Appendix A4: Mass transfer results-Physical modelling (Cont.)

Sample 6 at simulated slag thickness, SS_t =54mm								
Time	**Test 1**		**Test 2**		**Average Radius**	**Mass transfer coefficient**	**Sherwood number**	**Turbulent Characteristic**
	Weight	**Radius**	**Weight**	**Radius**				
s	**g**	**mm**	**g**	**mm**	**mm**	**($x10^{-5}ms^{-1}$)**		
Air volumetric flow rate = 0.00875Nm^3s^{-1}								
0	108.3834	19.00	108.7834	19.03	19.02	9.69	1843	325
900	106.2129	18.81	103.5891	18.59	18.70			
1800	102.0023	18.45	102.7625	18.51	18.48			
2700	98.9127	18.17	99.3034	18.21	18.19			
3600	96.5615	17.96	94.9890	17.82	17.89			
Air volumetric flow rate = 0.01125Nm^3s^{-1}								
0	108.2012	18.98	108.7656	19.03	19.01	12.89	2450	431
900	106.9723	18.88	101.2205	18.38	18.63			
1800	101.7821	18.43	97.5557	18.05	18.24			
2700	94.5476	17.78	97.0029	18.00	17.89			
3600	91.0217	17.45	92.2449	17.57	17.51			
Air volumetric flow rate = 0.01375Nm^3s^{-1}								
0	108.4219	19.00	108.4451	19.01	19.00	11.05	2099	370
900	104.7952	18.69	104.7765	18.69	18.69			
1800	100.2518	18.29	101.5646	18.41	18.35			
2700	97.3417	18.03	97.7500	18.07	18.05			
3600	93.2198	17.66	94.6027	17.78	17.72			

Appendix A4: Mass transfer results-Physical modelling (Cont.)

Sample 6 at simulated slag thickness, SS_t =108mm								
Time	**Test 1**		**Test 2**		**Average Radius**	**Mass transfer coefficient**	**Sherwood number**	**Turbulent Characteristic**
	Weight	**Radius**	**Weight**	**Radius**				
s	**g**	**mm**	**g**	**mm**	**mm**	**($x10^{-5}ms^{-1}$)**		
Air volumetric flow rate = 0.00875Nm^3s^{-1}								
0	108.8363	19.04	108.6305	19.02	19.03	10.32	1964	346
900	105.1096	18.72	104.9227	18.70	18.71			
1800	101.7444	18.42	101.2035	18.38	18.40			
2700	98.3417	18.12	98.5324	18.14	18.13			
3600	95.1018	17.83	95.1289	17.83	17.83			
Air volumetric flow rate = 0.01125Nm^3s^{-1}								
0	108.3916	19.00	108.5752	19.02	19.01	9.10	1730	305
900	105.6392	18.76	105.0850	18.72	18.74			
1800	102.5185	18.49	101.7914	18.43	18.46			
2700	99.6542	18.24	99.2345	18.20	18.22			
3600	96.3447	17.94	96.5300	17.96	17.95			
Air volumetric flow rate = 0.01375Nm^3s^{-1}								
0	108.3419	19.00	108.4249	19.00	19.00	9.55	1814	319
900	105.5248	18.75	104.9687	18.71	18.73			
1800	101.1854	18.37	102.4430	18.49	18.43			
2700	98.9767	18.18	99.0154	18.18	18.18			
3600	95.6716	17.88	95.8789	17.90	17.89			

Appendix A4: Mass transfer results-Physical modelling (Cont.)

Sample 7 at simulated slag thickness, SS_t =0mm								
Time	**Test 1**		**Test 2**		**Average Radius**	**Mass transfer coefficient**	**Sherwood number**	**Turbulent Characteristic**
	Weight	**Radius**	**Weight**	**Radius**				
s	**g**	**mm**	**g**	**mm**	**mm**	**($x10^{-5}ms^{-1}$)**		
Air volumetric flow rate = 0.00875Nm^3s^{-1}								
0	109.1921	19.07	107.8747	18.96	19.01	1.14	217	38
900	108.9149	19.05	107.3842	18.91	18.98			
1800	108.8341	19.04	106.2977	18.82	18.93			
2700	108.4918	19.01	106.1739	18.81	18.91			
3600	107.9981	18.97	105.9695	18.79	18.88			
Air volumetric flow rate = 0.01125Nm^3s^{-1}								
0	107.8917	18.96	108.6128	19.02	18.99	1.11	210	37
900	106.9145	18.87	108.4505	19.01	18.94			
1800	106.6213	18.85	108.0445	18.97	18.91			
2700	106.4127	18.83	107.5549	18.93	18.88			
3600	106.3219	18.82	107.1809	18.90	18.86			
Air volumetric flow rate = 0.01375Nm^3s^{-1}								
0	108.9197	19.05	108.1981	18.98	19.01	0.82	155	27
900	107.8342	18.95	107.9976	18.97	18.96			
1800	107.6941	18.94	107.9043	18.96	18.95			
2700	107.6704	18.94	107.6947	18.94	18.94			
3600	107.2389	18.90	107.6598	18.94	18.92			

Appendix A4: Mass transfer results-Physical modelling (Cont.)

Sample 7 at simulated slag thickness, SS_t =54mm								
Time	**Test 1**		**Test 2**		**Average Radius**	**Mass transfer coefficient**	**Sherwood number**	**Turbulent Characteristic**
	Weight	**Radius**	**Weight**	**Radius**				
s	**g**	**mm**	**g**	**mm**	**mm**	**($x10^{-5}ms^{-1}$)**		
Air volumetric flow rate = 0.00875Nm^3s^{-1}								
0	108.7819	19.03	109.4152	19.09	19.06	3.53	674	119
900	106.2874	18.82	108.6113	19.02	18.92			
1800	105.9816	18.79	106.3613	18.83	18.81			
2700	105.0751	18.72	105.6491	18.76	18.74			
3600	104.7659	18.69	103.8860	18.61	18.65			
Air volumetric flow rate = 0.01125Nm^3s^{-1}								
0	108.8236	19.04	108.9433	19.05	19.04	2.43	463	82
900	107.7899	18.95	107.8084	18.95	18.95			
1800	106.8672	18.87	106.8679	18.87	18.87			
2700	106.4037	18.83	106.4028	18.83	18.83			
3600	105.5939	18.76	105.5922	18.76	18.76			
Air volumetric flow rate = 0.01375Nm^3s^{-1}								
0	108.8373	19.04	108.6296	19.02	19.03	1.72	327	58
900	107.9986	18.97	107.8332	18.95	18.96			
1800	107.2167	18.90	107.2162	18.90	18.90			
2700	106.9826	18.88	106.9850	18.88	18.88			
3600	106.4021	18.83	106.4044	18.83	18.83			

Appendix A4: Mass transfer results-Physical modelling (Cont.)

Sample 7 at simulated slag thickness, SS_t =108mm								
Time	**Test 1**		**Test 2**		**Average Radius**	**Mass transfer coefficient**	**Sherwood number**	**Turbulent Characteristic**
	Weight	**Radius**	**Weight**	**Radius**				
s	**g**	**mm**	**g**	**mm**	**mm**	**($x10^{-5}ms^{-1}$)**		
Air volumetric flow rate = 0.00875Nm^3s^{-1}								
0	108.5423	19.01	108.6245	19.02	19.02	3.76	715	126
900	107.1276	18.89	107.0726	18.89	18.89			
1800	105.2854	18.73	106.3630	18.83	18.78			
2700	104.8762	18.70	104.6955	18.68	18.69			
3600	103.2549	18.56	103.7921	18.60	18.58			
Air volumetric flow rate = 0.01125Nm^3s^{-1}								
0	108.7165	19.03	108.5504	19.01	19.02	2.68	509	90
900	107.6562	18.94	107.4756	18.92	18.93			
1800	106.1592	18.81	106.8793	18.87	18.84			
2700	105.4951	18.75	106.3847	18.83	18.79			
3600	105.1016	18.72	104.9308	18.70	18.71			
Air volumetric flow rate = 0.01375Nm^3s^{-1}								
0	108.4319	19.00	108.5247	19.01	19.01	3.08	585	103
900	107.6516	18.94	107.4802	18.92	18.93			
1800	106.7181	18.86	105.6248	18.76	18.81			
2700	105.6372	18.76	105.0870	18.72	18.74			
3600	104.2386	18.64	104.4133	18.66	18.65			

Appendix A4: Mass transfer results-Physical modelling (Cont.)

Sample 8 at simulated slag thickness, SS_t =0mm								
Time	Test 1		Test 2		Average Radius	Mass transfer coefficient	Sherwood number	Turbulent Characteristic
	Weight	Radius	Weight	Radius				
s	g	mm	g	mm	mm	($x10^{-5}ms^{-1}$)		
Air volumetric flow rate = 0.00875Nm^3s^{-1}								
0	107.6983	18.94	108.6685	19.02	18.98	1.53	290	51
900	107.5418	18.93	108.5236	19.01	18.97			
1800	107.3498	18.91	107.5489	18.93	18.92			
2700	107.0902	18.89	105.2527	18.73	18.81			
3600	106.9919	18.88	105.2491	18.73	18.81			
Air volumetric flow rate = 0.01125Nm^3s^{-1}								
0	108.1235	18.98	108.2481	18.99	18.98	3.38	642	113
900	107.9012	18.96	106.2990	18.82	18.89			
1800	105.0123	18.71	106.1738	18.81	18.76			
2700	105.3906	18.74	105.3337	18.74	18.74			
3600	104.0017	18.62	103.2743	18.56	18.59			
Air volumetric flow rate = 0.01375Nm^3s^{-1}								
0	107.8721	18.96	108.1783	18.98	18.97	2.23	423	75
900	107.4389	18.92	107.6929	18.94	18.93			
1800	107.1798	18.90	107.4317	18.92	18.91			
2700	106.6719	18.85	105.5679	18.76	18.81			
3600	105.1892	18.73	104.8432	18.69	18.71			

Appendix A4: Mass transfer results-Physical modelling (Cont.)

Sample 8 at simulated slag thickness, SS_t =54mm								
Time	**Test 1**		**Test 2**		**Average Radius**	**Mass transfer coefficient**	**Sherwood number**	**Turbulent Characteristic**
	Weight	**Radius**	**Weight**	**Radius**				
s	**g**	**mm**	**g**	**mm**	**mm**	**($x10^{-5}ms^{-1}$)**		
Air volumetric flow rate = 0.00875Nm^3s^{-1}								
0	108.5879	19.02	108.5789	19.02	19.02	3.76	715	126
900	107.6528	18.94	106.7801	18.86	18.90			
1800	106.0644	18.80	105.5840	18.76	18.78			
2700	105.0253	18.71	104.5464	18.67	18.69			
3600	103.9981	18.62	103.0489	18.54	18.58			
Air volumetric flow rate = 0.01125Nm^3s^{-1}								
0	108.4276	19.00	108.5392	19.01	19.01	4.29	815	144
900	107.0912	18.89	107.1090	18.89	18.89			
1800	105.3561	18.74	105.3681	18.74	18.74			
2700	104.2486	18.64	104.1737	18.64	18.64			
3600	102.6389	18.50	102.8093	18.52	18.51			
Air volumetric flow rate = 0.01375Nm^3s^{-1}								
0	108.4991	19.01	108.7677	19.03	19.02	3.45	657	116
900	107.3327	18.91	107.3330	18.91	18.91			
1800	106.5076	18.84	105.6037	18.76	18.80			
2700	105.3141	18.74	104.9487	18.70	18.72			
3600	103.8971	18.61	104.0663	18.63	18.62			

Appendix A4: Mass transfer results-Physical modelling (Cont.)

Sample 8 at simulated slag thickness, SS_t =108mm								
Time	**Test 1**		**Test 2**		**Average Radius**	**Mass transfer coefficient**	**Sherwood number**	**Turbulent Characteristic**
	Weight	**Radius**	**Weight**	**Radius**				
s	**g**	**mm**	**g**	**mm**	**mm**	**($x10^{-5}ms^{-1}$)**		
Air volumetric flow rate = 0.00875Nm^3s^{-1}								
0	108.2167	18.99	108.5501	19.01	19.00	4.21	801	141
900	106.8945	18.87	107.0731	18.89	18.88			
1800	105.9531	18.79	105.2330	18.73	18.76			
2700	104.1216	18.63	104.3007	18.65	18.64			
3600	102.2749	18.47	103.1733	18.55	18.51			
Air volumetric flow rate = 0.01125Nm^3s^{-1}								
0	108.3388	19.00	108.6280	19.02	19.01	3.26	619	109
900	107.4313	18.92	107.2344	18.90	18.91			
1800	106.7131	18.86	105.6298	18.76	18.81			
2700	105.3161	18.74	104.9467	18.70	18.72			
3600	104.9016	18.70	103.2912	18.56	18.63			
Air volumetric flow rate = 0.01375Nm^3s^{-1}								
0	108.5618	19.02	108.3050	18.99	19.00	3.73	710	125
900	107.0017	18.88	107.1985	18.90	18.89			
1800	105.0768	18.72	106.3404	18.82	18.77			
2700	104.8786	18.70	104.6931	18.68	18.69			
3600	103.0419	18.54	103.7764	18.60	18.57			

Appendix A 5: Numerical simulation results

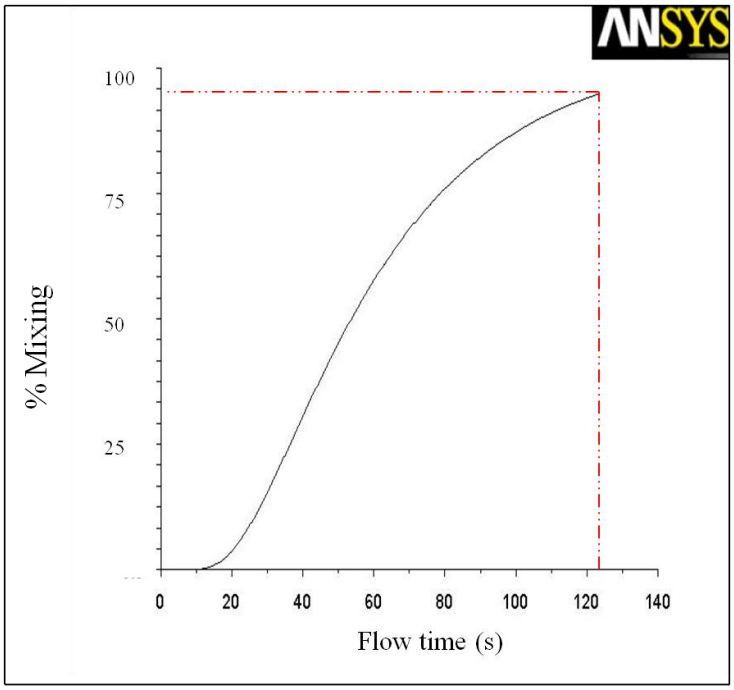

Graph A1: Numerical mixing time graph for 81mm simulated slag thickness at air volumetric flow rate of 0.01125Nm^3s^{-1}.

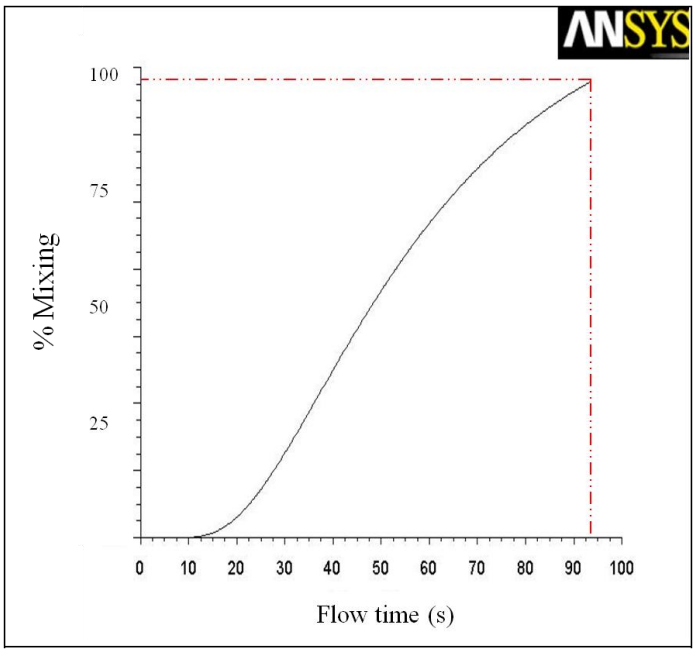

Graph A2: Numerical mixing time graph for 54mm simulated slag thickness at air volumetric flow rate of 0.01125Nm^3s^{-1}.

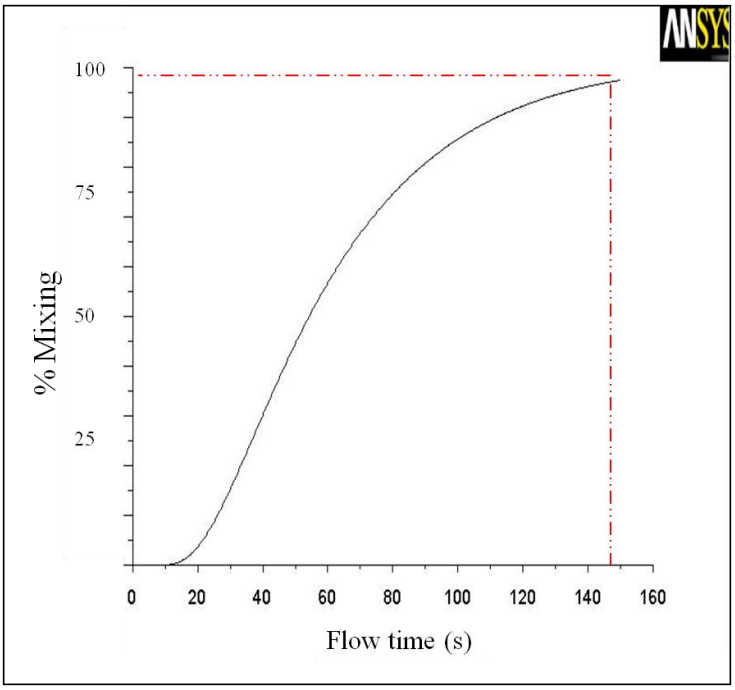

Graph A3: Numerical mixing time graph for 324mm simulated matte at air volumetric flow rate of 0.01125Nm^3s^{-1}.

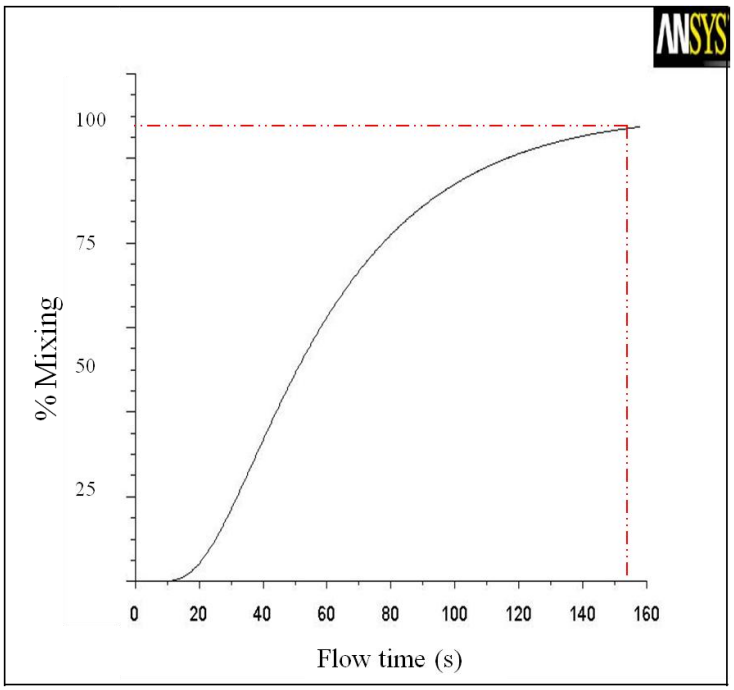

Graph A4: Numerical mixing time graph for 378mm simulated matte at air volumetric flow rate of 0.01125Nm^3s^{-1}.

Appendix A 6: Mass transfer results

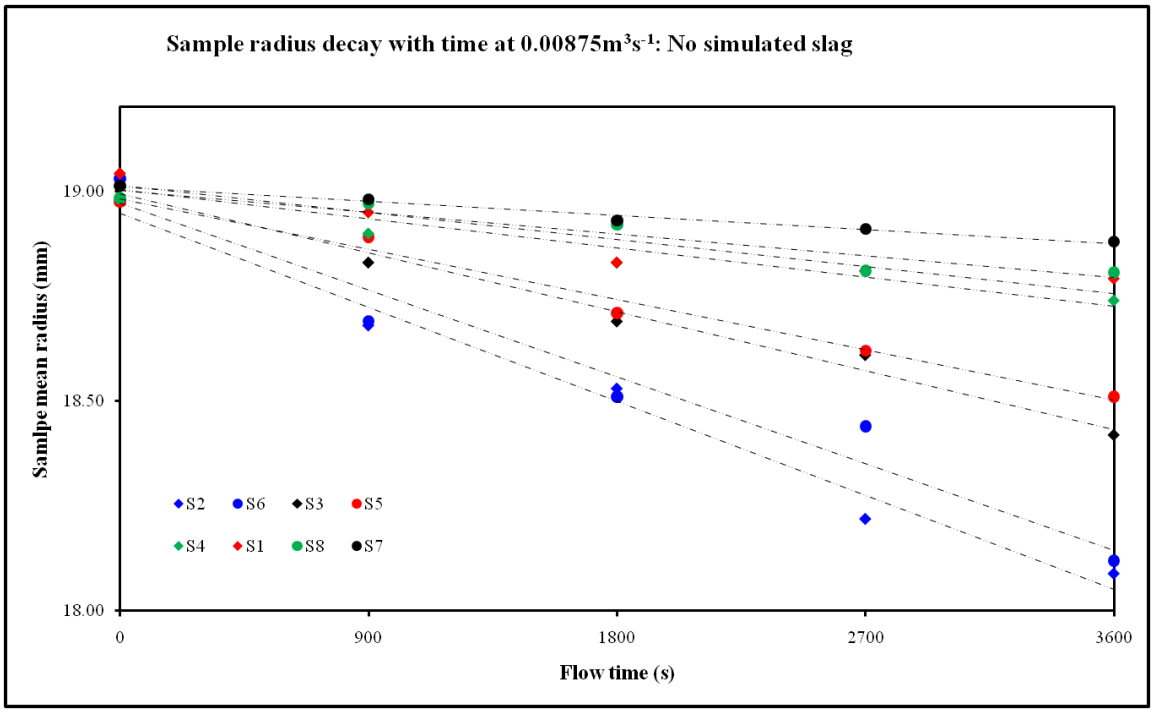

Figure A6 (a): Sample radius decay with time at 0.00875Nm^3s^{-1} with no simulated slag

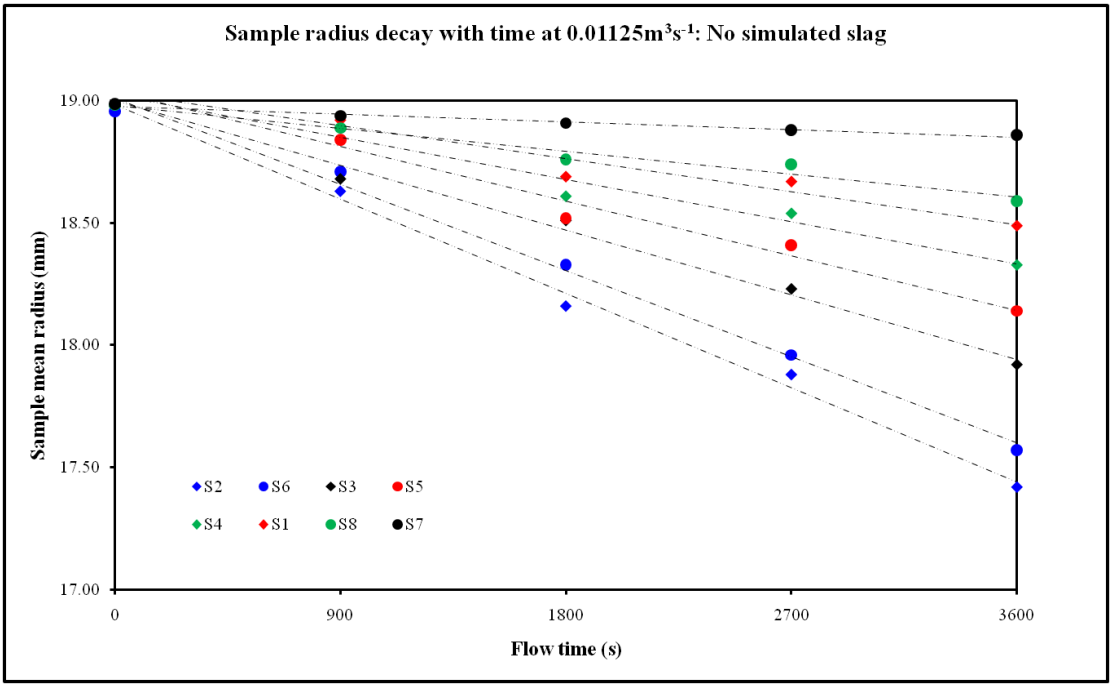

Figure A6 (b): Sample radius decay with time at 0.01125Nm^3s^{-1} with no simulated slag

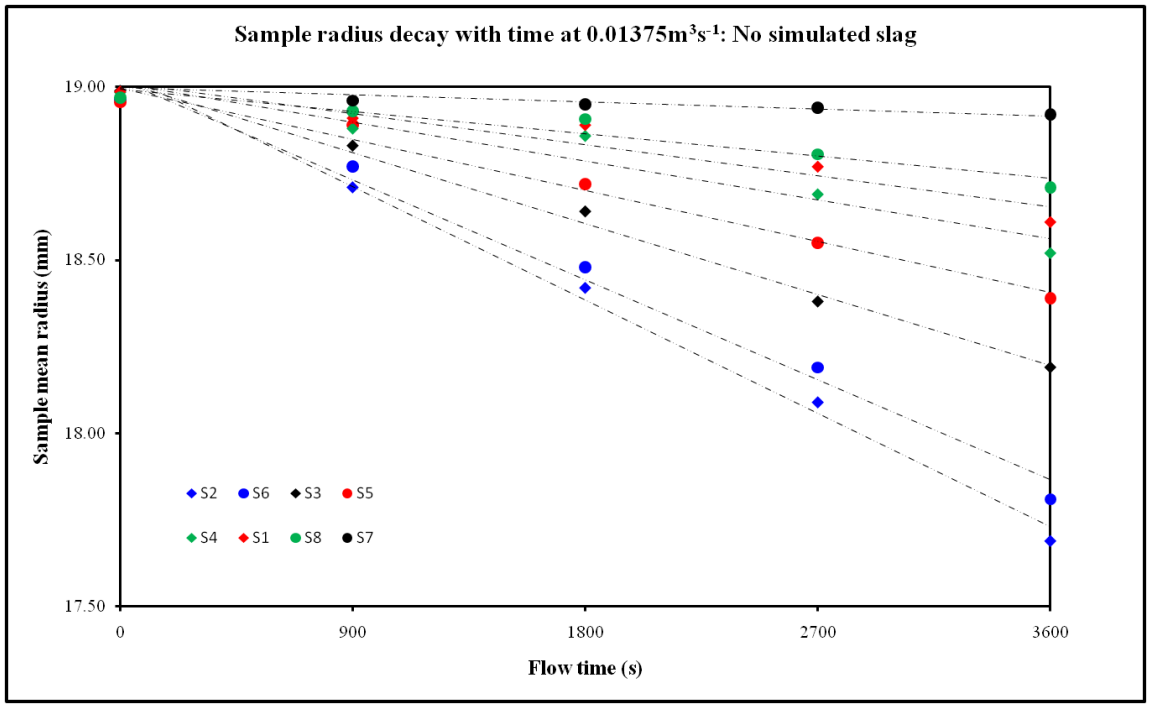

Figure A6 (c): Sample radius decay with time at 0.01375Nm^{3}s^{-1} with no simulated slag

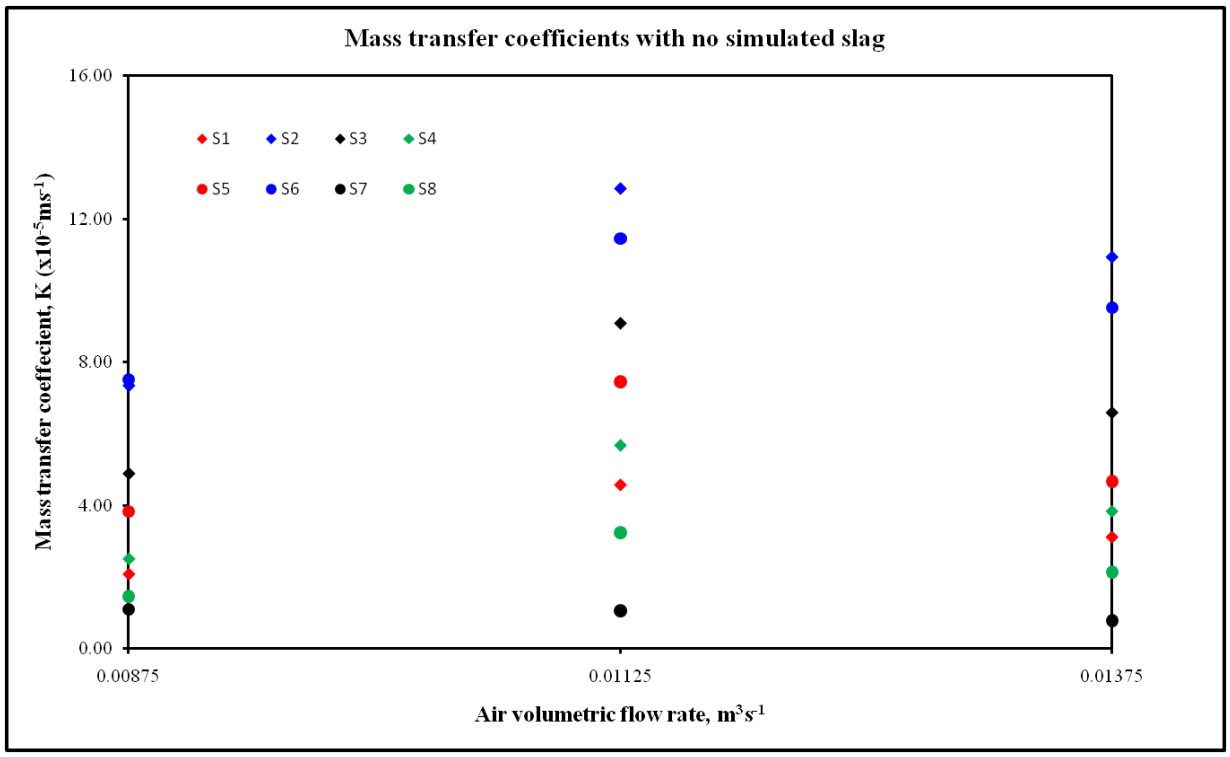

Figure A6 (d): Mass transfer coefficients with no simulated slag

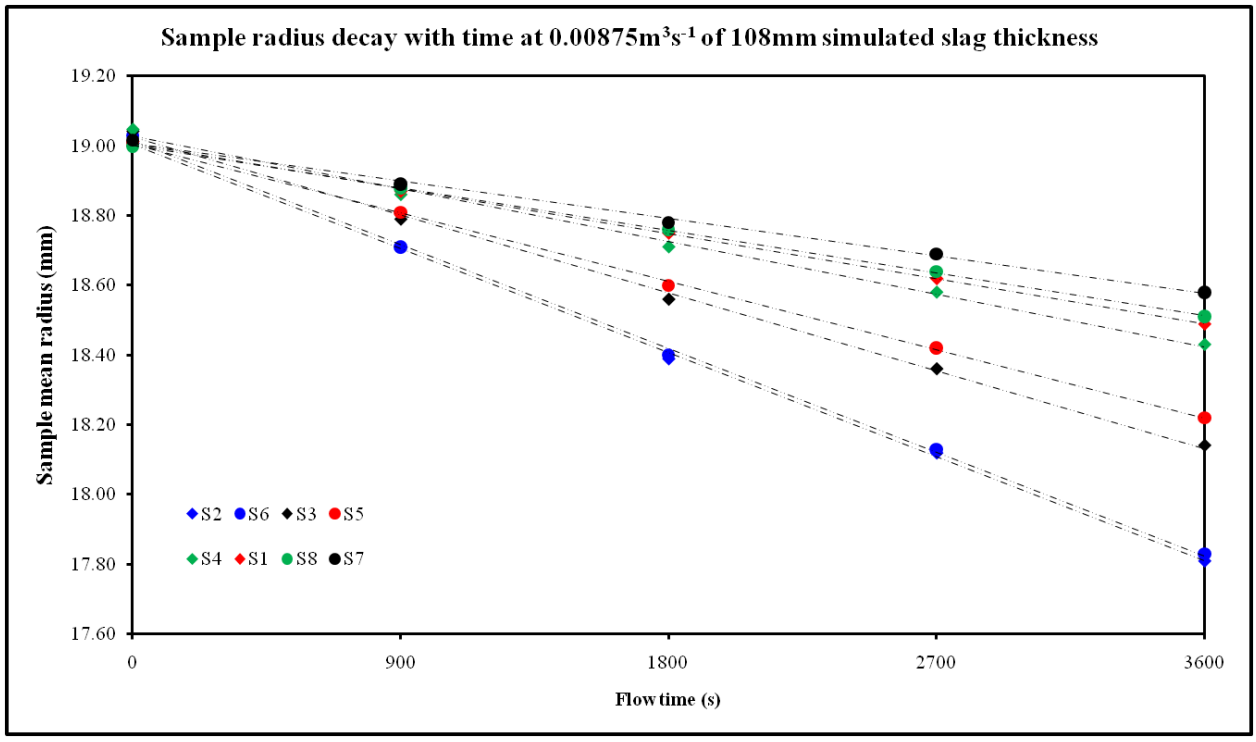

Figure A6 (e): Sample radius decay with time at 0.00875Nm^{3}s^{-1} with 108mm simulated slag thickness

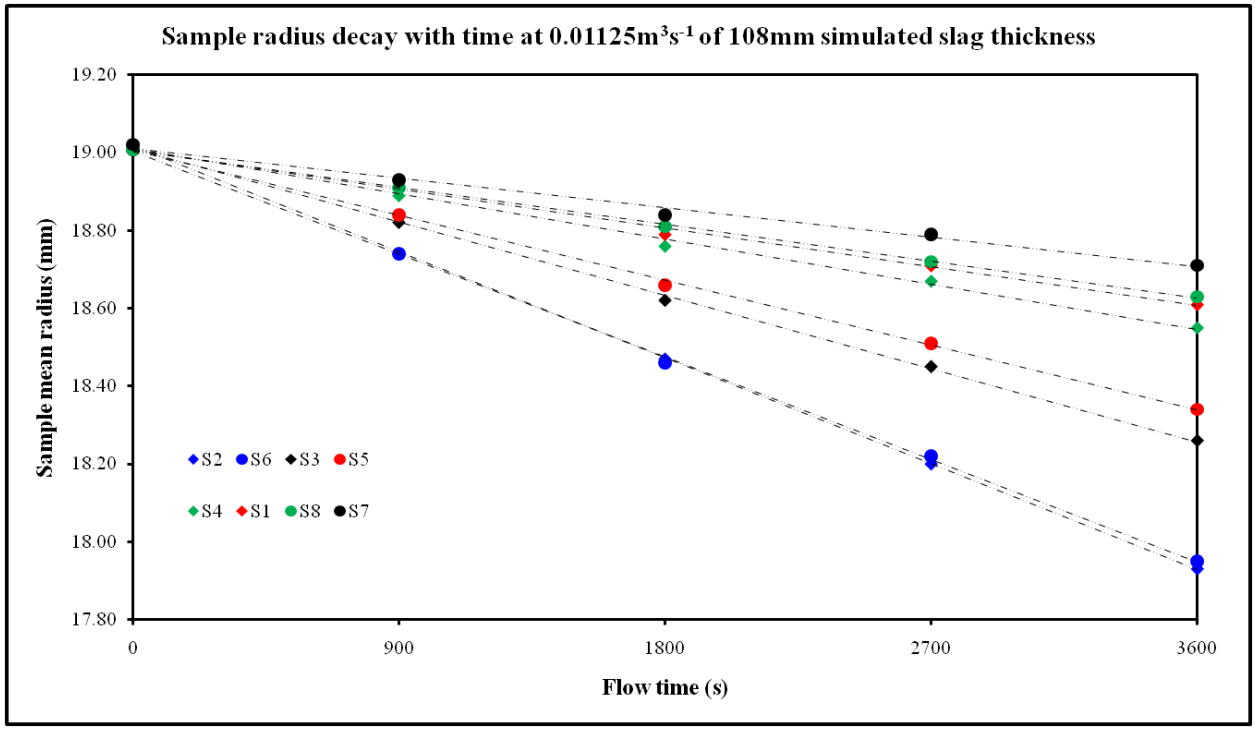

Figure A6 (f): Sample radius decay with time at 0.01125Nm^{3}s^{-1} with 108mm simulated slag thickness

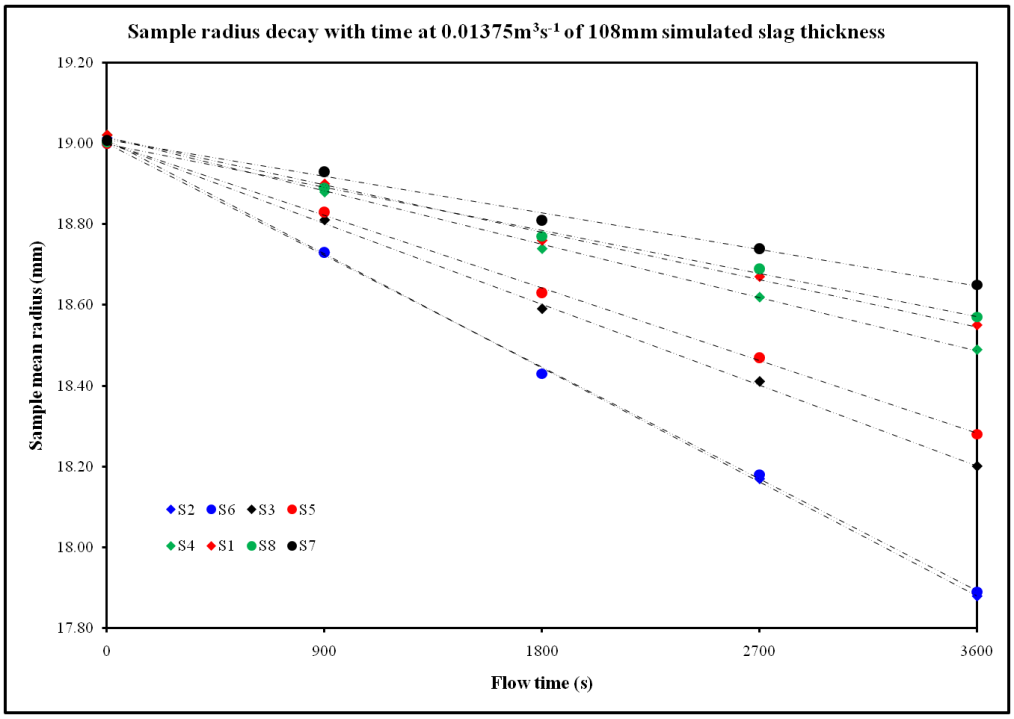

Figure A6 (g): Sample radius decay with time at 0.01375Nm^3s^{-1} with 108mm simulated slag thickness

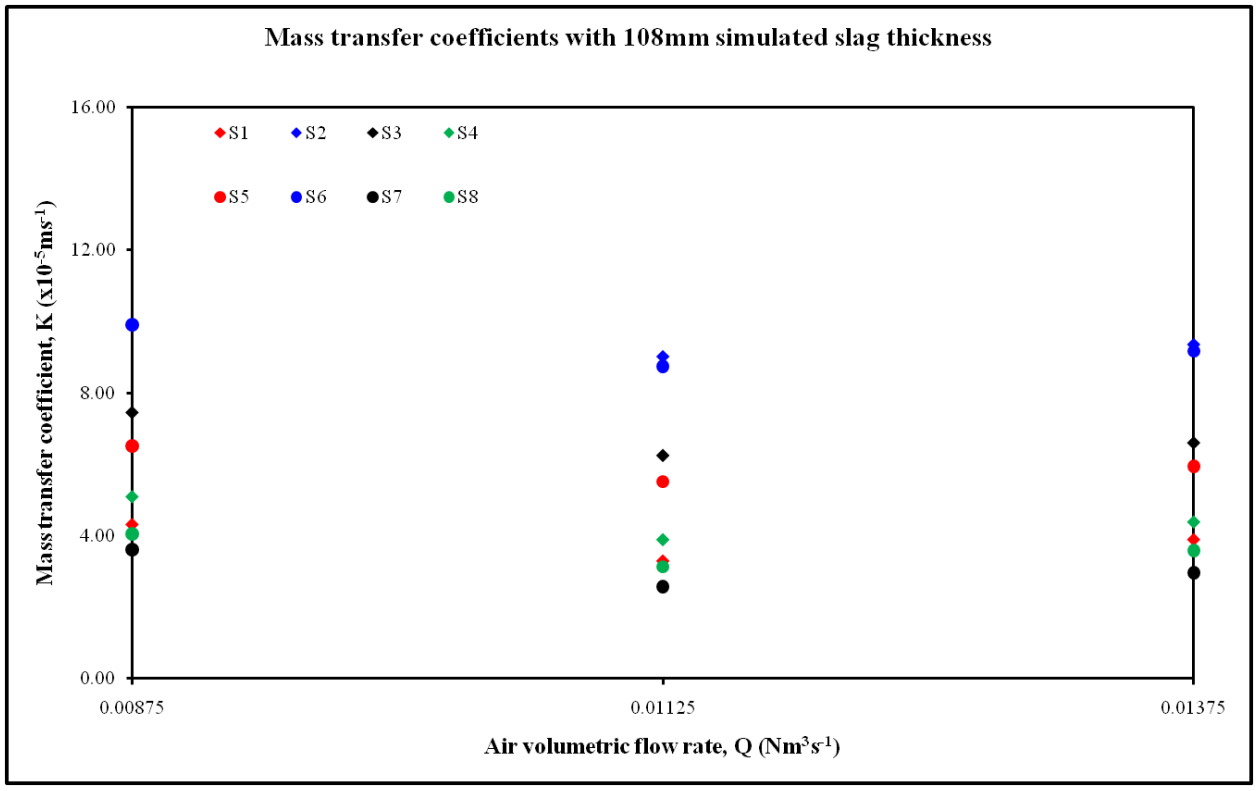

Figure A6 (h): Mass transfer coefficients with 108mm simulated slag thickness

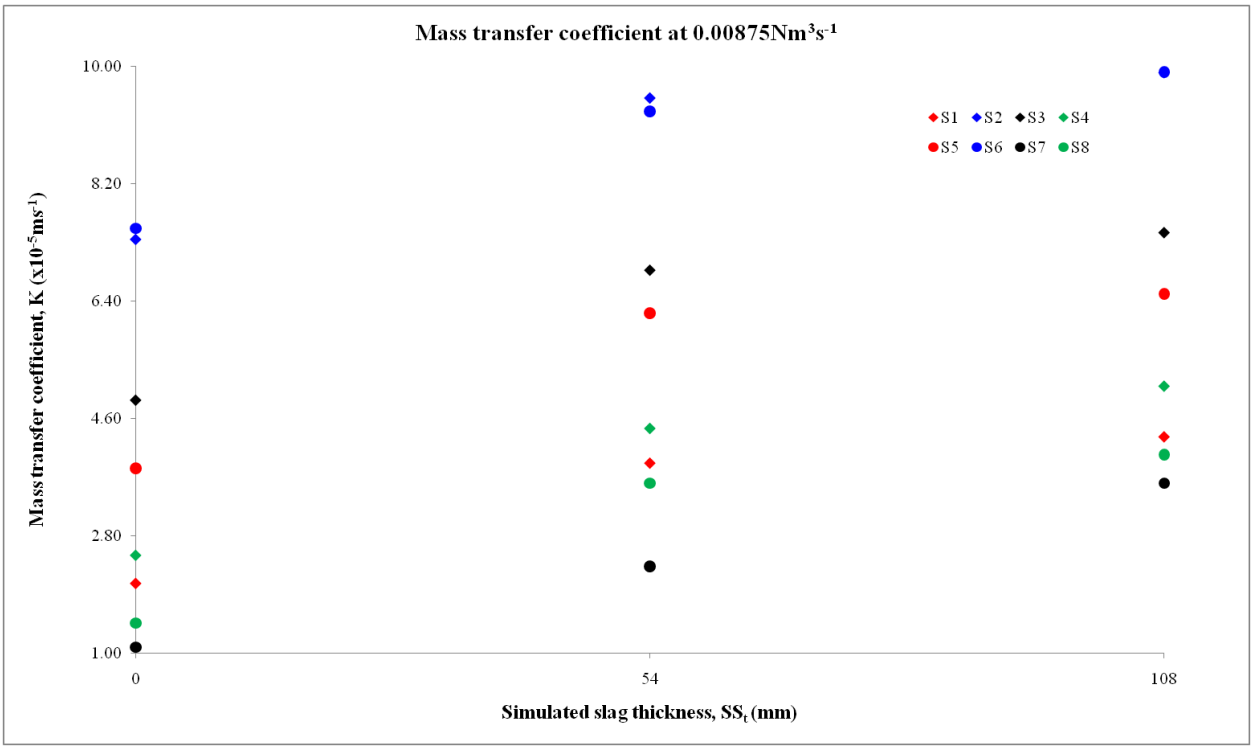

Figure A6 (i): Mass transfer coefficients at air volumetric flow rate of 0.00875Nm^3s^{-1} as a function of slag thickness

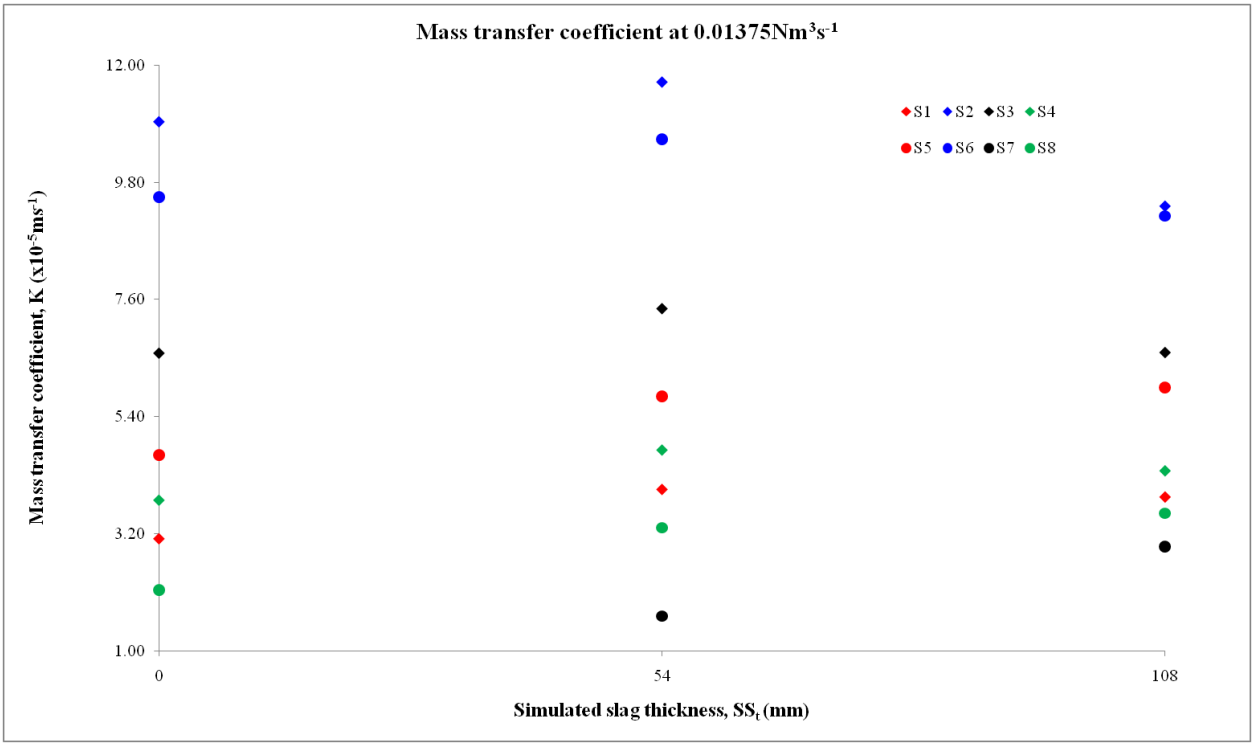

Figure A6 (j): Mass transfer coefficients at air volumetric flow rate of 0.01375Nm^3s^{-1} as a function of slag thickness

Appendix A 7: Mixing time and mass transfer results comparison

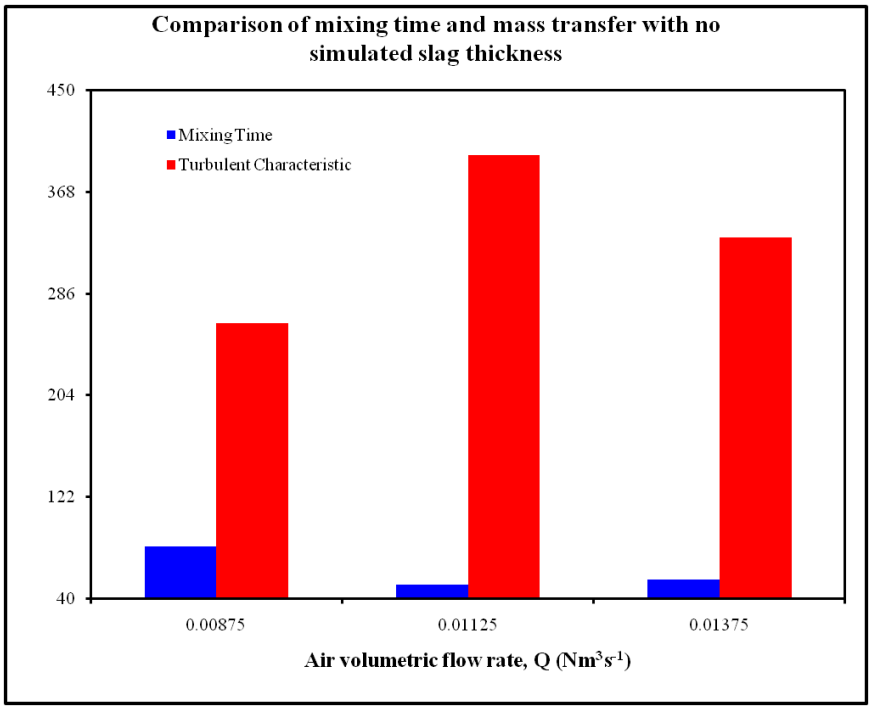

Figure A7 (a): Mixing time and mass transfer comparison with no slag simulated.

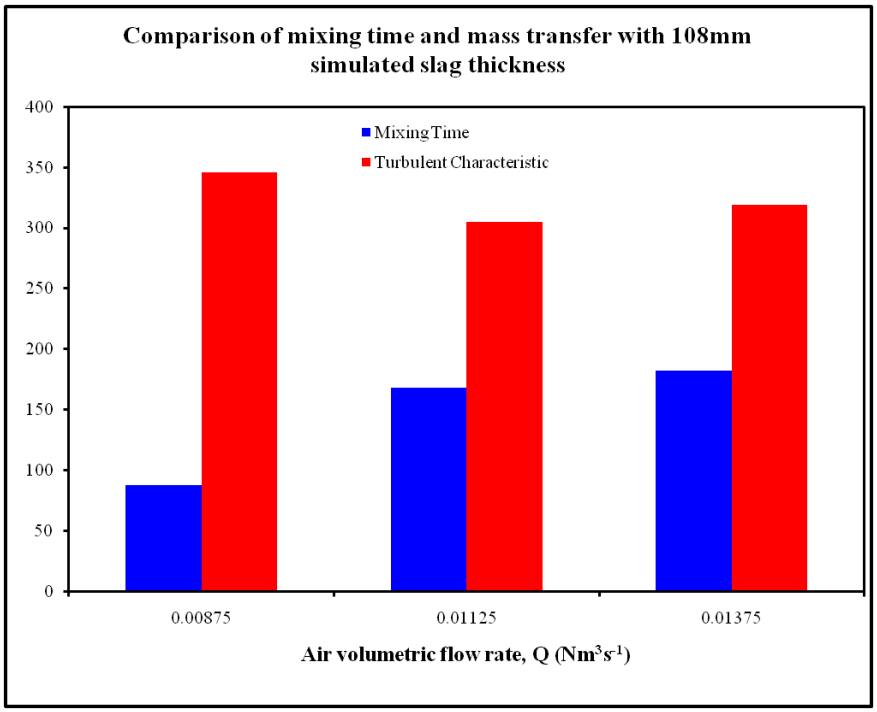

Figure A7 (b): Mixing time and mass transfer comparison with 108mm simulated slag thickness.

Appendix A 8: Laboratory produced sintered benzoic acid compacts

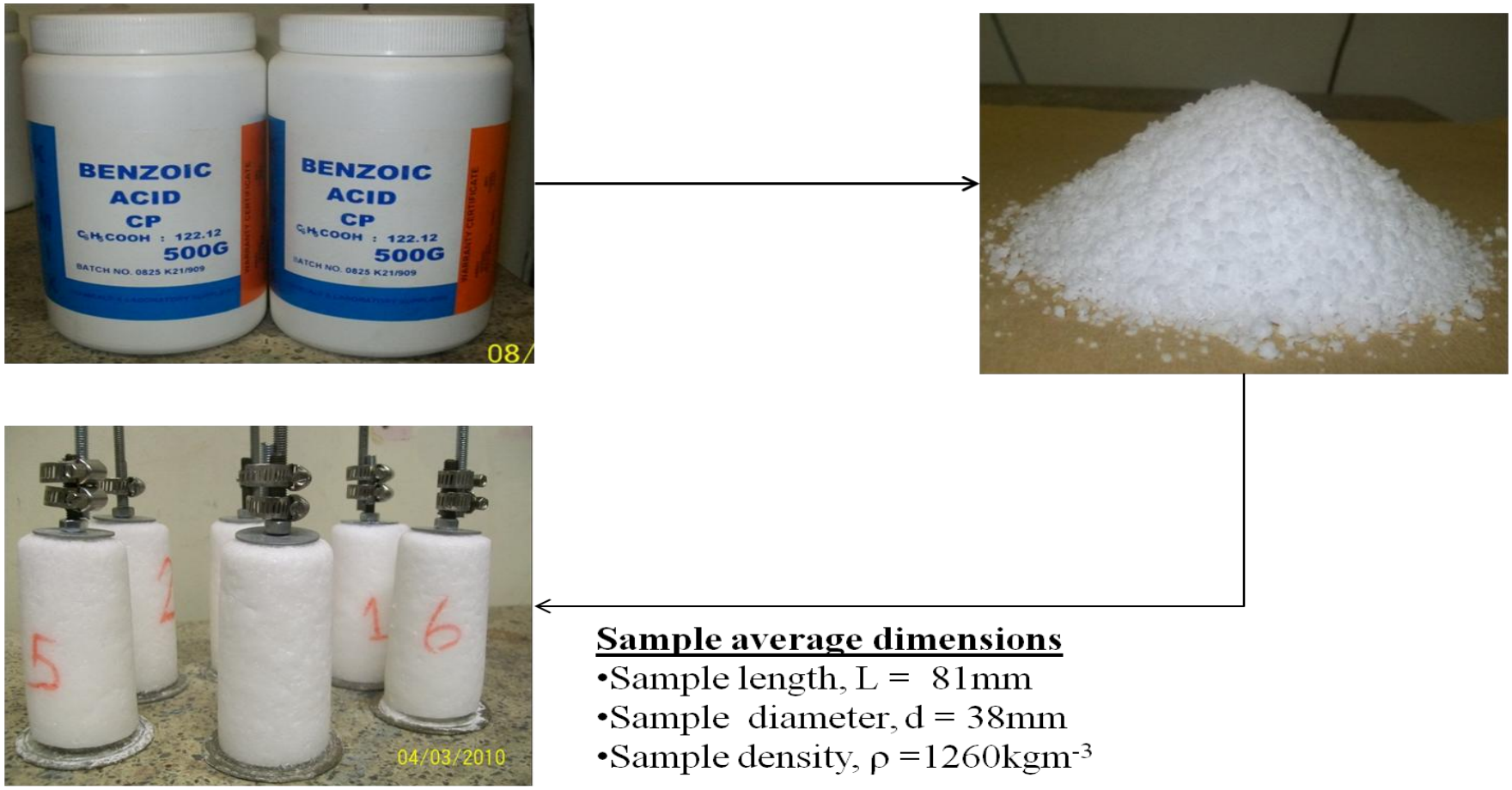

Figure A8: Laboratory produced benzoic acid sintered compacts